Universidade de São Paulo
Instituto de Física

Anisotropia azimutal de elétrons de quarks pesados em colisões p–Pb no ALICE

Henrique José Correia Zanoli

Orientador: Prof. Dr. Alexandre A. P. Suaide

Tese de doutorado apresentada ao Instituto de Física da Universidade de São Paulo, como requisito parcial para a obtenção do título de Doutor(a) em Ciências.

Banca Examinadora:
Prof. Dr. Alexandre A. P. Suaide - Orientador (IFUSP)
Prof. Dr. Edivaldo M. Santos (IFUSP)
Profa. Dra. Frederique Grassi (IFUSP)
Prof. Dr. Rafael Peretti Pezzi (UFRGS)
Profa. Dra. Sandra S. Padula (IFT/UNESP)

São Paulo
2018

FICHA CATALOGRÁFICA
Preparada pelo Serviço de Biblioteca e Informação do Instituto de Física da Universidade de São Paulo

Zanoli, Henrique José Correia

Anisotropia azimutal de elétrons de quarks pesados em colisões p- -Pb no ALICE. São Paulo, 2019.

Tese (Doutorado) – Universidade de São Paulo, Instituto de Física. Depto. de Física Nuclear.

Orientador: Prof. Dr. Alexandre Alarcon do Passo Suaide
Área de Concentração: Física

Unitermos: 1. Quark; 2. Colisões de íons pesados relativístico; 3. Elétrons; 4. Física nuclear.

USP/IF/SBI-010/2019

University of São Paulo
Physics Institute

Azimuthal anisotropy of electrons from heavy quarks in p–Pb collisions with ALICE

Henrique José Correia Zanoli

Supervisor: Prof. Dr. Alexandre A. P. Suaide

Thesis submitted to the Physics Institute of the University of São Paulo in partial fulfillment of the requirements for the degree of Doctor of Science.

Examining Committee:
Prof. Dr. Alexandre A. P. Suaide - Supervisor (IFUSP)
Prof. Dr. Edivaldo M. Santos (IFUSP)
Profa. Dra. Frederique Grassi (IFUSP)
Prof. Dr. Rafael Peretti Pezzi (UFRGS)
Profa. Dra. Sandra S. Padula (IFT/UNESP)

São Paulo
2018

Acknowledgments

I would like to thank my supervisor, Alexandre Suaide, and my co-supervisor, Andre Mischke for all the attention and support they gave me. They have both played a very important role during the course of my Ph.D., guiding me with scientific discussions, but also in some not-so-fun parts such as bureaucracy. Thanks again for all the work!

My family also deserves a lot of credit. I would like to thank my parents, Valdecir and Antonia, for all the love, support and patience in all those years. My brother Vinícius for the friendship and the discussions about science and politics which are an important part of my worldview. My sister Cristiane for all the years of friendship and help, which stimulate kindness and hope. Also to my nephew Lucas for all the happy and fun times we have together. I also appreciate the support that all my close and distant family members have given me.

I cannot forget to thank Jeroen, for all the support and companionship. From all the answering questions about programming to the nights spent together, thanks for the patience and tranquility. Jeroen has always shown me his inspiring intelligence and consideration together with love. Thanks!

Thanks to all my friends, for providing some nice ideas and a lot of fun! Anne and Paula for the long and honest friendship. Diógenes for the discussions about life (and physics sometimes). Jacopo for all the fun, and also for the serious, times in the Netherlands. Gabriela, Julia and George, for showing me the funniest and cutest cat videos. Maira for the all the conversations about politics. Ana, for the long friendship even with long distances. I also thank Lucas, Jéssica, Ricardo and José. Each one of you has contributed to something special in my life, thanks.

I would like to thank everyone involved in my education: family, teachers from primary to the university, and my colleagues. I would never be here if it was not for each one of them. Thanks for all the faith you had on me early on and helped me to focus on my studies. I cannot mention all their names, given the limited space, but they are very important for me.

I would like to thank all my friends and colleagues from my research group in São Paulo, in special Cristiane, Renato, Camila, Marcel, Arthur, Elienos, Geovane,

Diógenes, Milton, Caio, Lucas, Marcelo, Hugo, Marco, and Hermann. Special thanks also to Alexis for the time we worked at the initial stages of this work.

Thanks to the research group in Utrecht, that has welcomed me so well. In special to Cristina, Jacopo, Barbara, Lennart, Luuk, Auro, Annelies, Mike, Rihan, and Davide. Many thanks for a great time we had.

The ALICE collaboration was also an important piece to make this project happen. Thanks to my colleagues in the heavy-flavor working group, particularly to Elena Bruna, Andrea Rossi, Andrea Dubla, Alessandro Grelli, Barbara Trzeciak, and Shingo Sakai. I would like to especially thank Fabio Colamaria and Deepa Thomas for all the work we did to publish the results of this work in a paper.

I would like to thank the São Paulo Research Foundation (FAPESP, process number 2014/11042-9 and 2016/05723-9) and Conselho Nacional de Desenvolvimento Científico e Tecnológico (CNPq, process number 141633/2014-0) for their financial support to this work. I thank CNPq and CAPES for the funding of the graduation program of the Physics Institute of the University of São Paulo. I also thank The Netherlands Organization for Scientific Research (NWO) for support provided to the Dutch universities. Thanks to the all the staff from the University of São Paulo and Utrecht University. I appreciate the investment of the public money in basic research, education and outreach programs. The money invested will pay off in the future as a benefit for the ones in need.

When most laypeople see such an equation, they usually panic and freeze, like a deer caught in the headlights of a speeding vehicle. The reaction is quite natural, and does not betray a lack of intelligence or curiosity. With rare exceptions, human brains are simply incapable of thinking through concepts like relativity and quantum mechanics. Physicists nevertheless manage to do so, because they set aside the traditional human way of thinking, and learn to think anew with the help of external data-processing systems. Crucial parts of their thought process take place not in the head, but inside computers or on classroom blackboards.

Yuval Noah Harari in Sapiens: A Brief History of Humankind

Resumo

Um novo estado, o Plasma Quark-Gluon (QGP), é formado quando a matéria comum formada por hadrons é submetida a condições extremas de temperatura e/ou densidade. Acredita-se que esse estado esteja presente nos primeiros momentos do universo e que seja relevante para entender propriedades da cromodinâmica quântica. O QGP é criado e caracterizado em aceleradores de partículas por meio de colisões de íons pesados. No entanto, uma estrutura alongada em psedorapidez (*double ridge*) na distribuição da correlação angular entre duas partículas foi encontrada em sistemas pequenos, como pp e p–Pb. Essa estrutura assemelha-se àquela observada nas colisões com íons pesados, onde sua interpretação está ligada ao comportamento coletivo que gera uma anisotropia azimutal nos produtos finais das colisões. Essa estrutura não era esperada em sistemas pequenos e sua interpretação física ainda está em debate, em particular no que diz respeito ao papel da hidrodinâmica e das condições iniciais. Uma medida para este efeito com partículas provenientes de quarks pesados ainda não haviam sido realizadas no momento em que este trabalho foi iniciado e esta medida poderia esclarecer questões sobre as diferentes interpretações. Os quarks pesados são uma sonda interessante caso o QGP seja formado devido ao seu tempo de formação inicial, reagindo a toda a evolução do meio.

Neste trabalho, os quarks pesados são estudados medindo-se os elétrons provenientes dos decaimentos semi-leptônicos de hádrons que contêm quarks *charm* ou *beauty* e outros quarks leves (*open heavy flavor*). Os hadrons não são reconstruídos e usa-se um método de extração de sinal para remover elétrons de outras fontes. As correlações angulares de elétrons de decaimento de hadrons de quarks pesados com partículas carregadas em colisões de p–Pb a $\sqrt{s_{\mathrm{NN}}}$ = 5,02 TeV medidos com o experimento ALICE em rapidez central ($|\eta| < 0,8$) são apresentadas. As distribuições mostram sinais de anisotropias azimutais que são quantificadas pelo coeficiente v_2. O v_2 para elétrons provenientes de quarks pesados é positivo com mais de 5σ de significância, fornecendo uma forte indicação de anisotropias azimutais similares ao *double ridge* para partículas contendo quarks pesados em colisões de alta multiplicidade de p–Pb. Esta é a primeira medida do v_2 para elétrons vindos de quarks pesados em colisões p–Pb.

Palavras-chave: anisotropia azimutal, quarks pesados, plasma de quarks e gluons, sistemas pequenos, LHC

Abstract

A new state of mater, the Quark-Gluon Plasma (QGP), is formed when the ordinary hadronic matter is put under extreme temperature and/or density conditions. This state is believed to be present in the first moments of the universe and it is relevant to understand properties of the quantum chromodynamics. The QGP is created and characterized in particle accelerators by colliding heavy ions. However, a double-ridge long-range structure in the two-particle azimuthal correlation distribution was found in small systems, such as pp and p–Pb. This structure resembles the one observed in heavy-ion collisions, where its interpretation is linked to collective behavior that generates an azimuthal anisotropy in the final products of the collisions. This structure was not expected in small systems and its physical interpretation is still in debate, in particular regarding the role of hydrodynamics and initial conditions. A measurement for this effect with particles coming from heavy quarks was not done by the time this work started and this measurement could shed light into the different interpretations. Heavy quarks are an interesting probe in case the QGP is formed due to their early formation time, experiencing the whole evolution of the medium.

In this work, heavy quarks are examined by measuring electrons originating from the semi-leptonic decays of hadrons that contain a heavy quark (charm or beauty) and other light quarks (open heavy flavor). The hadrons are not reconstructed and a signal extraction method is used to remove electrons from other sources. The azimuthal angular correlations of heavy-flavour hadron decay electrons with charged particles in p–Pb collisions at $\sqrt{s_{\mathrm{NN}}}$ = 5.02 TeV measured with ALICE detector at mid-rapidity ($|\eta| < 0.8$) are studied. The distributions show signs of azimuthal anisotropies which are quantified by the v_2 coefficient. The v_2 for heavy-flavor electrons is found to be positive with more than 5σ significance, providing very strong indication of long-range azimuthal anisotropies for heavy-flavour particles in high multiplicity p–Pb collisions. This is the first measurement of the v_2 for electrons coming from heavy-flavor hadron decays in p–Pb collisions.

Keywords: azimuthal anisotropy, heavy quarks, quark-gluon plasma, small systems, LHC

Contents

1 — Introduction

The accumulated knowledge of how particles interact is often called the Standard Model of Particle Physics. The standard model contains the electromagnetic force, the weak force, and the strong force. Although the Standard Model describes many of the measurements done in the particle accelerators, there are many questions in the particle and nuclear physics that need better understanding. Some of these questions are: the origin of the mass, how to include gravity in the standard model, the origin of the measured dark matter and dark energy found in astrophysical observations, the mystery of the matter-antimatter difference in the universe, the confinement of quarks and gluons inside the atomic nuclei, and many others. One way, and sometimes the only known way, to answer these questions is to collide particles and study the products of this collision. This has made the particle and nuclear physics move to the era of large collaborations. Now different nations collaborate to build experiments that test those questions and explore the basic properties of our universe.

The motivation of this work is to study one of these problems: the confinement of quarks and gluons inside the atomic nuclei and to understand the basic properties of strong interaction. This problem is a key point to understand the basic properties of the quantum chromodynamics (QCD), a part of the Standard Model. QCD is the physical theory that describes the strong interaction. It explains how quarks interact to form hadrons. Its interactions are mediated by gluons, which interact with each other unlike photons of quantum electrodynamics. Quarks are “glued” together to form the ordinary matter we know, such as protons and neutrons. One of the central questions in QCD is that quarks (and gluons) seem to be confined inside the hadrons. This is widely accepted from the experimental point of view and from calculations of lattice QCD but its formal proof in a rigorous mathematical way is still unsolved. However, the confinement may break in certain conditions such as extreme temperature and/or densities. The quarks and gluons would not be confined in the hadronic scales, forming a hot and dense state that resembles the first moments of the universe. This state of matter is called Quark-Gluon Plasma (QGP) and its formation is expected in very dense systems, such as relativistic heavy-ion collisions in particle accelerators.

The study of the QGP can help to understand important properties of the QCD, such as confinement, jets, hadronization, and properties of the atomic nuclei. A few important properties of the QGP include interaction strength of particles going thought the medium and wheter the QGP is weak or strongly coupled. The properties are quantified by measurements of the jet supression, particle production ratios, Fourier coefficients of the azimuthal distribution of the final-state particles, and many other observables. The QGP is also likely related to the enhancement of the strange particle in heavy-ion collisions. Recent results in small collision systems, mainly pp and p–Pb collisions, have indicated that particles are not produced isotropically as expected. This anisotropy, in heavy-ion collisions with non-zero impact parameter, is attributed to the hydrodynamic evolution of the medium created and its collectivity. It is not clear at the moment how to interpret the anisotropy in those other collision systems, mainly regarding the role of hydrodynamics and initial conditions. This work measures the anisotropy of electrons coming from hadrons that contain heavy quarks in p–Pb collisions to further constrain models. In case the QGP is formed, the heavy quarks are great probes due to its early formation time. It was not clear whether this phenomenon was even present for heavy quarks when the work started, but the results point to a significant anisotropy with more than 5σ significance. This measurement may help to understand the basic properties of this anisotropies and, consequently, will help to understand the properties of the QCD.

The text is structured as follows. First, a brief description of the Quark-Gluon Plasma and some recent results are presented in Chapter 2. Chapter 3 follows the discussion extending it to the unexpected results found in small collision systems. Then the ALICE experiment and the Large Hadron Experiment (LHC), where the data was obtained, are introduced on Chapter 4. After those introductory chapters, the measurement is reported. Chapter 5 explains the common procedure to avoid repetition. The results for the LHC Run 1 are reported on Chapter 6, where it was not possible to measure the azimuthal anisotropy due to the insufficient number of events. The measurement was repeated for a new data set obtained in the LHC Run 2 and the azimuthal anisotropy of open heavy-flavor electrons was measured, as described in Chapter 7. The possibilities for this measurement during the next LHC run are described Chapter 8. The thesis is concluded by Chapter 9 with a discussion of the results, comparison to the results obtained by other collaborations, and the summary of the measurement performed.

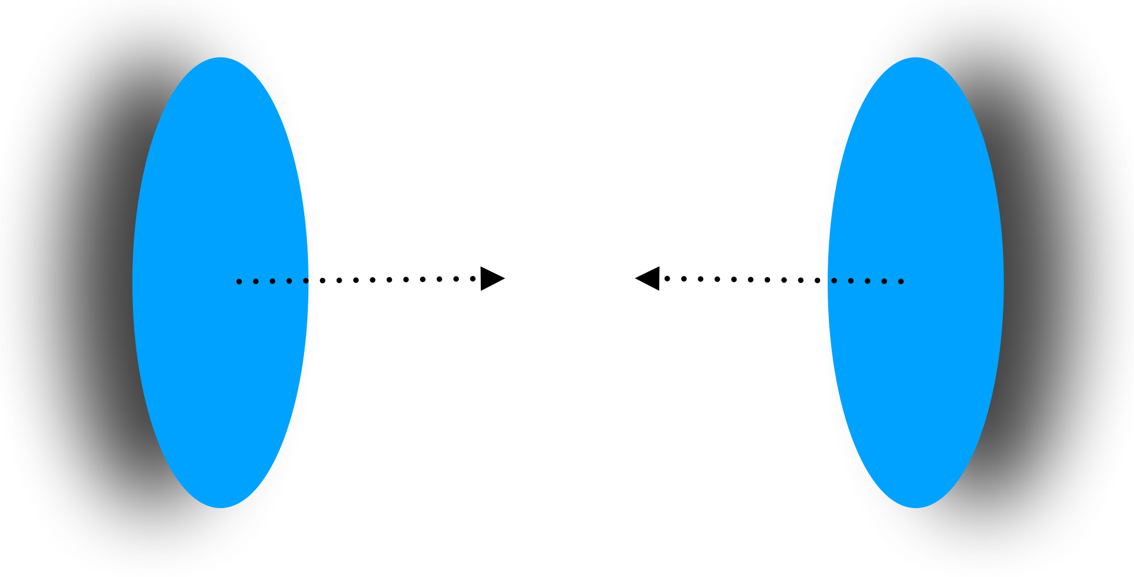

2 — Heavy-ion collisions and the Quark-Gluon Plasma

A new state of matter, the Quark-Gluon plasma (QGP), is formed when the ordinary nuclear matter is put under extreme conditions such as extremely high temperatures and/or densities. Its proposal as a state of matter candidate dates from the 1970s in the context of, for example, how matter would behave in neutron starts [1] or why the shape of the transverse momentum spectrum observed follows an exponential behavior [2]. It was inspired by Quantum Chromodynamics (QCD) properties, such as confinement and asymptotic freedom, that will be discussed on Sec. 2.1. It is believed that the early universe was in this state in the first few moments after its creation. The partons are not confined in the hadrons anymore, so the hadrons lose their identity and they are now part of a soup of quarks and gluons. The QGP is created under controlled experiments in particle accelerators by colliding heavy ions such as Pb and Au. The creation, expansion, and hadronization of the hot and dense medium take place in very short timescales and they will be discussed in Sec. 2.2. The collision product is studied using a vast number of observables, such as the nuclear modification factor, the elliptic flow and two or multi-particle correlations. Definitions and recent results of those observables will be presented on Sec. 2.3. It is important to highlight that a lot of those measurements depend on references in proton–proton or proton–nucleus collisions where usually no formation of the QGP is expected. However, measurements from the last decade have shown puzzling results as it will be discussed in Chapter 3. Nevertheless, this chapter will be focused in a brief discussion of the picture of the QGP in heavy-ion collisions.

2.1 Quantum Chromodynamics

In order to discuss the QGP, we need to understand the properties of the underlying fundamental interaction responsible for it: the strong force, part of the Standard Model for particle physics. The physical theory created to explain the strong interaction between quarks and gluons is the Quantum Chromodynamics (QCD) developed in the 1960s. The other Standard Model interactions are described in a unified electroweak theory that contains the weak force, explaining radioactive decay, and electromagnetic force, responsible for the interactions of charged particles and photons. Although the electro-weak theory is not directly related to the QGP, it has its importance in this field of study as reference probes.

In the first decades of the 20th century many *elementary* particles were discovered [3], one after the other, and the sense of their *elementariness* was affected. There were so many particles that the expression *particle zoo* was colloquially used to refer to these many particles. The quark model emerged to explain that these *elementary* particles were made of other particles: the quarks. The model was proposed independently in 1961 by Murray Gell-Mann [4] and George Zweig [5]. A few years later, in 1964, Oscar W. Greenberg [6] introduced a new charge that could have three different values, leading to what we today consider the color degree of freedom. In the following year, Moo Young Han e Yoichiro Nambu introduced the color gauge symmetry[7]. These are the basic ingredients to make the QCD.

QCD is a Yang-Mills theory with a local gauge symmetry SU(3). It describes the interaction of the six quarks and the gluons, shown in Figure 2.1, in the standard model. The QCD Lagrangian is:

$$\mathcal{L} = -\frac{1}{4} G^{a}_{\mu\nu} G^{a,\mu\nu} + \bar{\psi}(i\gamma_{\mu} D^{\mu} - m)\psi, \tag{2.1}$$

where:

- ψ is the fermionic field;
- $G^{a}_{\mu\nu}$ is the gauge invariant gluon field strength tensor given by $G^{a}_{\mu\nu} = \partial_{\mu} A^{a}_{\nu} - \partial_{\nu} A^{a}_{\mu} + g f^{abc} A^{b}_{\mu} A^{c}_{\nu}$, where f^{abc} are the structure constants of SU(3);
- A^{a}_{μ} is the gluon field;
- a is the index of the generators of the SU(3) group;
- D^{μ} is the covariant derivative $D^{\mu} = \partial_{\mu} - i g t^{a} A^{a}_{\mu}$;
- m is the quark mass. In case the theory has more than one quark (as it is in QCD) you should sum the last term over all the different quarks.

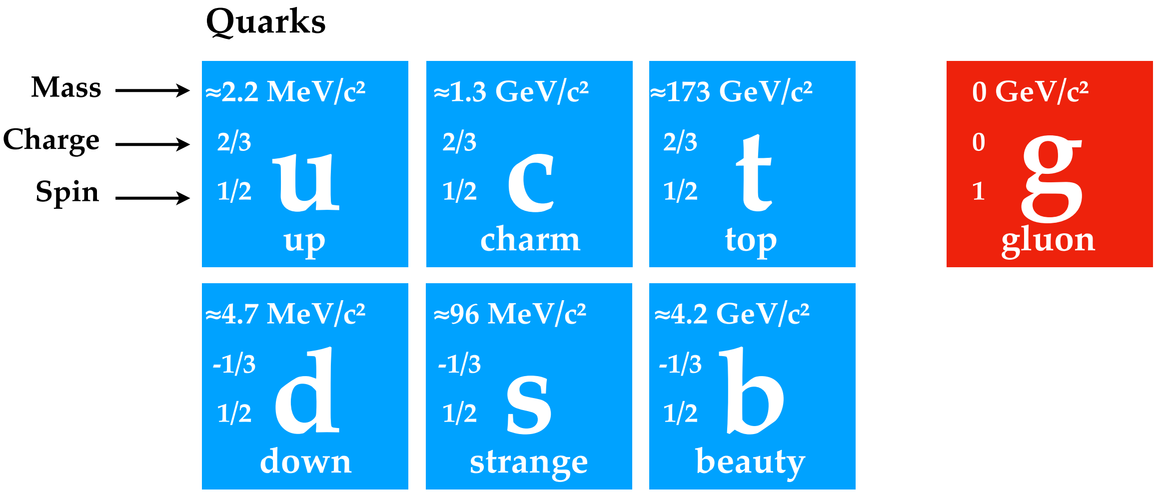

Figure 2.1: Particles from the Standard Model that interact through the strong force (QCD). Data of the mass and other properties are taken from Ref. [8].

The two most important properties from QCD are the asymptotic freedom, where the strong interaction becomes weaker for high energy (short distances), and (color) confinement, the fact that no color object has been seen isolated.

To understand the asymptotic freedom of the quarks, it is important to look at perturbative QCD (pQCD). The calculations from pQCD are obtained as an expansion in terms of the coupling constant ($\alpha_s = g^2/4\pi$). But as in most of the Quantum Field Theories (QFT), the calculations containing loops often have divergences and they need to be corrected. This is done through renormalization and regularization methods [9]. After the renormalization, α_s is dependent of the scale of energy we are probing. The first-order solution of the renormalization group equation for the QCD [9] is

$$\alpha_s(Q) = \frac{\alpha_s}{1 + (b_0\alpha_s/2\pi)\log(Q/M)}, \tag{2.2}$$

where Q is the energy scale, $b_0 = 11 - 2/3n_f$ and n_f is the number of fermions. It is common to define a scale (Λ_{QCD}) that satisfies Eq. 2.3.

$$1 = g^2\frac{b_0}{8\pi^2}\log(M/\Lambda_{QCD}) \tag{2.3}$$

Using Eq. 2.2 combined with Eq. 2.3, we can obtain Eq. 2.4. This equation clearly shows the behavior of the coupling constant for different values of Q. Thus, for larger values of Q ($Q/\Lambda_{QCD} \gg 1$) the interaction becomes weaker. In the limit $Q/\Lambda_{QCD} \to \infty$ the coupling constant vanishes ($\alpha_s \to 0$) making quarks and gluons almost free particles. This limit corresponds to very high energy (or very small distances). The asymptotic freedom of QCD was discovered by David Gross and Frank Wilczek [10] and by David Politzer [11], independently. This discovery gave them the 2004 Nobel Prize in Physics [12]. This prediction is confirmed by many experiments, as seen in Fig. 2.2. The other limit, when $Q/\Lambda_{QCD} \gg 1$, the coupling constant is greater than 1 and the perturbative regime is broken. The calculations are no longer valid since they assume that $\alpha_s(Q)$ is small.

$$\alpha_s(Q) = \frac{2\pi}{b_0 \log(Q/\Lambda_{QCD})}. \tag{2.4}$$

On the other hand, it is more complicated to understand the color confinement. We can qualitatively examine the problem by looking at two color-charged quarks being separated, as illustrated in Fig. 2.3. The QCD potential is approximately linear for large distances and thus the interaction can be understood in terms of tubes that are connecting the two quarks. When the distance increases, the interaction also grows, making it more energy costly to separate the two particles. At a given point it is more

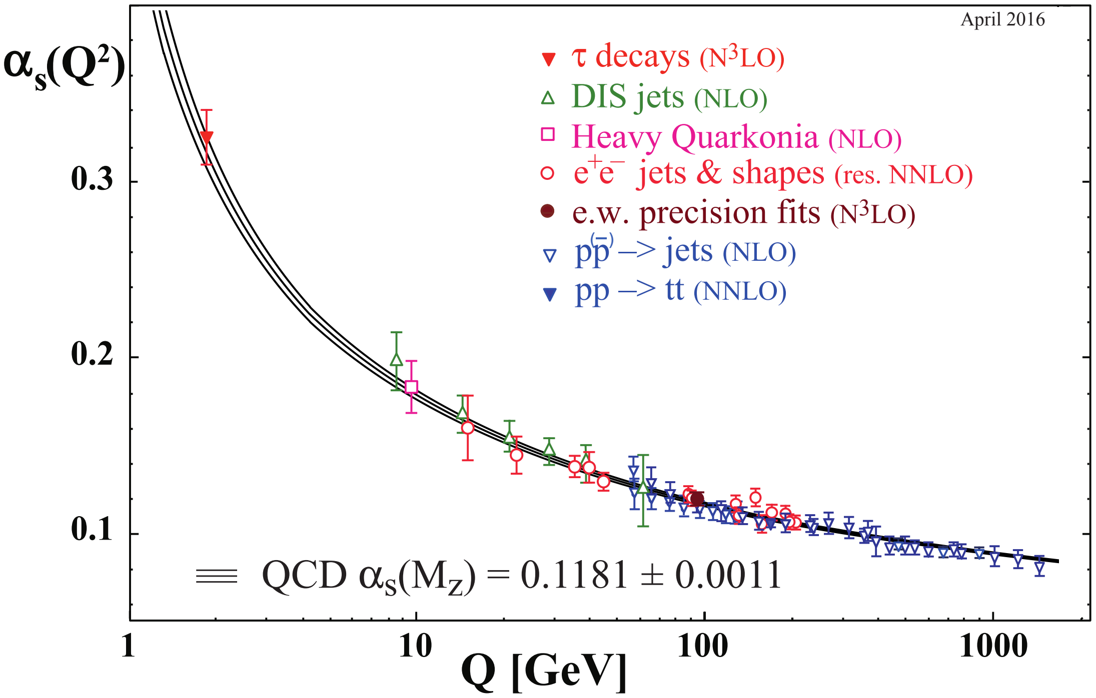

Figure 2.2: Evolution of the running coupling constant (α_s) of QCD as a function of the energy scale (Q). The degree of perturbation theory used is indicated in brackets. Figure taken from Ref. [13].

efficient to produce a new particle and antiparticle pair ($q\bar{q}$) rather than extending the tube further. The confinement is not yet fully understood from the mathematical perspective. It is one of the Millennium Problems from the Clay Mathematics Institute [14] and to prove it would be of great importance in this field.

Another approach towards examining confinement is to do calculations using lattice gauge theory, i.e. lattice QCD (lQCD), that have been developed since the 1970s [15] to address solutions in non-perturbative regimes. This formalism defines the theory in a discrete space-time domain and it provides ultra-violet cut-off by restricting highest momentum to π/a (a is the lattice spacing). The studies using lQCD also allow path integrals to be evaluated stochastically in the Euclidean formulation by using importance sampling [16]. Results from lQCD [15] show that confinement is strictly a low-temperature phenomenon and lead to evidence of a QCD transition from confined to deconfined quarks, in a state denominated the Quark-Gluon Plasma (QGP).

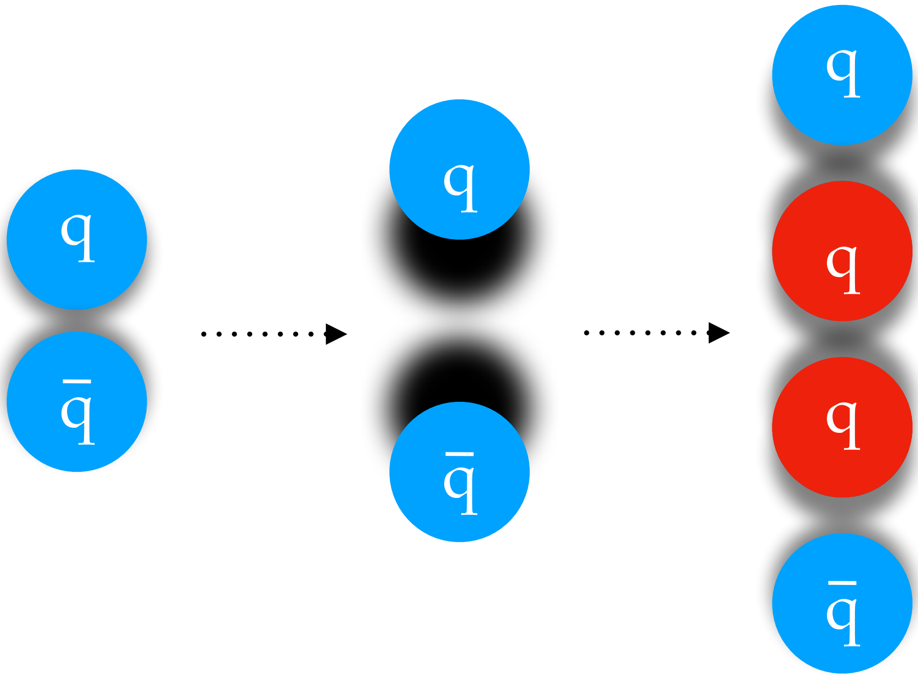

Figure 2.3: Illustration of the pair-creation process produced by the separation of two quarks (represented as two circles). The strong interaction (gluons) are represented by the shadows. The particles in blue are separated more and more from the left to the right until a pair (particles in red) is produced.

2.2 Creating the QGP by colliding heavy ions

This new phase of the nuclear matter, the Quark Gluon Plasma, is expected to be formed in conditions of high temperature or pressure, such as the first moments of the Universe due to the extremely high temperature and also in the core of neutron stars because of their extreme density. Understanding the properties of the QGP will help us to enlighten the QCD phase diagram. A figure of the phases of QCD as a function of the temperature and baryon chemical potential is illustrated in Fig. 2.4. In the bottom of the diagram, the vacuum is on the left at (0,0), surrounded by the hadron gas state, and going to the center we can find the ordinary matter. Moving more to the right of the diagram there are also the neutron stars and another state, the Color superconductor. In the top of the diagram, the region of the Quark-Gluon Plasma (QGP) is shown. Over the years, the theoretical understanding of the QGP has evolved, as discussed in the introduction of Ref. [18]. The definition of Ref. [18] is not too broad and covers the current understanding of the community:

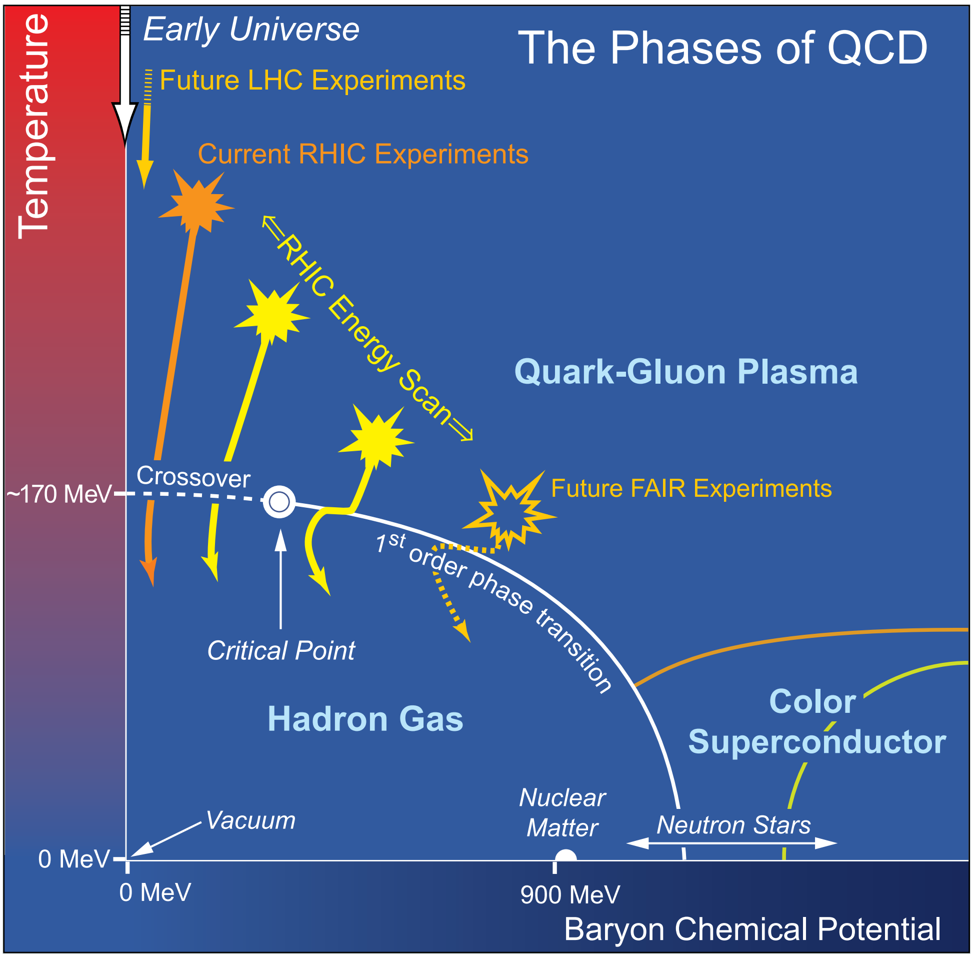

Figure 2.4: Illustration of the phase diagram of QCD. The different phases and phase transitions are listed. The experiments used to explore the regions are represented by arrows. Figure from Ref. [17].

> ”For our purposes here, we take the QGP to be a (locally) thermally equilibrated state of matter in which quarks and gluons are deconfined from hadrons, so that color degrees of freedom become manifest over nuclear, rather than merely nucleonic, volumes.”

This definition is based on the need of thermalization and deconfinement, but it lets out a few outdated concepts. It was believed that the QGP would have almost non-interacting quarks and gluons, but lQCD calculations point that the deconfinement transition happens actually at lower temperatures. Also, there is no requirement of an evidence of a first- or second-order transition or the restoration of the chiral symmetry. They are not excluded from the properties but are not explicitly requested to the discovery of the QGP [18].

In order to explore the properties of the phase diagram and understand the properties of the QGP, it is necessary to recreate extreme conditions of density and temperature in a controlled environment. This is usually done by colliding heavy ions at high energies, such as lead and gold, in particle accelerators. This generates a very high temperature due to the energy of the collisions and a higher density than in pp or ee collisions since heavy ions have greater size and number of constituents. An illustration of a collision of two heavy ions with impact parameter b is shown in Fig. 2.5. In the left side, the particles are traveling in opposite directions and are going to collide in the interaction point. On the right side, the collision already took place and a high number of particles is produced. The particles that have interacted will evolve in

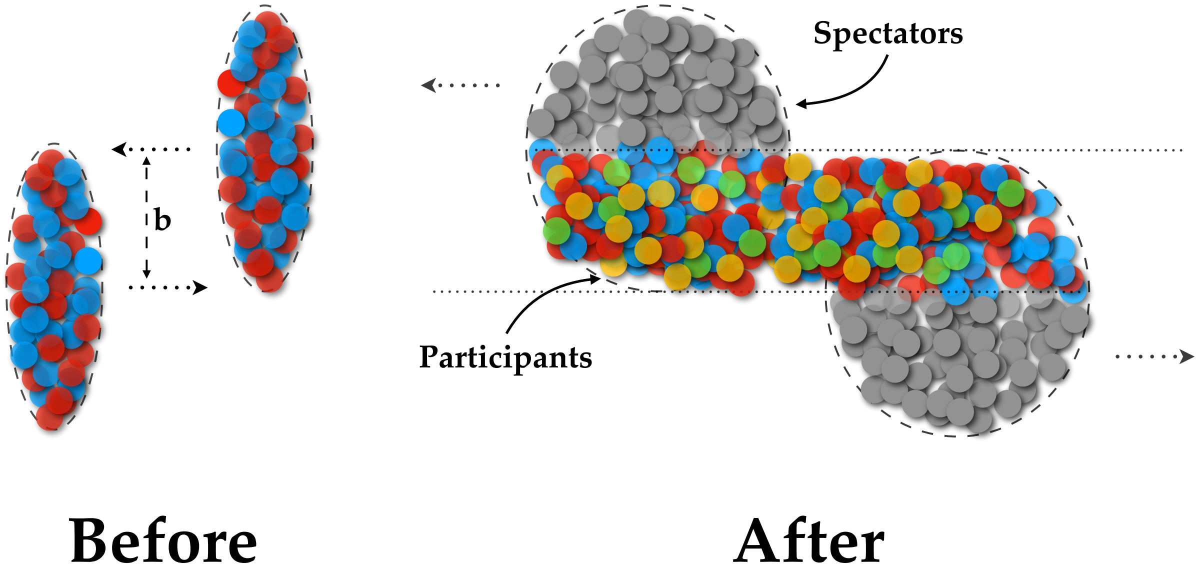

Figure 2.5: Schematic of colliding two heavy ions. On the left side, the two ions are traveling in opposite directions with an impact parameter b. On the right side, they have already collided and it is shown the particles that participated in the collisions in color and the ones that have not collided in gray.

different phases that will be described in the following paragraphs and produce other particles that can be measured on the experiments. Then, properties of these collisions are compared to models and different systems in order to understand the complex system formed in heavy-ion collisions.

The number of particles that have collided defines an important experimental concept: the number of participants. Another important definition is the spectators: partons that have not collided and they move forward unaffected. A way to understand this better is shown on the right side of Fig. 2.5 where both participants and spectators are represented. The spectators are usually the proxy to determine the number of participants. The participants cannot be directly measured because they have interacted and generated different particles. So, while in head-on collisions ($b = 0$), also called central collisions, all (or almost all) the protons and neutrons of the nucleus participate and there are no spectators, in non-central collisions the ($b \neq 0$) only a few of the partons have collided and the participants can be deduced by measuring the number of spectators. The diagram of Fig. 2.4 also points to the regions explored by the experiments such as the Large Hadron Collider (LHC), very close to the temperature axis; the Relativistic Heavy Ion Collider that covers a large horizontal area by changing the energy and particles they are colliding and is particularly interesting to study the phase transition itself; and the FAIR experiment, currently under construction.

After the collisions of the participants, the system undergoes a series of stages as shown in Fig. 2.6. In the horizontal direction, the beam axis is shown (representing positions) and, in the vertical axis, the time is represented with the collision as the reference. The figure compares the system in case the QGP is formed (right, that happens in heavy ion collisions) with the case it is not formed. For the case that the QGP is formed, we can divide it into the following phases [19, 20]:

- Pre-Equilibrium: happens just after the collision, when the time is smaller than the formation time of the QGP ($t < \tau_0$). The time is still too short for the system to thermalize. Partons with large momentum ($p_{\mathrm{T}} \gg 2$ GeV$)/c$) and mass (b, c and t quarks) are produced in this phase because they require a considerable amount of energy to be produced.

- Quark-Gluon Plasma (QGP): as discussed before, it is a phase where quarks and gluons are no longer confined inside the hadrons. It is a very hot and dense medium, forming a thermalized system. It has collective behavior. The particles traveling through it loose energy in radiative emission (gluons) or due to collisions. The system will expand rapidly making the temperature drop. It stays in this stage until the temperature reaches a critical temperature T_c where the chemical freeze-out will start.

- Mixed phase: depending on the type of the phase transition, the QGP can coexist with another state of the nuclear matter.

- Hadronization: At this stage, the hadronization will take place and the partons will be confined in hadrons. The hadronization can happen through two different mechanisms: fragmentation, a dominant process for large momentum particles, or coalescence, more important for intermediate momentum particles. Fragmentation is when high transverse momentum partons fragment (i.e, break its energy into small *pieces*) and produce other lower transverse momentum particles. Coalescence usually involves the combination of partons that have low transverse momentum, leading to the formation of a hadron with larger transverse momentum. The produced particles will interact between themselves while they are expanding and the system will cool down. When the temperature of the system is below the chemical freeze-out temperature (T_{ch}), the hadrons of the system will not interact between themselves anymore, other than the kinetic interaction (collisions).

- Chemical freeze-out: the particles species are fixed.

- Hadron gas: in this phase, the system is still expanding and the particles still change momentum in collisions. But now the quarks and gluons are confined

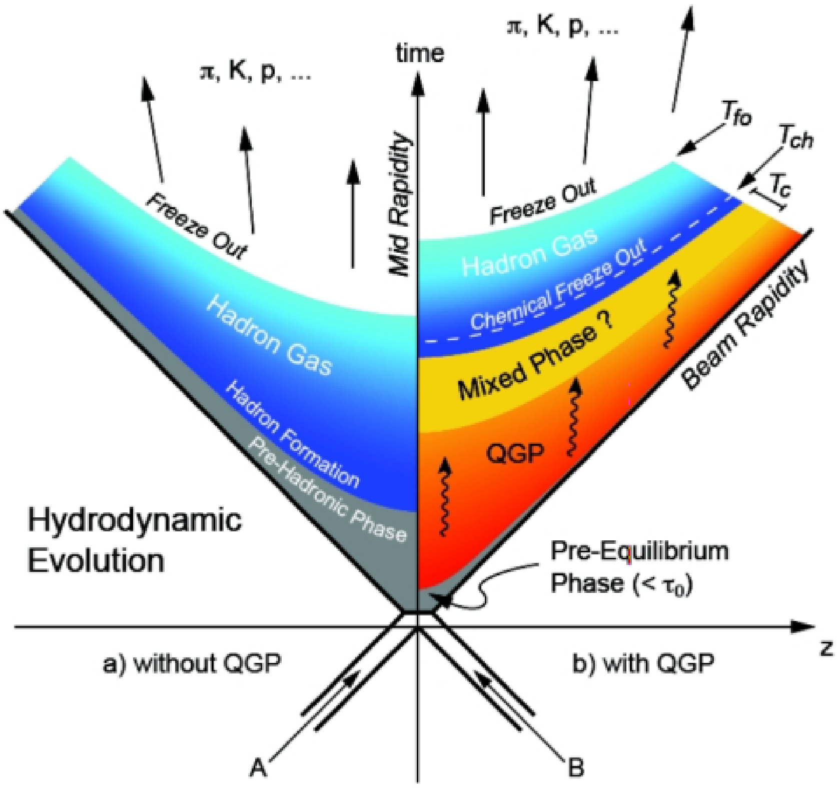

Figure 2.6: Illustration stages of the collision of two particles in case no QGP is formed (a) and with the formation of the QGP(b). Figure taken from Ref. [21].

to the hadrons since the hadronization already happened. The energy is mostly exchanged by collisions.

- (Kinetic) Freeze-out: when the density becomes low due to the expansion, the particles do not collide. The medium distance between the particles will be greater than the radius of the interaction of the strong force. At this point, the system reaches a temperature that the kinetic freeze-out occurs (T_{fo}). The momentum does not change and the kinetic equilibrium is reached. The particles will now travel in the detector, they might decay or not depending on their species, and will be measured by the experimental apparatus.

Although the process was described as a series of well-defined states, this is a simplification of a very complex process. It depends on fluctuations in the initial conditions, the dynamics of the evolution, details of each state and random processes. After all these processes, the particles produced by these collisions and its evolution are measured by the detectors. The extraction of properties of the QGP is performed in measurements of the final particles that hit the detector. But the process of linking these measurements and the properties is complicated. First, even with the high precision of modern particle accelerator, some hypothesis need to be made about the initial state of the particles, such as the energy density of the partons in the nuclei, usually assumed to be following the Glauber model [22], and if there is any correlation in the initial state of particles from both beams. Also, the models used to compute the evolution of the system need to rely on prescriptions to perform hadronization and decays. As it will be discussed in the next chapter, part of these sources is expected to cancel by using ratios or comparisons of the same observable across different systems. The discussion will move in the sense of how to experimentally quantify properties of this state and techniques used in the analysis of these collisions.

2.3 Observables and evidences for the QGP formation

Before moving to the observables definitions, we can take some time to have a more general idea about what we can measure in the produced particles. First, the type of particles generated. The QGP is a QCD medium, so particles that have a color charge are mostly affected by it. This already sets one of the reference observables we can use: electromagnetic probes, which are not expected to interact with the QGP by the strong force, since they have no color charge. So photons, Z and W bosons, and leptons are great reference particles. But in experimental conditions they are very hard to measure: or they have a very large mass and consequently a very low production yield, for example, the Z and W bosons and τ; or there are a lot of other particles that decay in channels that involve the particles of interests. Even with the challenges, the measurements in this sector usually points that we see no interaction with the QGP.

The other part of the particles produced in the collisions, the quarks and gluons, interact with the QGP by the strong force since they have color charge. They are usually divided into two classes: **soft probes** and **hard probes**. Soft probes are particles with low mass (pions, kaons, etc) and low transverse momentum ($p_T \lesssim 2$ GeV$/c$). Since the energy necessary to produce them is low, they can be produced in almost all the phases that happen after the collision. They are very abundant and it is possible to measure their properties with great precision, often limited only by the systematic uncertainties of the procedure. On the other hand, hard probes are particles with large mass, for example, charm and beauty quarks; particles with large transverse momentum ($p_T \gtrsim$ 10 GeV$/c$); jets, the spray of particles produced by the fragmentation of high energy particles. They all share a common property: since they require a large amount of energy to be produced, their production can only happen in the initial moments of the collisions in a time of the order of the inverse of the quark mass. This allows them to experience the full evolution of the system, probing its evolution.

To quantify the main characteristics of the QGP it is important to explore the observables for the different particles produced in the collisions. In the next subsection, the production of particles in different systems and the correlation between the particles in the same event (the collective effects and jet suppression) will be briefly explained as one of the few observables used to study the QGP.

2.3.1 Nuclear Modification factor

One way to characterize the QGP is to study the modifications of the particle production in the presence of the medium. It is done comparing an observable O_{AA} in the heavy-ion collisions, where the QGP (*hot QCD medium*) is expected to be formed , with respect to the same observable O_{pp} in the *QCD vacuum* (pp collisions) normalized by some normalization factor N (such as the number of binary collisions), as function of function of center of mass energy ($\sqrt{s_{NN}}$), transverse momentum (p_T) , rapidity (y), reaction centrality (impact parameter b), and particle type/mass (m) [23]:

$$R_{AA}(\sqrt{s_{NN}}, p_\mathrm{T}, y, b, m) = \frac{\text{“hot QCD medium”}}{\text{“QCD vacuum”} \times N} \propto \frac{O_{AA}(\sqrt{s_\mathrm{NN}}, p_\mathrm{T}, y, b, m)}{Opp(\sqrt{s}, p_\mathrm{T}, y, m) \times N} \tag{2.5}$$

Deviations from the unity, enhancement ($R_{AA} > 1$) or suppression ($R_{AA} < 1$), can be connected to properties of QGP if the other nuclear effects are well understood. These other effects will be discussed later in this section, since they are very important to separate the contributions that modify the R_{AA}. In case the QGP is formed, one source of suppression is that the particles have lost energy to the medium via inelastic processes (gluon radiation) or elastic scatterings (collisional processes). Modifications due to the interaction with the medium are called *final-state effects*. This observable is usually reported for the soft probes and for the hard sector that includes open and hidden heavy-flavor hadrons (D mesons, B mesons, J/ψ, etc), high p_T particles and jets. These measurements as functions of particle species allow us to study the mass dependence of the R_{AA}. Quarks should lose less energy than gluons due to their smaller color factor. Heavy-quarks (c and b) are expected to suffer less suppression, when compared to light quarks or gluon, due to the "dead-cone effect" that reduces the small-angle gluon radiation [24–27]. It is important to stress that at high momentum, when p_T is considerably higher than the particle mass, the mass dependence of the R_{AA} would not be relevant anymore.

The most common way of presenting the nuclear modification factor is as function of the transverse momentum:

$$R_{AA}(p_{\mathrm{T}}) = \frac{1}{< N_{coll} >} \frac{\frac{dN^{AA}}{dp_{\mathrm{T}}}(p_{\mathrm{T}})}{\frac{dN^{pp}}{dp_{\mathrm{T}}}(p_{\mathrm{T}})}, \tag{2.6}$$

where $< N_{coll} >$ is the number of binary collisions calculated using the Glauber Model [22], $dN^{AA}/dp_{\mathrm{T}}(p_{\mathrm{T}})$ and $dN^{pp}/dp_{\mathrm{T}}(p_{\mathrm{T}})$ are the yields as function of the p_{T} in heavy-ion collisions and pp collisions, respectively. Recent measurements report a strong suppression of light and heavy quarks in Pb-Pb collisions at the LHC. For example, one result that compares the R_{AA} for different particles is reported on Figure 2.7. We can observe that charged particles have $R_{AA} < 1$ for almost the whole range reported. It also has a structure with a local maximum around $p_{\mathrm{T}} = 2\,\mathrm{GeV}/c$ and a local minimum around $p_{\mathrm{T}} = 7\,\mathrm{GeV}/c$ and it reaches $R_{AA} \approx 1$ for $p_{\mathrm{T}} > 100\,\mathrm{GeV}/c$. This structure is usually assumed to be the combination of a few factors such as the energy loss discussed in the previous paragraph and properties linked to the cold nuclear matter properties, as it will be discussed later. Similar features are also present for the D mesons R_{AA}, that are fully compatible with the charged particles R_{AA} within uncertainties. The non-prompt J/ψ and B mesons have larger uncertainties that make it harder to draw conclusions, but they are also compatible with the charged particles one. This is not in contradiction with the previous statement that we would expect the R_{AA} to have a mass dependence, given the limited precision for low p_{T} region where the effect is more relevant. There are measurements from the LHC from a wide range of particles, including charged particles, pions, kaons, ϕ mesons, D mesons, Z and W bosons, J/ψ and much more, with similar conclusions as reported on Refs. [32–43]. Similar features were observed at RHIC [18, 44–50].

It is also relevant to perform a comparison with intermediate collision systems, such as proton–nucleus collisions, to account for possible modifications that do not

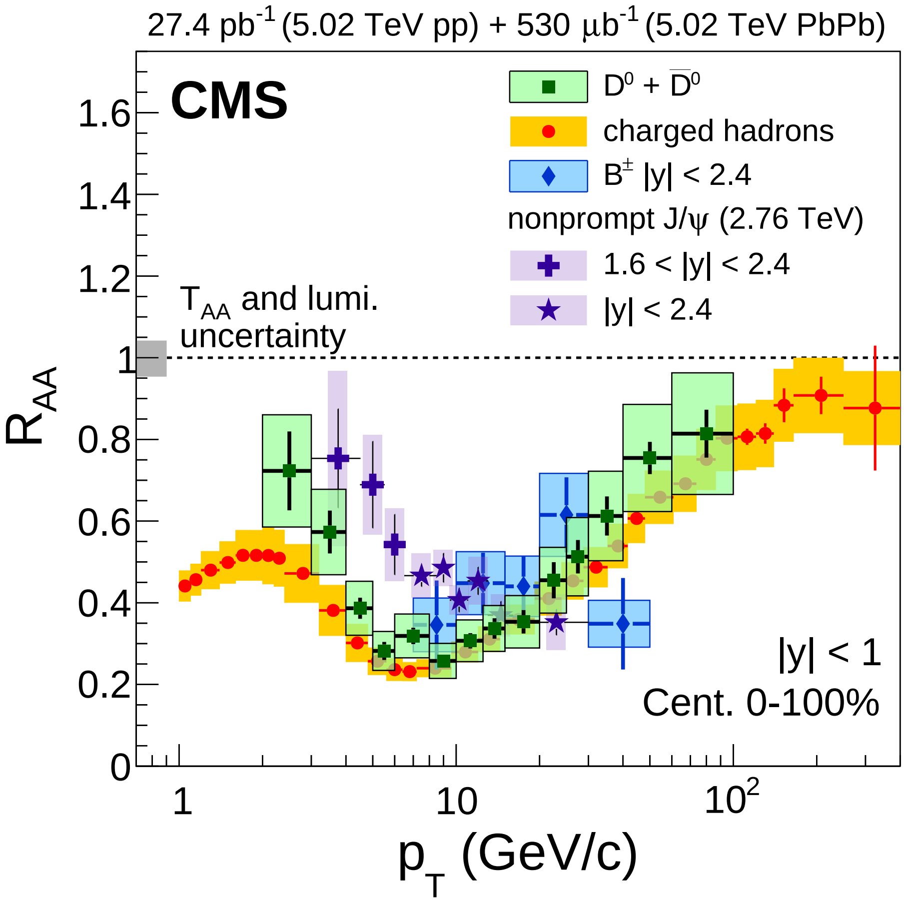

Figure 2.7: R_{AA} for Pb-Pb collisions at $\sqrt{s_{\mathrm{NN}}}$ = 5.02 TeV as a function of p_{T} in the centrality range 0–100% for D mesons (green, Ref. [28]), charged hadrons (orange, Ref. [29]) and B mesons (blue, Ref. [30]). In purple the R_{AA} of non-prompt J/ψ at $\sqrt{s_{\mathrm{NN}}}$ = 2.76 TeV Pb-Pb collisions in two different rapidities is reported (Ref. [31]). Figure taken from Ref. [28] .

come from the interaction with the medium. These *initial-state effects* (or Cold Nuclear Matter effects) are related to properties of the nuclei and other properties coming from the initial conditions. They should not be directly connected to the QGP or other final state effect. They include the parton density shadowing [51], a depletion in the parton distribution function in the low x (fraction of momentum carried by the parton) region, and momentum broadening or Cronin enhancement [52] where the high-momentum particle production is enhanced. Inspired on Eq. 2.5, similar quantities are defined: proton–nucleus collisions ("cold QCD matter") observables are divided by the same observable in pp collision, normalized usually by the number of binary collisions or the atomic number (if cross sections are used). The nuclear modification factor is now denoted as R_{pA}:

$$R_{pA}(\sqrt{s_{\mathrm{NN}}}, p_{\mathrm{T}}, y, b, m) = \frac{\text{“cold QCD matter”}}{\text{“QCD vacuum”} \times N} \propto \frac{O_{pA}(\sqrt{s_{\mathrm{NN}}}, p_{\mathrm{T}}, y, b, m)}{Opp(\sqrt{s}, p_{\mathrm{T}}, y, m)}. \tag{2.7}$$

and again the most common way to report it is as function of transverse momentum:

$$R_{pA}(p_{\mathrm{T}}) = \frac{1}{< N_{coll} >} \frac{\frac{dN^{pA}}{dp_{\mathrm{T}}}(p_{\mathrm{T}})}{\frac{dN^{pp}}{dp_{\mathrm{T}}}(p_{\mathrm{T}})}, \tag{2.8}$$

where $< N_{coll} >$ is number of binary collisions calculated using the Glauber Model [22], $dN^{pA}/dp_{\mathrm{T}}(p_{\mathrm{T}})$ and $dN^{pp}/dp_{\mathrm{T}}(p_{\mathrm{T}})$ are the yields as function of the p_{T} in proton–nuclei collisions and pp collisions, respectively. The D-meson and charged-particle R_{pA} are shown on Fig. 2.8. The first noticeable characteristic is the suppression of the charged-particle R_{pA} for $p_T < 2$ GeV/c. A similar feature is observed in the average non-strange D-meson R_{pA}, but the uncertainties do not allow us to draw strong conclusions.

For both D mesons and charged particles, the R_{pA} is compatible with one for $p_{\mathrm{T}} > 2$ GeV/c indicating that most of the suppression observed in the R_{AA} should come from the interaction with the QGP. Similar conclusions are also reached by comparing other particle productions in p–Pb and pp collisions. This lead to the conclusion that the suppression observed in heavy-ion collisions is a final-state effect coming mostly from the interaction with the QGP and not from Cold Nuclear Matter effects.

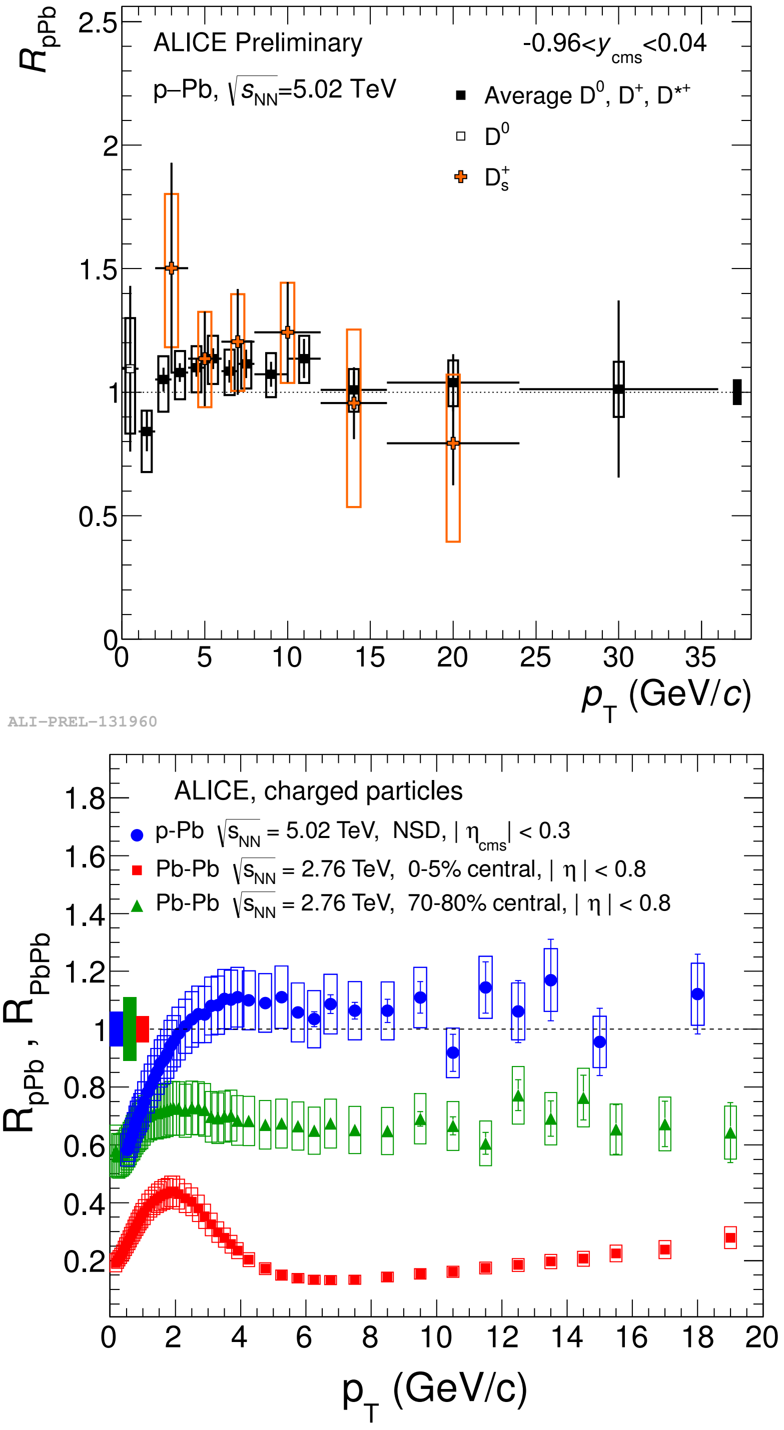

Figure 2.8: R_{pA} of D mesons (upper panel [53]) and charged particles (lower panel [54]) for p-Pb collisions at $\sqrt{s_{NN}}$ = 5.02 TeV as a function of p_T measured by the ALICE collaboration.

2.3.2 Two-particle correlations

Correlation functions are an important tool developed to study the QGP and rely in differences of properties of the particles in the same event. One of the most intuitive way to study how two particles in an event are correlated is to study the difference in the angles between them. It is said that one particle starts the correlation, usually called *trigger* and that the other particles they are compared against are known as *associated*. So the simplest correlation function is obtained by subtracting both azimuthal angle ($\Delta\varphi = \varphi_{assoc} - \varphi_{trigger}$) and pseudorapidity ($\Delta\eta = \eta_{assoc} - \eta_{trigger}$). The two-particle correlation distribution is computed as:

$$C(\Delta\varphi, \Delta\eta) = \frac{1}{N_{triggers}} \frac{d^2 N^{trigger-assoc}(\Delta\varphi, \Delta\eta)}{d\Delta\varphi d\Delta\eta}, \tag{2.9}$$

where $N_{triggers}$ is the number of trigger particles and $N^{trigger-assoc}$ is the number of pairs formed by triggers and associated particles.

One example of that correlation distributions is illustrated in Fig. 2.9. It has a few characteristics that are related to the underlying physical mechanism of the particles produced. It typically has a near-side peak at $(\Delta\varphi, \Delta\eta) \sim (0, 0)$ created by the jet that contains the trigger particle. There is also an away-side structure, due to the recoil jets, centered at $\Delta\varphi \sim \pi$ and extended over a very wide pseudorapidity range. The correlation distribution also exhibits pronounced structures on the near- and away-side extending over a large $\Delta\eta$ region, commonly called "ridges" [55]. Their origin is related to the collective motion of the system during the QGP phase and they will be discussed in more detail later, in Sec. 2.3.3. In non-central nuclei-nuclei collisions, the second Fourier coefficient, also called elliptic flow, is the dominant one. So, two important properties of the QGP can be accessed with this observable: the modifications of the jet structures in the presence of the QGP and the elliptic flow and higher Fourier coefficients, related to the collective motion of the system and to the initial geometry fluctuations.

Jet suppression

As seen in the previous section, the particle production is suppressed in nucleus–nucleus collisions. This should also be seen in jets since they are composed of particles. The two-particle correlation analysis adds the possibility to understand how jets are suppressed. Figure 2.10 shows a famous plot from the STAR collaboration that compares the two-particle correlations in pp, d–Au and Au-Au collisions [56]. In this analysis, the contribution of the elliptic flow is subtracted from the correlation and only the jet component is shown. In pp collisions, there is clear near-side peak. The broad distribution in η in the away side is also seen as a a peak, since it was projected

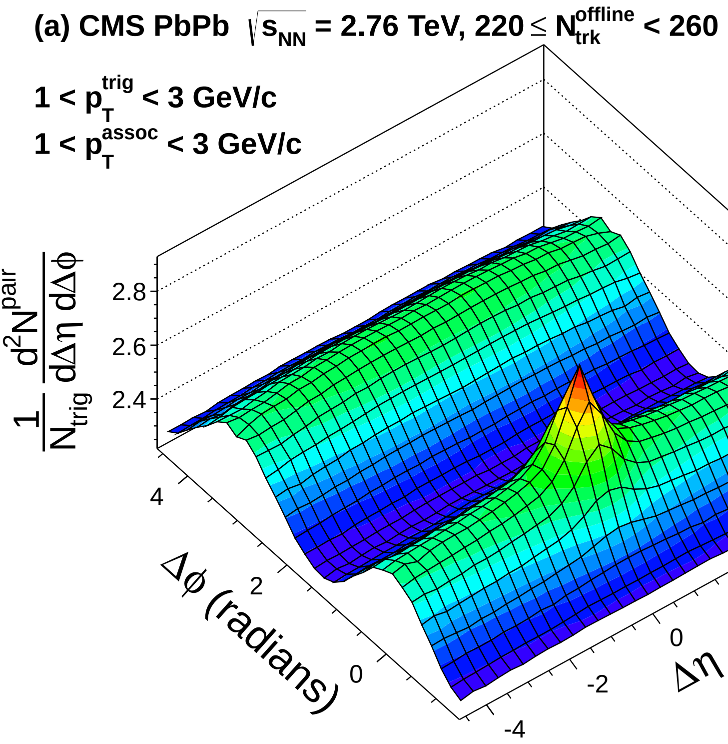

Figure 2.9: Two-particle correlation distribution for pairs of charged particles with $1 < p_T < 3$ GeV/c for events with $220 \leq$ Number of tracks < 260 for 2.76 TeV Pb–Pb collisions measured by CMS [57].

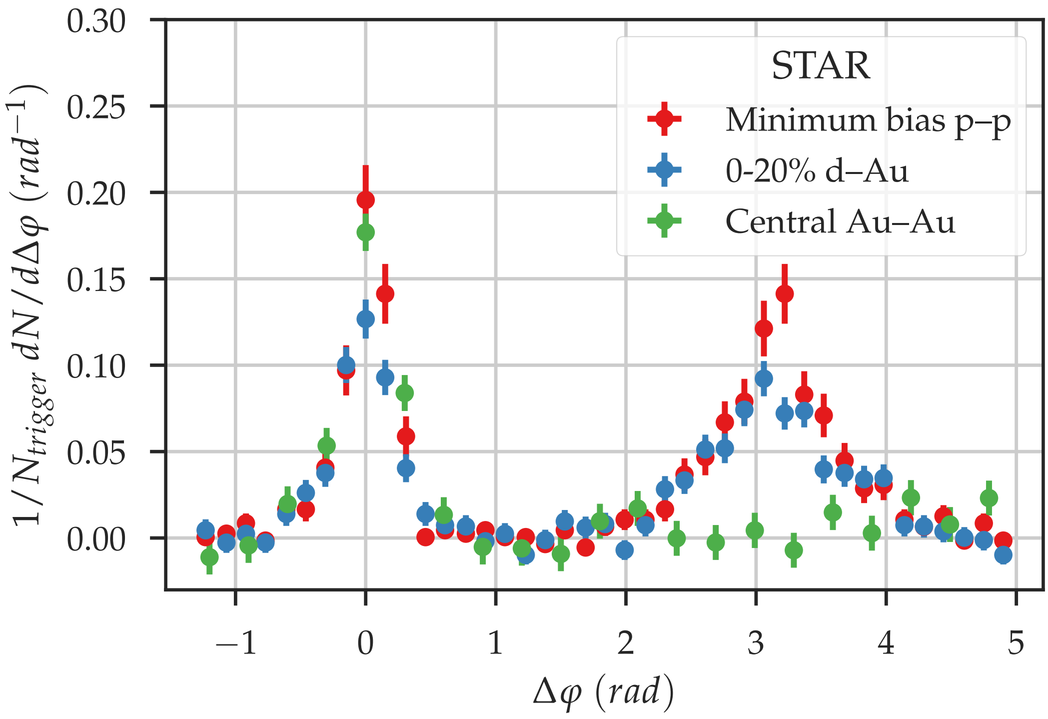

Figure 2.10: Comparison of two-particle azimuthal distributions for central Au–Au, d–Au and p–p and collisions obtained by the STAR collaboration. Data from Ref. [56].

onto $\Delta\varphi$. Moving towards a larger system, the d–A collision, a similar structure is also found. But when both structures are compared to the central Au–Au collisions, it is possible to see the clear suppression in the away side. This can be qualitatively interpreted as the formation of a di-jet pair in the border of the QGP. One of the jets will go quickly outside of the medium while the other one will have to travel through the QGP and it will lose energy to the medium. The jet in the border will appear in the near side, and the other one is suppressed in the away side. This is the jet suppression caused by the interaction with the QGP.

2.3.3 Elliptic flow and collective motion

The double-ridge structure of the correlation function comes mainly from the collective motion of particles in the QGP. To understand how it is generated, we may first have a look in a non-central nuclei-nuclei collision shown in Fig. 2.11. Since the impact parameter is non zero, the interaction region has an almond-like shape, shown in red. As said before, the particles that are in this volume are called participants. The plane defined by beam axis and the direction of the short axis of the participating nucleon distribution (in gray) is called participant plane and it plays a role in understanding the particle production in these collisions. As said in Sec. 2.2, the particles in the QGP phase present a collective behavior, where the re-scattering of the partons may result in a local thermal equilibrium. The anisotropy in space, due to the almond-like shape of the interaction area, is translated into anisotropic pressure gradients, which is responsible for a collective expansion. The expansion is also not uniform: the direction along the short axis has much more pressure than the one in the long axis. So the initial geometry of the collisions (initial-state particles), through the interaction with the QGP, creates an azimuthal anisotropy on the final-state particles. This is usually quantified by looking at the Fourier expansion azimuthal angle (φ) distribution of the particles

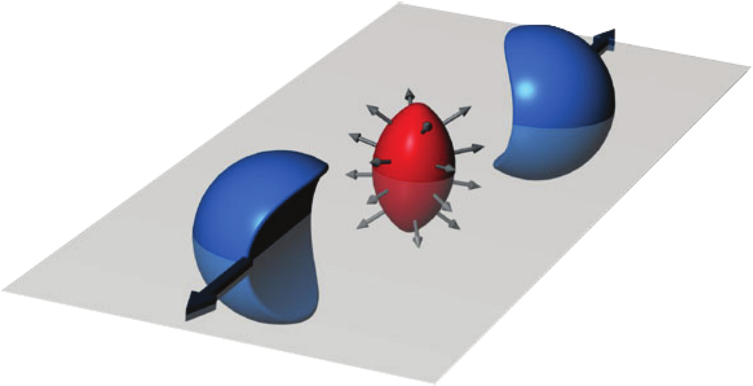

Figure 2.11: Shape of the interaction volume after a non-central collision of two nuclei. Figure taken from Ref. [58].

yield:

$$\frac{dN}{d\varphi} \propto 1 + \sum_{n=1}^{\infty} 2\, v_n \; \cos[n(\varphi + \psi_n)], \tag{2.10}$$

were v_n are the Fourier coefficients, and ψ_n is the event-by-event azimuthal angle of the participant plane. The shape of the interaction area in non-central nuclei-nuclei collisions makes the second-order coefficient (v_2, also called elliptic flow) dominant over others. The high-order coefficients are mostly related to the fluctuations of the initial conditions of the system, such as the distributions of the partons inside the nuclei and geometry. An illustration of the different contributions to the coeffients is shown in Fig. 2.12. The anisotropic flow depends on the equation of state of the QGP and on the transport coefficients of the system providing constraints to models.

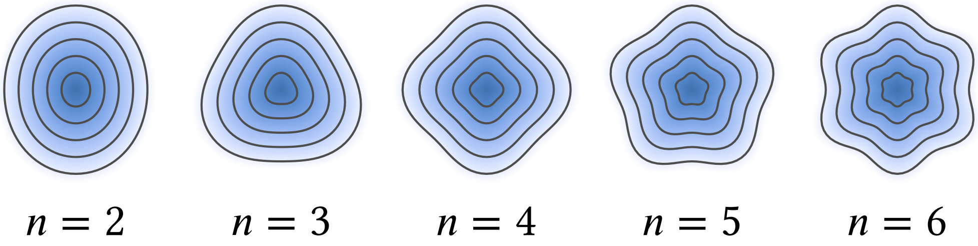

Figure 2.12: Different contributions of the Fourier harmonics to shape of the final-state particles. Figure taken from Ref. [59].

However, in the real-condition nuclear physics experiments, the impact parameter vector typically does not coincide with the short axis of this almond-shape region [60], which makes not really possible to use the participant plane to perform measurements. This happens because the nuclei has a finite number of particles whose positions are not uniformly distributed in the volume and its shape might depend in event-by-event properties. Since it is not possible to measure this plane, two sets of techniques can be used to handle this limitation. The first set relies on estimating the event plane, defined as the direction of maximum final-state particle density [60], which is currently discouraged [61]. The event plane method is affected by the resolution of the event plane determination which is detector dependent, making comparison between different experiments hard [61]. The other methods use two- and multi-particle correlations, as defined in Sec. 2.3.2, to try to remove the participant plane out of the problem. Starting with the two-particle correlations, the analyzed quantity in this method is the yield of pairs (N_{pair}) as function of the angular difference between the two particles ($\Delta\varphi = \varphi^a - \varphi^b$):

$$\frac{dN^{pairs}}{d\Delta\varphi} = f^{\text{non-flow}}(\Delta\varphi) + a(1 + \sum_{n=1}^{\infty} 2\; V_{n\Delta} \; \cos[n(\Delta\varphi + (\psi_n^a - \psi_n^b))]), \tag{2.11}$$

where $f^{\text{non-flow}}(\Delta\varphi)$ is the contribution coming from decays, jets and other terms that are not related to long-range correlations. The angles ψ_n^a and ψ_n^b are the ψ_n for particles a and b, respectively, and $V_{n\Delta}$ are the Fourrier coefficients. The first term is usually suppressed by imposing a pseudorapidity gap between the two particles or by using templates/measurements of the jet contributions. In case $\psi_n^a = \psi_n^b$, we can simplify the equation to

$$\frac{dN^{pairs}}{d\Delta\varphi} \propto 1 + \sum_{n=1}^{\infty} 2\ V_{n\Delta}\ \cos(n\Delta\varphi). \tag{2.12}$$

This last step is not granted, since particles a and b could be of different types of particles (for example, pions or kaons) or particles with different momentum ranges. In case $\psi_n^a = \psi_n^b$, we say that the factorization of the coefficients hold. The pair Fourier coefficient ($V_{n\Delta}$) is simply the product of the single particle coefficients (v_n) in this case:

$$V_{n\Delta} = v_n^a \times v_n^b. \tag{2.13}$$

The v_n obtained by two-particle correlations method can be directly measured by correlating identical particles:

$$v_n\{2PC\} = \sqrt{V_{n\Delta}} \tag{2.14}$$

That is straightforward for non-identified particles and after their v_2 is measured, the factorization is used to obtain the $v_2\{2PC\}$ for other particles. The use of factorization has been tested experimentally and also with model calculations and it seems to be valid mainly for low p_T particles [60, 62, 63].

More sophisticated two- and multi-particle correlation methods involve the scalar product method and cumulants. The scalar product [61, 64] divides each event into sub-events and the v_n is obtained as

$$v_n\{SP\} = \frac{\langle Q_n Q_{nA}^* \rangle}{\langle Q_{nA} Q_{nB}^* \rangle}, \tag{2.15}$$

where Q_n is the flow vector defined as the sum over the particles of interest ($Q_n = \frac{1}{N}\sum_j e^{in\varphi_j}$) and Q_{nA} and Q_{nB} are the reference flow coming from the sub events (usually obtained using reference detectors in a different η range). It is also common to impose a further separation in η to further remove contributions from short-range correlations, such as jets.

Other method, the cumulants, are also widely used to quantify the Fourier coefficients since their response to flow fluctuations (event-wise variations in the flow coefficients) and non-flow effects is considered well understood [65]. They rely on the calculation of the angular difference of two-particles and of the flow coefficients on an event-by-event basis. For a given n^{th}- harmonic coefficient (v_n), first we calculate its strength in a single event (the average is performed in a single event):

$$\langle 2 \rangle_n = \langle e^{in(\varphi_1 - \varphi_2)} \rangle, \tag{2.16}$$

where φ_1 and φ_2 come from different particles. Then the two-particle cumulant ($c_n\{2\}$) is calculated by averaging over an event ensemble:

$$c_n\{2\} = \langle \langle 2 \rangle_n \rangle = \langle \langle e^{in(\varphi_1 - \varphi_2)} \rangle \rangle, \tag{2.17}$$

where the inner mean is taken in a single event and the outer mean is with respect to the ensemble of events. In case there are no non-flow effects, the $c_n\{2\}$ coefficient corresponds to the measurement of $\langle v_n^2 \rangle$:

$$c_n\{2\} = \langle v_n^2 \rangle. \tag{2.18}$$

and then we can obtain coefficients using two-particle correlations ($v_n\{2\}$):

$$v_n\{2\} = \sqrt{c_n\{2\}}. \tag{2.19}$$

Similarly, we can similarly obtain the v_n using four-particle correlations, stating from

$$\langle 4 \rangle_n = \langle e^{in(\varphi_1 + \varphi_2 - \varphi_3 - \varphi_4)} \rangle, \tag{2.20}$$

and then calculating $c_n\{4\}$, removing the contributions of non-flow coming from the two-particle correlations [58, 64]:

$$c_n\{4\} = \langle \langle 4 \rangle_n \rangle - 2 \langle \langle 2 \rangle_n \rangle^2, \tag{2.21}$$

and we can extract the $v_n\{4\}$ using

$$v_n\{4\} = \sqrt[4]{-c_n\{4\}}. \tag{2.22}$$

We can also define six- and eight-particle (or even higher order) cumulants to further suppress non-flow effects. It is also possible to apply requirements on the minimum separations in η for the particles studied or even divide the event in other sub events to further suppress short-range correlations.

As one can notice by the methods mentioned here, measuring the elliptic flow is a challenging and several techniques were developed to better compare the theory and experimental results. The measurement of the v_2 quantifies the collective motion of the system, that we expect to reconnect to the hydrodynamic expansion of the medium created in the collisions, and it was performed as a function of different variables, such as centrality and transverse momentum.

One example of these measurements for unidentified charged particles in 2.76 TeV Pb–Pb collisions is shown in 2.13, in this case using two-particle correlations. We observe in the figure the different harmonics, one in each panel, as function of the transverse momentum (in the x axis) and centrality (represented by different colors). For the second harmonic, more central collisions have smaller v_2, while non-central ones have considerable v_2. This is compatible with the picture previously mentioned since the central collisions have a more circular geometry. For the higher order harmonics, the strength of the modulation has a much weaker dependence on the centrality, that reflects its nature related to the fluctuations of the initial state.

The mass dependence of the Fourier coefficients, as shown in Fig. 2.14, was studied as well. The hydrodynamic expansion of the medium leads to a mass ordering [66, 67], making lighter particles have a larger v_2 than heavier particles at the same p_T. This can be observed for $p_T <$ 2-3 GeV/c for all centralities. This phenomenon is understood in terms of a strong radial flow, which imposes an equal and isotropic velocity boost to all particles added to the anisotropic medium expansion [68]. At intermediate p_T ($3 < p_T <$8-10 GeV/c), the mesons and baryons form different groups, which is likely not related to the collective expansion of the medium. This shows the role of quark coalescence in the particle production in high-energy Pb-Pb collisions [69].

As discussed for the nuclear modification factor, it is interesting to compare the observables for both soft and hard probes. The results illustrated in Fig. 2.14 already show a few of those results, since the v_2 coefficients are presented up to $p_T \approx 14$ GeV/c. For the high-momentum particles, the non-zero v_2 is explained by the energy loss due to multiple scattering and gluon radiation [70, 71]. But we are also interested to understand if the mass ordering present for particles in the light-flavor sector is also present for heavy particles. This is done by measuring the D-meson v_2 and v_3, reported in Fig. 2.15. In this figure, the charged particles v_2 and v_3 is also shown for comparison. The

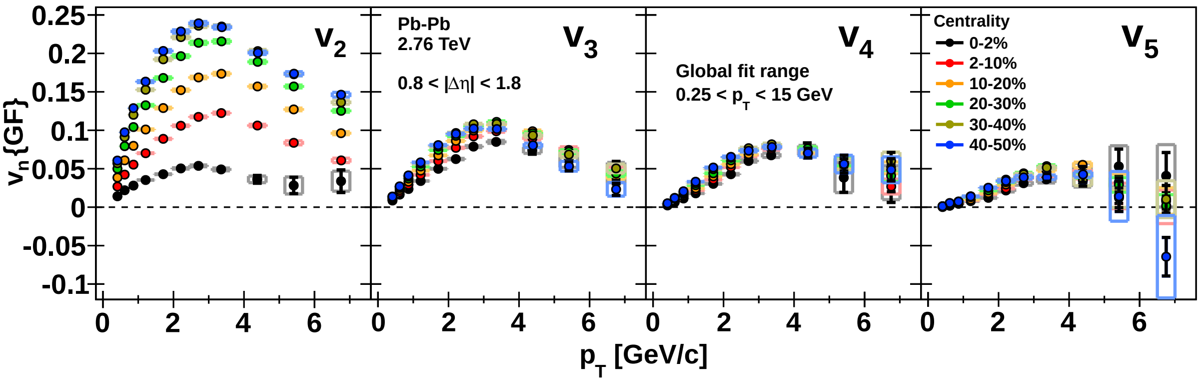

Figure 2.13: Fourier coefficients (v_n) obtained for order $2 \leq n \leq 5$ in Pb-Pb collisions at $\sqrt{s_{\rm NN}} = 2.76$ TeV by the ALICE Collaboration. The values are obtained using a global fit that takes into account different p_T combinations. Figure taken from Ref. [63].

p_T dependence is very similar for charged particles and D mesons, which are also similar to the trends to the results from Fig. 2.13 and 2.14. For D mesons with $p_T < 6\,\mathrm{GeV}/c$ and centrality classes 10-30% and 30-50%, the strength of the v_2 and v_3 coefficients are smaller than those for charged particles. This is consistent with the mass ordering observed for light-flavor particles, but more studies are necessary to determine whether other effects, for example, the degree of charm quark thermalization, coalescence, and the path length dependence of energy loss, are also relevant in this scenario.

Both hard and soft probes show considerable flow in Pb-Pb collisions, as expected in a hydrodynamic expansion of the medium. More studies are necessary, mainly in the hard sector, to further interpret the results obtained. The measurement of the elliptic flow reported in this section, combined with the measurement of the nuclear modification factor and the jet suppression, point to the formation of the QGP in heavy-ion collisions. Other observables are also used and point to similar conclusions, as it will be discussed in the next section.

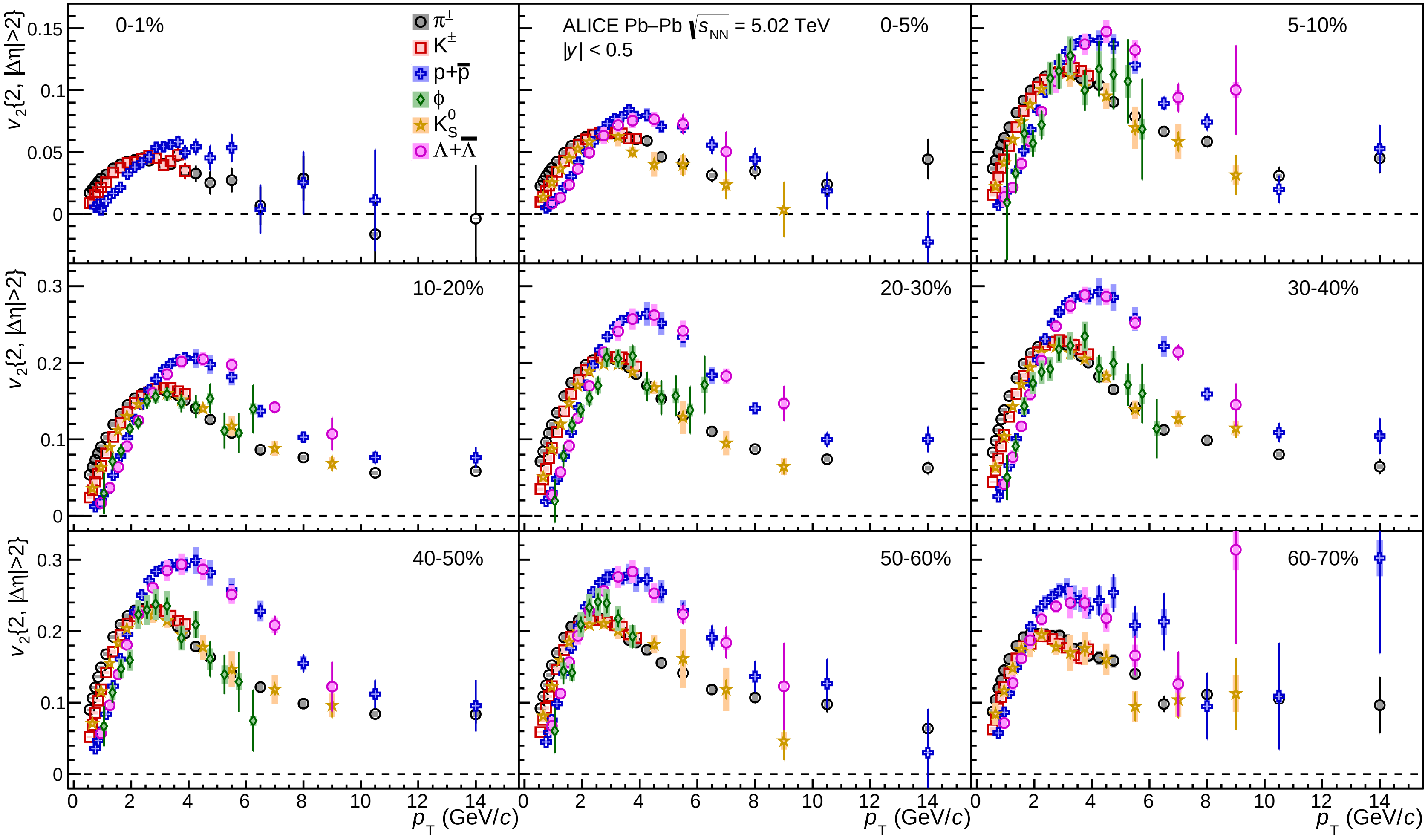

Figure 2.14: Identified particle v_2 for different centrality classes obtained using the scalar product method by the ALICE Collaboration. Figure taken from Ref. [68].

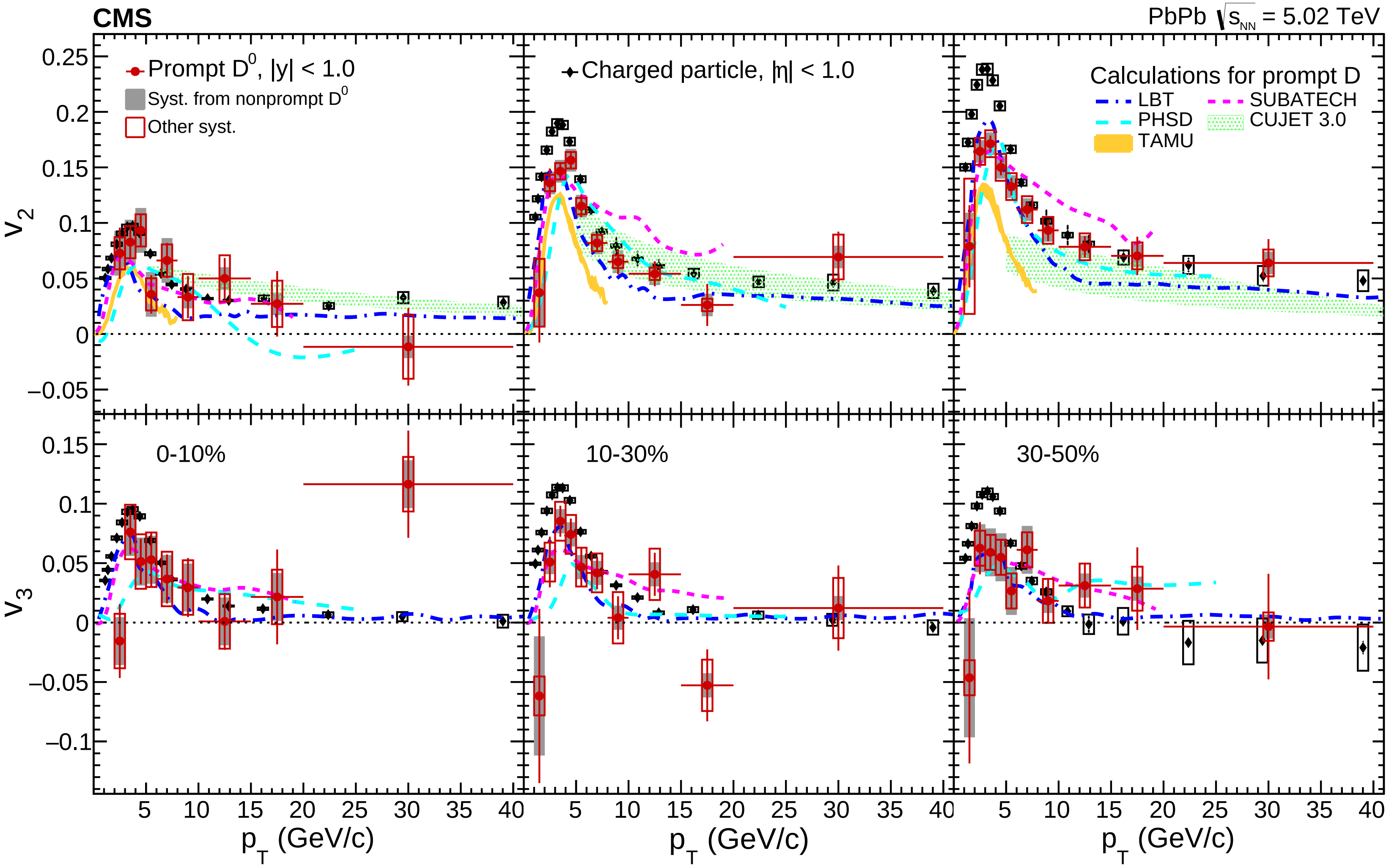

Figure 2.15: D^0 meson v_2 (upper) and v_3 (lower) coefficients at midrapidity ($|y| < 1.0$) for the centrality classes 0-10% (left), 10-30% (middle), and 30-50% (right). The v_n coefficients of charged particles at mid pseudorapidity ($\eta < 1.0$) and theoretical calculations for D meson v_n coefficient are also presented for comparison. Figure taken from Ref. [72], where the citation for the models are also given.

2.3.4 Other evidence for the QGP formation

There is a large number of observables that are used to quantify the properties of the QGP. Here only three of the most important ones where covered: the nuclear modification factor of charged particles and heavy flavors, the jet suppression measured using two-particle correlations and the elliptic flow. Other measurements that are very important for the QGP studies include electroweak probes, quarkonium formation, and strangeness enhancement.

Electroweak probes

Examples of hard electromagnetic probes are prompt photons and W/Z bosons. These particles do not interact with the QGP by the strong force since they do not have color charge. They are a reference to test the assumptions made about the geometry and to measure cold matter nuclear effects. As an example, Figures 2.16 and 2.17 show the R_{AA} of Z bosons as a function of the number of participants in Pb–Pb collisions at two different energies. The nuclear modification factor is compatible with unity in all the range studied. In particular, in central collisions (large N_{part} values) the measurement is very close to one. This is compatible with the picture that the QGP only interacts with colored particles. The ALICE collaboration has also performed similar measurements of electromagnetic probes [39].

On the other hand, the soft electroweak probes are thermal photons and di-electrons that are produced in the evolution of the collision and are sensitive to the thermal radiation of the system. They also give information about the temperature and energy density of the system. Just after they are produced, they decouple from the QGP, since they are color neutral. A few results are reported on Refs. [73–75]. Given the huge background present in this measurements, it is challenging to draw final conclusions.

Quarkonium

Quarkonium states, formed by $c\bar{c}$ and $b\bar{b}$ pairs, allow the study of bound states containing heavy quarks. Each quarkonia state dissociates at different temperatures, in an effect called sequential suppression [76]. This creates the possibility of using quarkonium production measurements as a thermometer of the medium [77]. These measurements are affected by regeneration (where pairs are formed in the late stages of the collision), medium-induced energy loss, and other effects. It is necessary to study these all these effects carefully. Nevertheless, the current measurements point to the sequential suppression. This can be seen in the different R_{AA} values for J/ψ and $\psi(2S)$ ($c\bar{c}$ states) in Fig. 2.18. The suppression of bottomonium (Υ, $b\bar{b}$ states) has also been measured, as shown in Fig. 2.19. Similar results concerning the order of the suppression were also found for Υ as shown in Ref. [78].

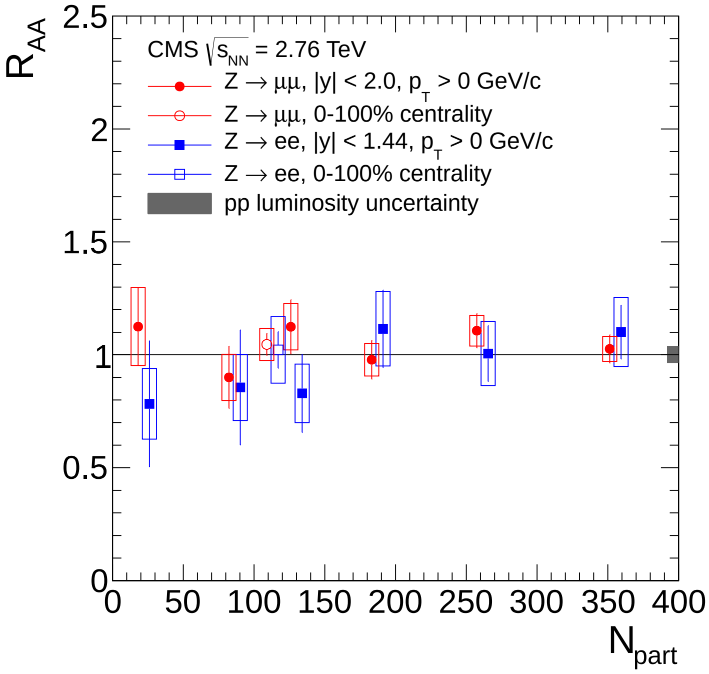

Figure 2.16: R_{AA} distribution for Z bosons, $Z \to e^+e^-$ (blue squares) and $Z \to \mu^+\mu^-$ (red circles) events as a function of the number of participants (N_{part}) in 2.76 TeV Pb–Pb collisions. Open points at $N_{\text{part}} \sim 110$ represent the centrality-integrated R_{AA}. Figure taken from Ref. [79].

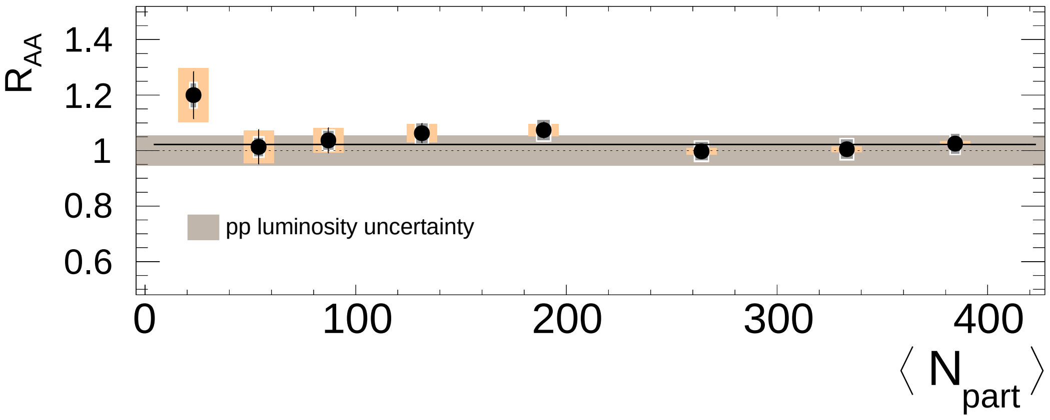

Figure 2.17: R_{AA} distribution for Z bosons in the di-muon decay channel as a function of the number of participants (N_{part}) in Pb–Pb collisions at $\sqrt{s_{\text{NN}}}$ = 5.02 TeV measured by the ATLAS collaboration. The orange uncertainties represent the uncertainties coming from the normalization factor (T_{AA}). Figure taken from Ref. [42].

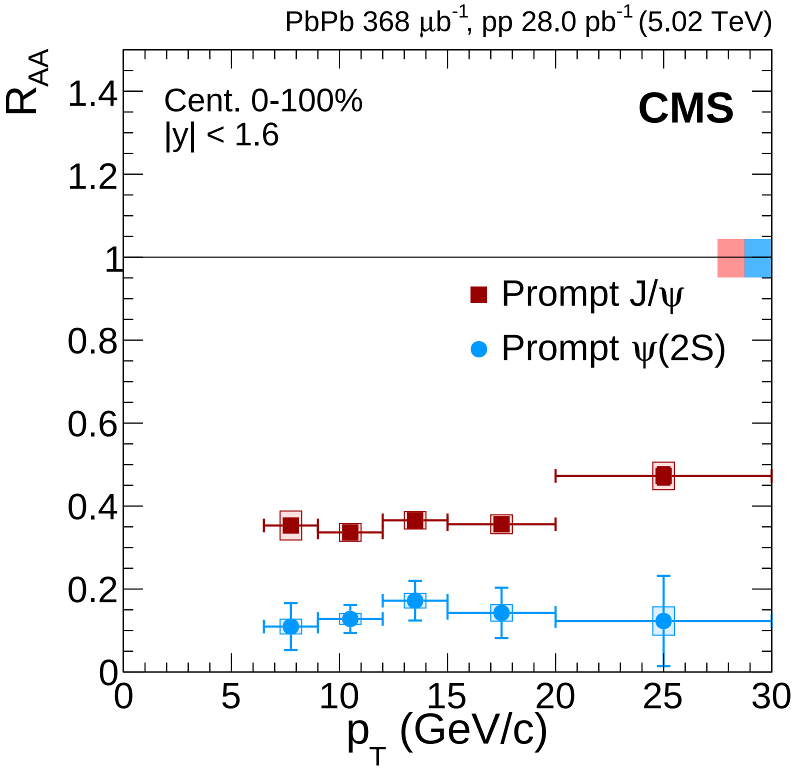

Figure 2.18: Nuclear modification factor of prompt J/ψ and $\psi(2S)$ mesons as a function of p_T in Pb–Pb collisions at $\sqrt{s_{\mathrm{NN}}}$ = 5.02 TeV measured by the CMS collaboration. Figure taken from Ref. [43]

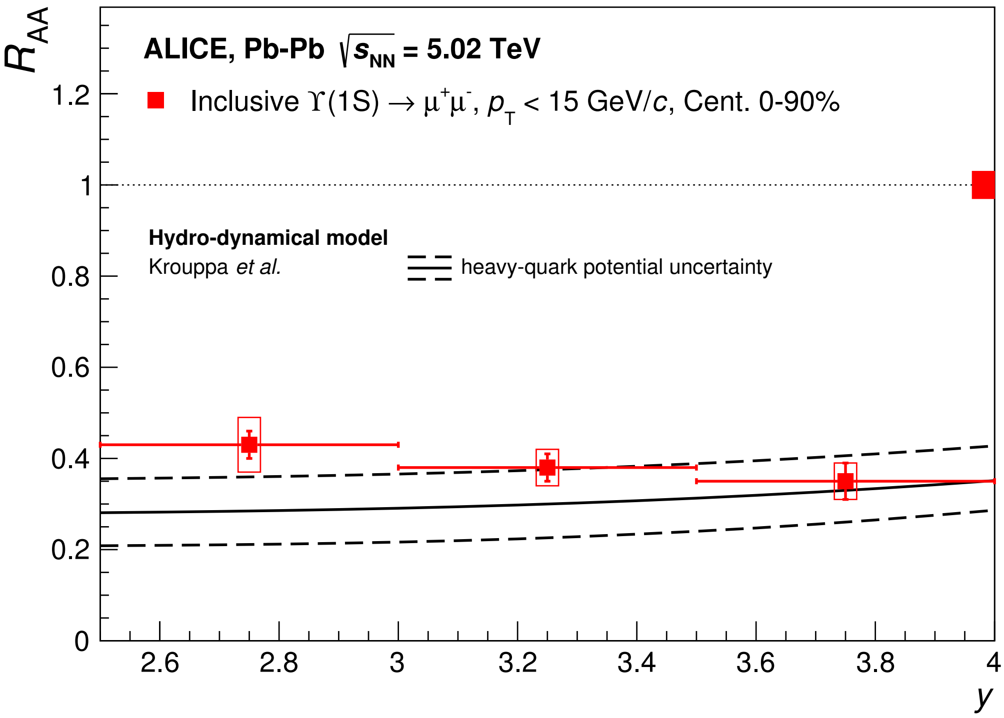

Figure 2.19: Nuclear modification factor of inclusive$\Upsilon(1S)$ mesons at forward rapidity as a function of y measured by the ALICE collaboration in Pb–Pb collisions at $\sqrt{s_{\mathrm{NN}}}$ = 5.02 TeV. Figure taken from Ref. [80]

Strangeness enhancement

Strangeness enhancement has been considered a signature of the QGP since the 1980s [81]. It was believed to be a precise signature of the formation of the QGP, but this has changed over the years. It is still not clear the microscopical mechanism which brings the system produced in heavy-ion collisions to enhance strangeness. Recent results [82] show that the strange mesons and baryons are enhanced in Pb–Pb collisions. But results in small systems have very interesting and similar signatures, which will be discussed in the next chapter.

2.4 Chapter summary

In this chapter, the different aspects of the quark-gluon plasma have been briefly discussed. From the first section, the Quantum Chromodynamics was introduced. It is the underlying theory behind the Quark-Gluon Plasma and has two important properties: the asymptotic freedom and confinement. The state that quarks and gluons are no longer confined in hadrons is called quark-gluon-plasma. This state is created in the laboratory using particle accelerators with beams of heavy ions. Different measurements support the formation of the QGP. The nuclear modification factor is suppressed for high p_T particle yields. This is an indication that the particles lose energy when transversing the medium. Additional evidence in the sequential suppression of quarkonium ($c\bar{c}$ and $b\bar{b}$) states were also found. The second Fourier coefficient of the particle azimuthal distribution, called elliptic flow, has been measured for different particles and was found to be positive with a mass ordering. The hydrodynamic evolution of the system translates the anisotropy in the geometry into the momentum anisotropy. Jets were also found to be suppressed and strange particles found to be enhanced due to the interaction with the medium. All those measurements and many more support the formation of the quark-gluon plasma in heavy-ion collisions. Its production is almost a consensus in the high-energy nuclear physics community. However, measurements from small collision systems have similar results as the one seen in heavy-ion collisions and they will be discussed in the next chapter.

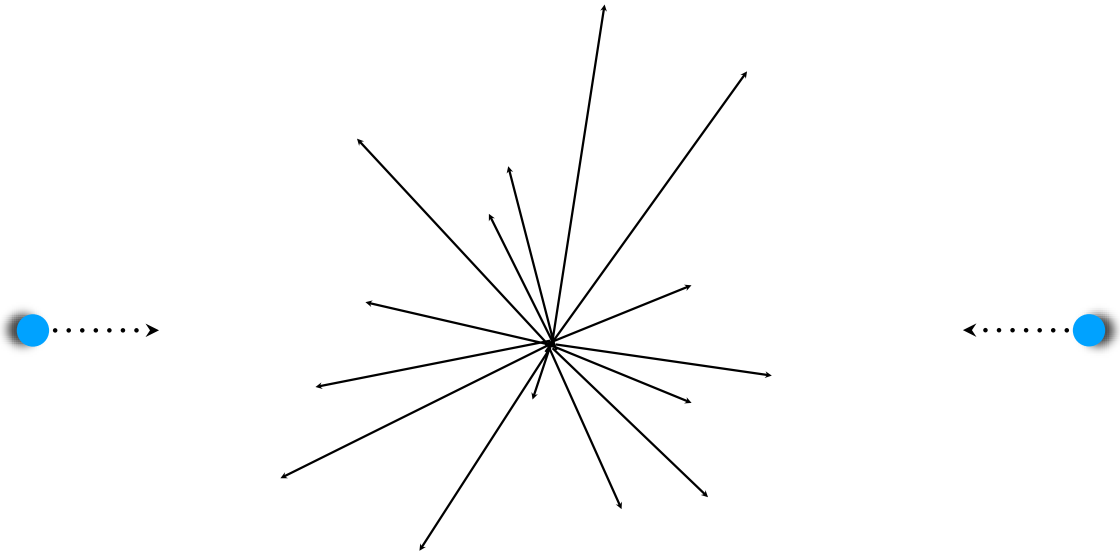

3 — Small systems

The extensive measurements in heavy-ion collisions have pointed to signatures of the Quark-Gluon Plasma. These signatures have been compared to models that use hydrodynamic calculations to describe the evolution of the medium created in those collisions. In both experimental and theoretical aspects, all the evidence point to the formation of this dense and hot medium in heavy-ion collisions.

Nevertheless, a few of those signatures have been found in small collision systems as well, such as pp and p–Pb collisions. We have observed azimuthal anisotropy and strangeness enhancement in those collision systems. Studies of two-particle correlations have shown a long-range double-ridge structure, that resembles the one in Pb–Pb collisions, as it will be discussed on Sec. 3.1. The studies of multi-particle correlations, reported on Sec. 3.2, point that the azimuthal anisotropy is present even when taking the correlations between 6 or 8 particles. These results are not expected and their origin is highly debated in the community, as it is briefly discussed on Sec 3.3. The role of the initial-state and final-state effects on the azimuthal anisotropy is an interesting research question that might not even be related to the Quark-Gluon Plasma. In any case, it shows the incomplete understanding of the state-of-art event generators. The strangeness enhancement is also present in all collision systems studied and its microscopic origin is still under discussion as reported in Sec. 3.4.

3.1 Observation of a double-ridge structure

As explained in Chapter 2, two-particle azimuthal correlations distributions in non-central nucleus-nucleus collisions have a contribution due to a non-zero elliptic flow (v_2). This is translated in the correlation distribution as a double ridge structure. In this case, the elliptic flow is connected to the presence of a collective motion generated by the hydrodynamic expansion that translates the spatial anisotropy into momentum anisotropy. The positive v_2 has been considered a strong signal of collectivity and of the formation of the QGP [83].

Surprisingly, similar long-range ridge structures have also been found in small systems and a positive v_2 coefficient was observed in high-multiplicity pp and p–Pb collisions at the LHC. This novel featured observation starts with the measurement of a long-range, near-side angular correlation by the CMS collaboration in pp collisions at different energies in a paper from 2010 [84]. It is possible to observe the differences between minimum bias and high multiplicity pp collisions in the correlation distributions from Fig. 3.1. On the top, Fig. 3.1a and 3.1b, the minimum-bias correlation distribution is shown and it has the characteristic near-side peak. There is also a broader structure in the away side, linked to the away-side jet. On the bottom, Fig. 3.1c and 3.1d, the high-multiplicity correlation distribution has the same features, but a long-range near-side structure is clearly present (mainly in Fig. 3.1d). In this paper, CMS also compares this features to different state-of-art event generators, such as PYTHIA 8 [85] and PYTHIA 6 [86] with different tunes, HERWIG++ [87] and Madgraph [88]. But none of them seem to describe this near-side correlations corresponding to those seen in data, although the other parts of the correlation distribution were qualitatively modeled.

The double-rigde structure was also observed by ATLAS in pp collisions [89]. Similar structure was also reported in p–Pb collisions by ALICE [90], ATLAS [91] and CMS [92] and in d–Au collisions by PHENIX [93] and STAR [94].

One technique developed to better analyze the near-side structure is the subtraction of the jet contribution using templates or the correlation distribution from low-multiplicity collisions. This comes with the underlying assumption that these distributions do not have a significant flow contribution and that the jet contribution to the correlation function is similar in different multiplicities. It is important to stress that even in case the v_2 contribution from low multiplicities is non-negligible but the jet component is similar in different multiplicities, this method still gives a significant result for the presence of long-range correlations because the v_2 is an additive quantity. So in case we subtract the low multiplicity results, the measured v_2 value would be in fact the v_2 in the measured multiplicity minus the low-multiplicity v_2, scaled by the different multiplicities in each multiplicity range. In this case, the conclusion of the

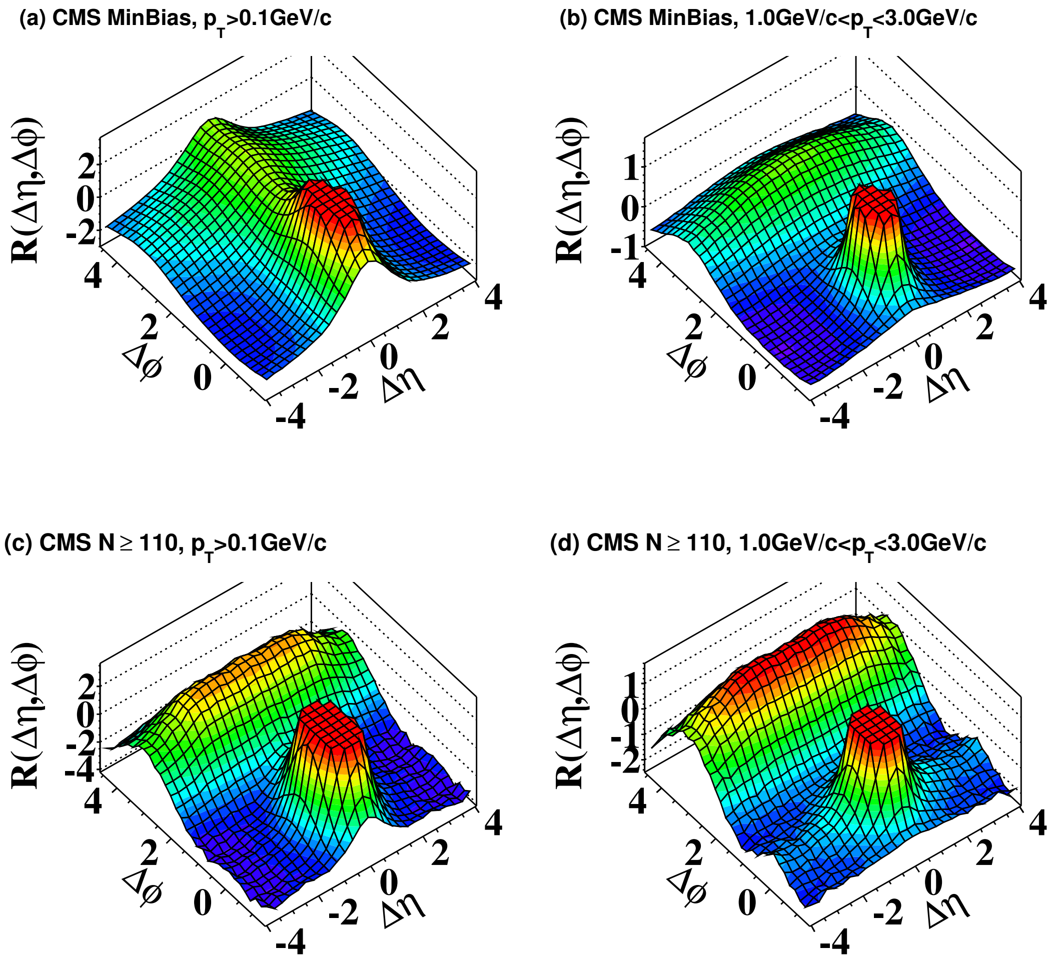
(a) CMS MinBias, p_T>0.1GeV/c

(b) CMS MinBias, 1.0GeV/c<p_T<3.0GeV/c

(c) CMS N ≥ 110, p_T>0.1GeV/c

(d) CMS N ≥ 110, 1.0GeV/c<p_T<3.0GeV/c

Figure 3.1: Two-particle correlation function in pp collisions at $\sqrt{s_{NN}} = 7$ TeV measured by the CMS Collaboration in minimum bias events with $p_{\mathrm{T}} > 0.1$ GeV/c (a) and with $1 < p_{\mathrm{T}} < 3$ GeV/c (b); and in high multiplicity (more than 110 reconstructed tracks) with $p_{\mathrm{T}} > 0.1$ GeV/c (a) and with $1 < p_{\mathrm{T}} < 3$ GeV/c (b). The sharp near-side peak from jet correlations was cut off in to better visualize the structure outside that region. Figure taken from [84].

presence of long-range structures would remain unchanged, although the v_2 in low-multiplicity would have to be obtained using a different method.

An example of the application of the subtraction method is presented in Figure 3.2. In this case, the low-multiplicity correlation distribution is subtracted from the high-multiplicity one to suppress the jet contribution. On the top panel of Fig. 3.2, the two-dimensional correlation distribution in $\Delta\eta$ and $\Delta\varphi$ is shown. In this case, it is possible to see a peak around $\Delta\varphi \approx 0$ and $\Delta\eta \approx 0$ for pions that is likely a remaining jet contribution coming from modifications of the jet structure in low- and high-multiplicity collisions. The remaining jet contribution in the protons is not visible, but this is probably a statistical limitation. In both cases, it is possible to observe a long-range structure in $\Delta\eta$. Its shape is dominated by the second-order Fourier coefficient. This decomposition is further studied in the bottom panel where the correlation is projected onto $\Delta\varphi$ using different $\Delta\eta$ ranges for the near and away side. The fit confirms that the second-order coefficient is dominant, but a non-negligible contribution from the third component is also obtained. The comparison of the different obtained v_2 values for the different species is shown on Fig. 3.3. A particle mass dependence of the v_2 coefficient is observed and it is qualitatively similar to the one observed in nucleus-nucleus collisions. This is one of the reasons behind the inspiration to use models where a small QGP is formed to explain this data.

Other measurements at the LHC [91] have also studied the long-range structure in p–Pb and pp collisions using similar techniques. The ATLAS Collaboration employs a template fit to remove the contribution of jets in the correlation and has also very precise results in small systems [89]. The fit template method is an analogous to the procedure used by ALICE [95] and similar assumptions are made, such as a small change

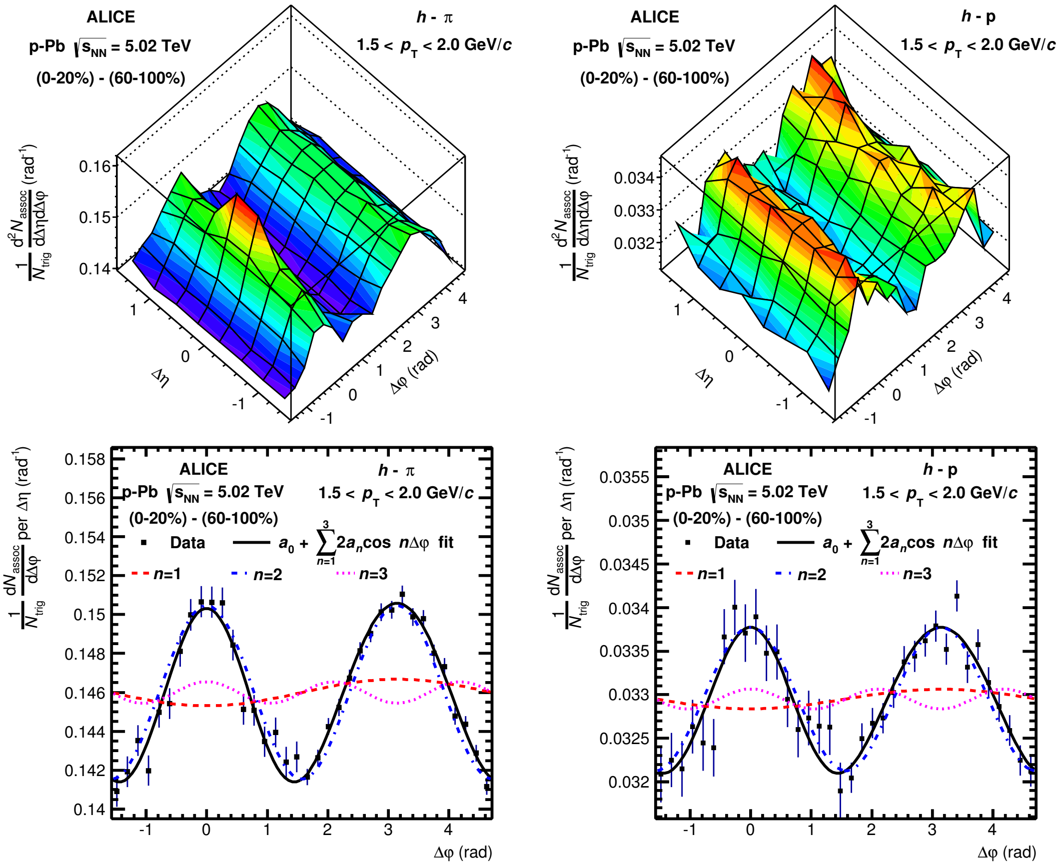

Figure 3.2: Two-particle correlation function for the 0-20% V0A classes (high multiplicity) subtracted from the 60-100% V0A classes for charged particles and charged pions/protons. On the bottom the projection to the $\Delta\varphi$ axis is calculated using weighted averages. The $\Delta\eta$ interval used is $0.8 < |\Delta\eta| < 1.6$ for $-\pi/2 < \Delta\varphi < \pi/2$ rad and $|\Delta\eta| < 1.6$ for $\pi/2 < \Delta\varphi < 3\pi/2$ rad. Figure from [95].

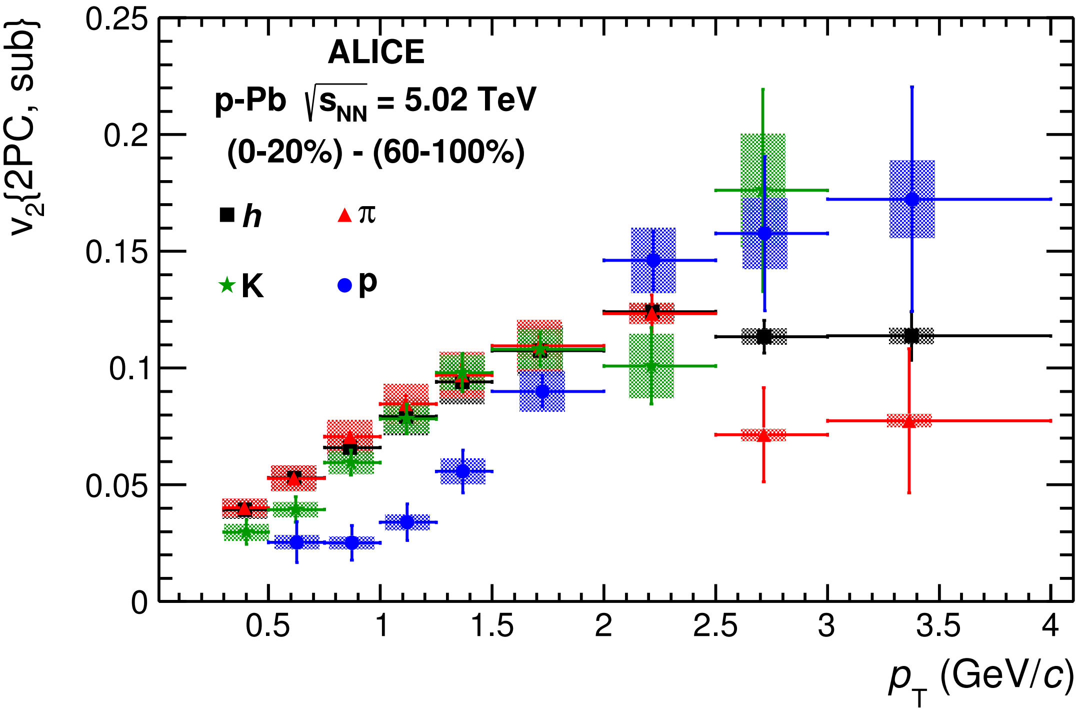

Figure 3.3: Fourier coefficient v_2 for hadrons, pions, kaons and protons as a function of p_{T} from the correlation in the 0-20% multiplicity class after subtraction of the correlation from the 60-100% multiplicity class in p–Pb collisions at $\sqrt{s_{\mathrm{NN}}}$ = 5.02 TeV. Figure taken from [95].

in the jet contribution from low- to high- and intermediate-multiplicity collisions. This assumption is much more reasonable because a very large veto is imposed in the $\Delta\eta$ of the pairs ($|\Delta\eta| > 2$) to remove the near-side jet structure. The template is built with the correlation from low-multiplicity collisions and it is used in to in the fit together with the Fourier components. An example of this method is shown in Fig. 3.4 and 3.5 for pp collisions at 13 TeV. The red line represents the total fit using both information from the template obtained in low multiplicity collisions (open black dots) and the Fourier component (blue dashed lines). After performing the fits, the conclusion is again the evidence for long-range correlations in small systems.

These are only a selection of measurements that reveal that the v_2 coefficient is present in pp and p–Pb collisions for light-flavoured hadrons. Further studies using multi-particle cumulants have been also performed in these collision systems and they will be further discussed on the next section.

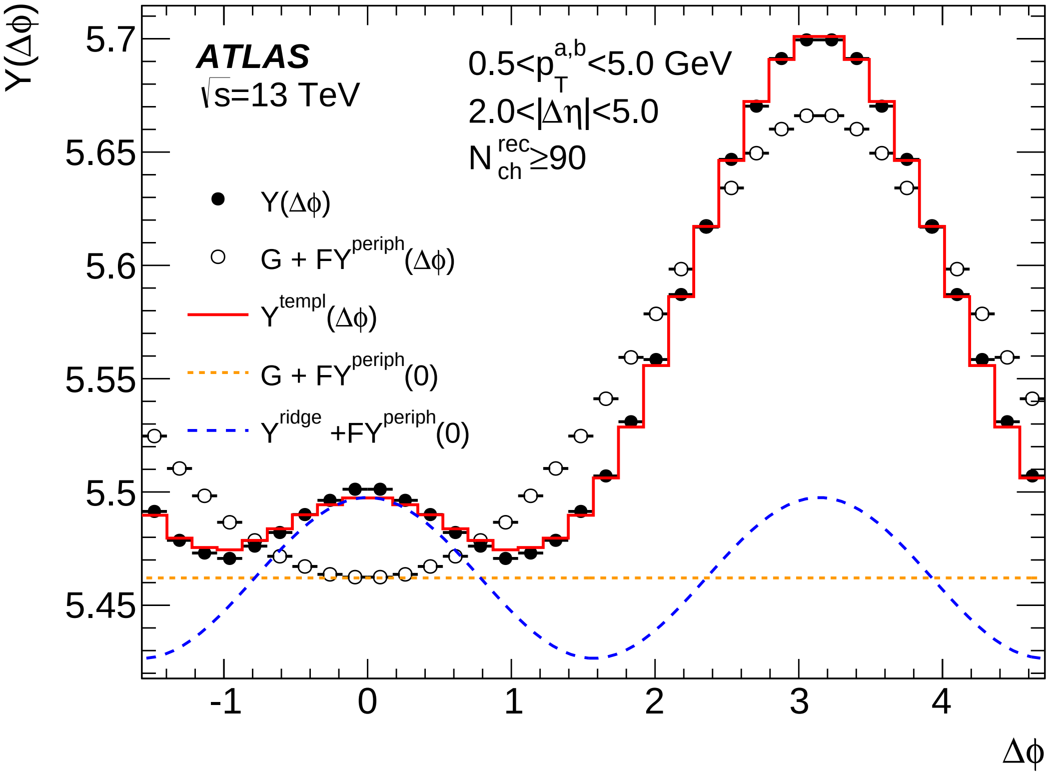

Figure 3.4: Fit of the two-particle correlation in 13 TeV pp collisions for charged particles with $0.5 < p_\mathrm{T} < 5$ GeV/c and $2 < |\Delta\eta| < 5$. The template used to estimate the jet contribution is shown in open black dots and the Fourier coefficients in dashed blue lines. Figure taken from the additional material of Ref. [89].

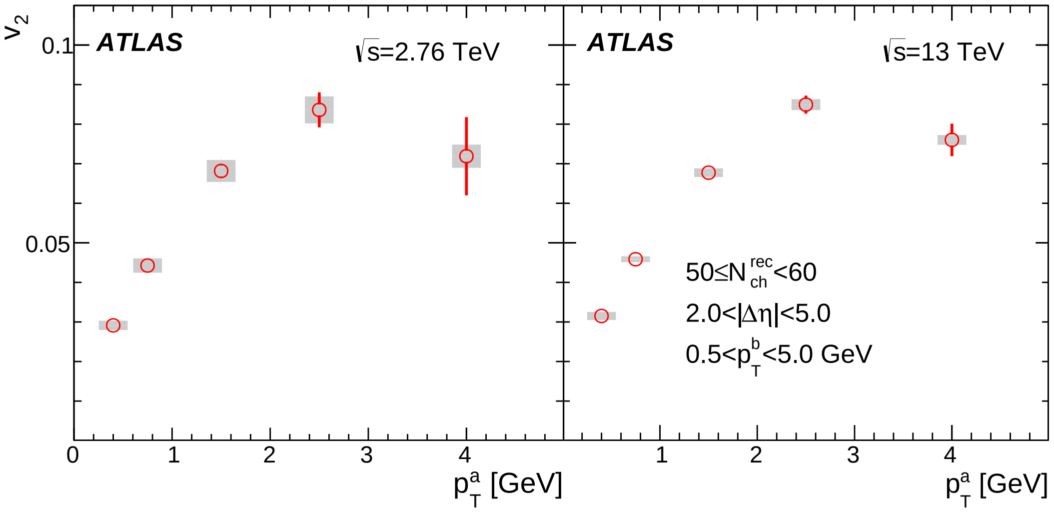

Figure 3.5: Fourier coefficient v_2 for charged particles in pp collisions at 2.76 TeV (left) and 13 TeV (right) obtained using fit templates. Figure taken from the additional material of Ref. [89].

3.2 Multi-particle correlations

As discussed on Sec. 2.3.3, multi-particle cumulants are used to calculate the Fourier coefficients of the azimuthal particle distributions. They can analytically suppress non-flow effects by subtracting correlations coming from fewer particles than the number of particles that are correlated. They are especially important in small systems to understand the bias of non-flow effects, such as jets and resonances, on the effects reported on the previous section. Similarly to heavy-ion collisions, the elliptic flow is also studied in pp and p–Pb collisions using multi-particle cumulants [96–100]. That is a natural extension of the studies reported in the previous section and it adds more information about the nature of the possible collective effects.

An example of such studies is shown in Fig. 3.6. The v_2 coefficient is calculated using correlations between two, four, six, and eight particles in p–Pb and Pb–Pb collisions in a broad multiplicity range. The higher-order cumulants are expected to further suppress non-flow contributions and the subtraction using low-multiplicity events is not performed. The v_2 should converge to a similar value in case the non-flow contributions and the flow fluctuations are low. The v_2 values obtained with a different number of particles are compatible within ±10% in p–Pb collisions and within ±2% for Pb–Pb collisions. This agreement supports the collective nature of the observed correlations rather than a jet-related origin. The measured values indicate that the correlations are more likely to come from a common mechanism that involves all the particles and dis-

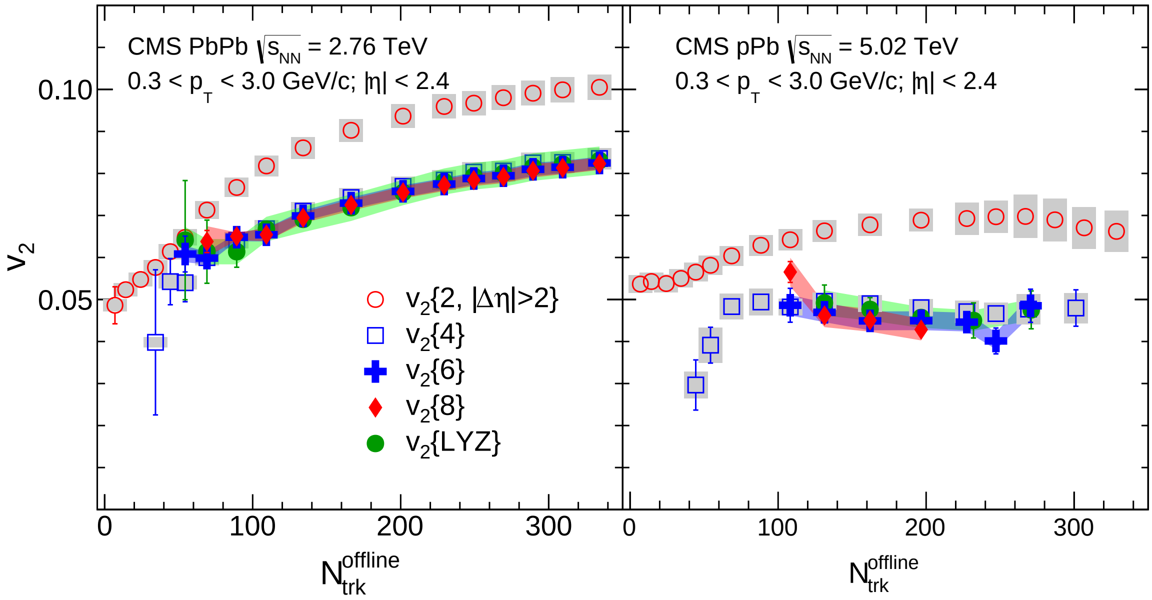

Figure 3.6: CMS results for the v_2 coefficient using multi-particle cumulants as a function of the number of reconstructed tracks ($N_{\mathrm{trk}}^{\mathrm{offline}}$) for Pb–Pb (left) and p–Pb (right) collisions. Figure from Ref. [97].

favor interpretations linked to few-particle correlations such as jets. The ALICE and ATLAS collaborations reported similar measurements that further agree with these results [65, 101].

3.3 Theoretical models of the azimuthal anisotropies in small systems

The theoretical description of the long-range structure in small collision systems, quantified by the v_2 harmonic, is still under debate. The interpretation is challenging since the R_{pPb} is compatible with unity for p–Pb collisions and that no jet suppression has been found. But it is important to stress that the current precision of the R_{pPb} measurements cannot rule out a suppression of a few percents, given the systematical uncertainties. The meaning of the measured v_2 in pp collisions is even more challenging given the small system size.

There are multiple approaches to explain these findings. One approach uses a similar formalism as the one in heavy-ion collisions, using final-state effects. A hydrodynamic evolution, which resembles a small QGP evolution, is used to simulate the high-multiplicity events. An example of calculation using a hydrodynamics is shown in Fig. 3.7. A few other models that include hydrodynamical calculations can be found

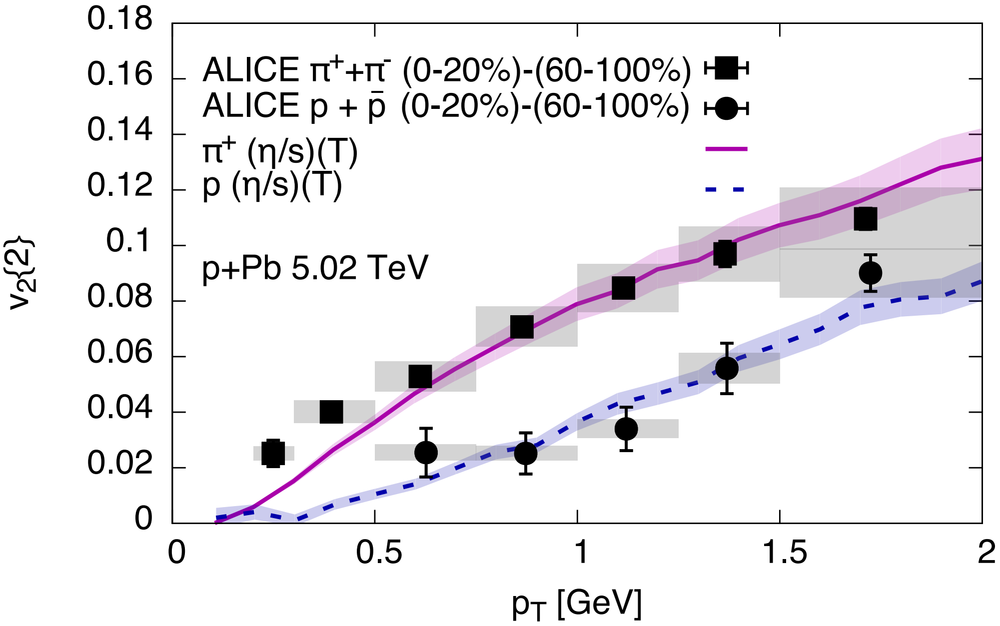

Figure 3.7: Comparison of the second harmonic between experimental data from ALICE [95] and predictions using a model that includes a hydrodynamic evolution using MUSIC [102] in p–Pb collisions. Figure taken from Ref. [103].

in Refs. [104–106]. The v_n harmonics are generated due to the geometry-induced collective flow in those models. The hydrodynamic approach successfully describes the p_T integrated v_2 as function of the multiplicity, the p_T-differential v_2, and the mass dependence of the v_2. Although the models involving hydrodynamics successfully reproduce the experimental data, they need additional parameters to tune on and other details of the models might be questionable. Lots of questions are also raised concerning the reliability of this description in small and out-of-equilibrium systems. Another point is how to know if the viscous corrections are under control. This and other concerns are reported in Ref. [107] and [108]. Even though there are many caveats in the application of hydrodynamic models in small systems, the description given by those models is undeniably helpful and provide some physical interpretation for this phenomena. There is no consensus yet, but one may think that the agreement between the hydrodynamic models and experimental data of small systems suggests a geometry-driven collective expansion at much lower multiplicities than one would expect [107].

Transport models, such as BAMPS [109] and AMPT [110], have also been considered to explain the data. BAMPS considers only gluons quasiparticles with a few scattering possibilities and it can produce the flow patterns in the limit of multiple collisions. BAMPS can qualitatively describe the anisotropic flow as shown in Ref. [111], but more studies are necessary to have the calculations under control. AMPT has different assumptions and it uses massless quark and antiquark quasiparticles to describe the interactions, but no gluons are considered in the initial state. The quarks can hadronize via coalescence and the produced hadrons can rescatter at later stages. One example of calculations using AMPT is shown in Fig. 3.8, where it is compared to p–Pb and Pb–Pb data from CMS [57]. For p–Pb collisions the agreement between the

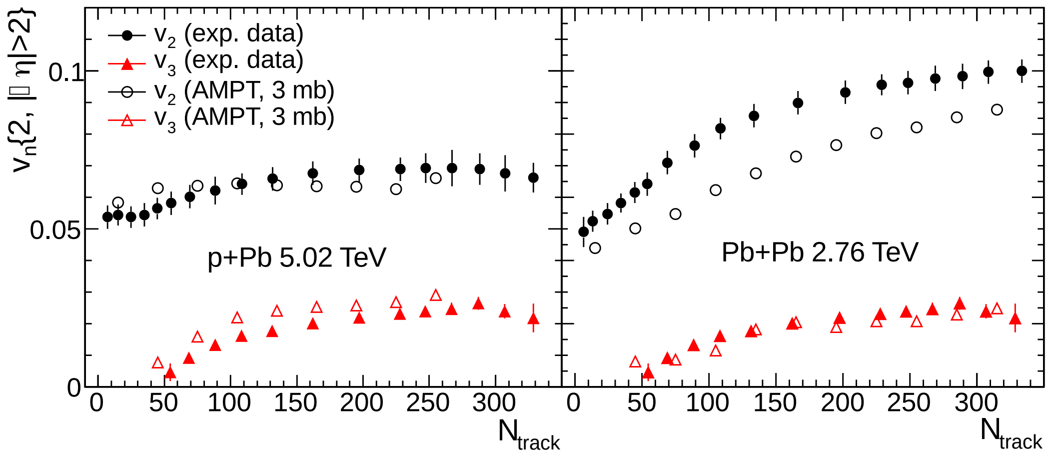

Figure 3.8: Comparison of the second harmonic as a function of the charged particle multiplicity between experimental data from CMS [57] and predictions using AMPT in p–Pb collisions. Figure taken from [112].

v_2 from AMPT and from the data is better than in Pb–Pb collisions, although no systematic uncertainties for the model are quoted. That is expected since the parameters of the model were tuned based on p–Pb collisions. Interpreting the results with AMPT is complicated since it includes non-physical assumptions, such as the absence of gluons. Nevertheless, it is possible to generate anisotropies using the transport models as it was in hydrodynamic models. This is not a contradicting picture since the hydrodynamic evolution can be understood as an efficient approximation to the full kinetic evolution depending on the path length and number of particles [107].

Another possibility is that the anisotropy could come from the initial-state correlations. The incoming nuclei can have correlations between their wave functions, coming from interactions. That could deflect the substructures of the incoming particle, generating anisotropies on an event-by-event basis. A few of those models are described in Refs [113, 114]. More recent calculations can generate any harmonic using initial-state correlations and even the mass ordering can be obtained. The indications that it is possible to generate a mass dependence of the v_2 using only initial-conditions is a striking result. That was believed to be a clear sign of the hydrodynamic collective flow. As a final remark about the models which use initial-state effects, they can reproduce the trend of the v_2 qualitatively, but more work is necessary for a quantitative comparison. The understanding of the v_2 in small systems will greatly benefit from the future progresses of this studies.

3.4 Strangeness Enhancement

Strange quarks are not present in the valence quarks of protons and/or nuclei, the initial state of the collisions, but they have a small mass which allows their abundant production. At high transverse momentum, they come from the initial states processes, such as flavor creation, and from stages after the collision, such as gluon splitting. At low momentum, they are mostly produced by non-perturbative processes. In heavy-ion collisions, the measurements of the ratio strange/non-strange particles are usually described by statistical models that consider a hadron gas in thermal and chemical equilibrium [115, 116]. Its microscopical interpretation is not straightforward, even in Pb–Pb collisions, and the origin of enhanced strangeness production is not known [82], but it is usually linked to the QGP.

As it happened for the elliptic flow in the previous section, similar measurements of the ratio of strange/non-strange particle productions have interesting results that resemble the ones in heavy-ion collisions. This result is presented in Fig. 3.9, where the ratios of the p_T integrated yields for K^0_s, Λ, Ξ and Ω divided by the π one are shown. . An enhancement of strange to non-strange hadron production as a function of multiplicity is found in pp and p–Pb collisions. The values are also similar to Pb–Pb colli-

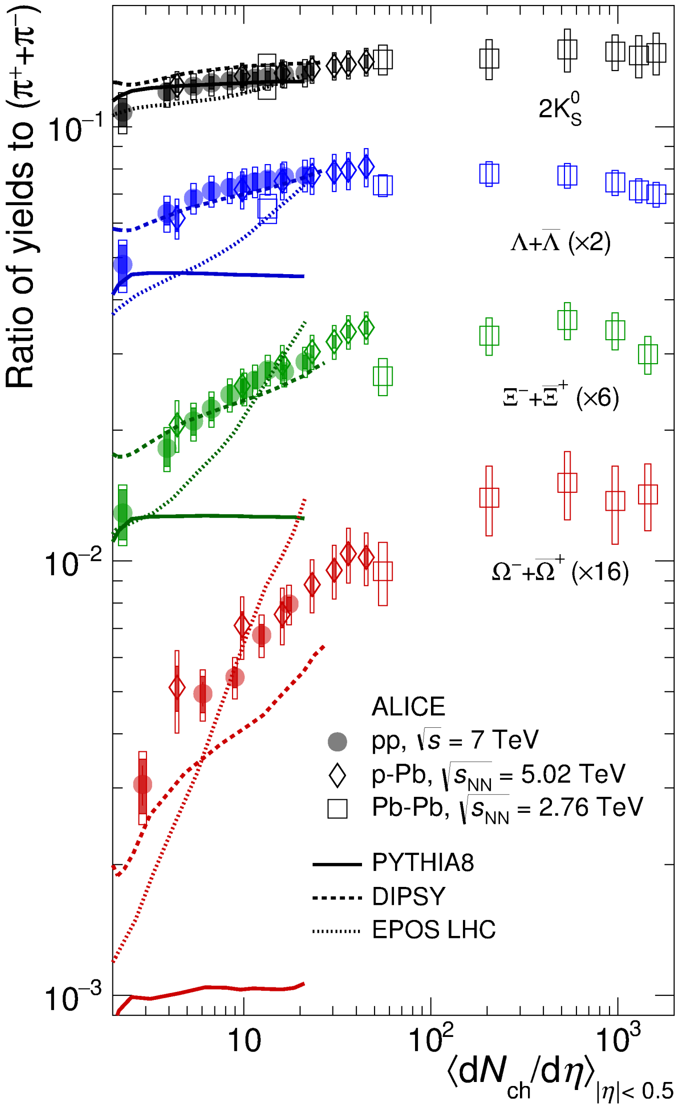

Figure 3.9: Integrated yield ratios to pions as function of the average number of particles at mid-rapidity for different collision systems. The results are compared to models, that are refered in [82].

sions in the overlapping multiplicities. No significant energy and system dependence are found. The comparison to standard event generators, such as PYTHIA [85, 86], points that the data is not well described by them. The data is well described by DIPSY [117], where the interaction between gluonic strings is allowed to form color ropes. In the model, it these color ropes are expected to produce more strange particles and baryons. The production of strange particles is apparently driven by the final-state effects rather than by the collision system or energy. This is further suggested by the fact that the particle ratios are identical in pp and p–Pb collisions at similar multiplicity. In Ref. [82], the ratios of non-strange to non-strange particles are also examined and they do not have similar features.

To check if the number of strange quarks plays a role in this enhancement, the ratios are normalized by the integrated multiplicity result in pp collisions, as shown in Fig. 3.10. The data follows a trend: for hadrons with higher strange content, the production is further enhanced. This feature also supports that the mechanism that enhances the production of those particles is related to the number of strange quarks.

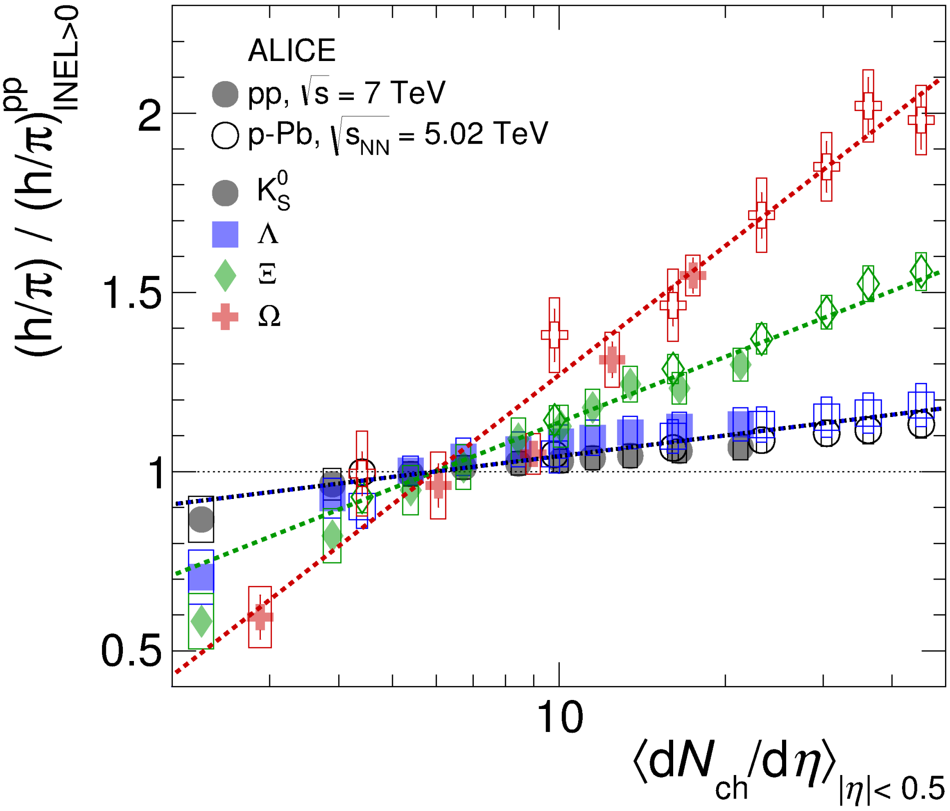

Figure 3.10: Particle yield ratios to pions in pp and p–Pb collisions normalized to the values measured in minimum bias pp collisions. Figure taken from Ref. [82].

3.5 Chapter summary

The observation of double-ridge structures in small systems has caught the interest of the heavy-ion community. The effect resembles the elliptic flow in heavy-ion collisions, connected to the translation of the initial geometry into the anisotropy in the transverse momentum. The second Fourier coefficient v_2 is found to be non-zero using two- and multi-particle azimuthal correlations of light hadrons. The anisotropy also has a similar mass dependence as the one in heavy-ion collisions, which could point to a similar origin. Models evoking a hydrodynamic expansion of a small-medium, inspired in the ones used in heavy-ion collisions, have successfully described the effect and its mass dependence. Transport models, such as BAMPS and AMPT have also reproduced, at least qualitatively, the v_2 in small systems. Models using initial-state effects as a source of anisotropy are qualitatively similar to the experimental data and more progress in this area could help the understanding of the anisotropies. The question on what is the source of those structures is still under debate and more measurements might help in the understanding of this puzzle. The production of strange particles is found to be enhanced in pp and p–Pb collisions, similarly to heavy-ion collisions. The source of this effect is also not understood at the moment. It is important to stress that, as shown in the previous chapter, no considerable suppression on the particle yields or jets have been found so far in small systems.

4 — A Large Ion Collider Experiment at the Large Hadron Collider

Large experiments were built in order to study the phenomena presented in the two previous chapters. The high-energy physics has reached an era that it is not possible to finance and build the accelerators for single research purposes: the size of the experiments has grown a lot - and together with it also the cost to build them. They involve thousands of people working to provide accelerator technology, instrumentation to record the results of the collisions, data storage and analysis frameworks to inspect the physical observables. In that field, all the steps are done in a multicultural and diverse team, that has researchers from all the continents.

The results here discussed were taken with the ALICE experiment, one of the six experiments hosted in the Large Hadron Collider (LHC). The LHC is part of the CERN accelerator complex and it has the highest center-of-mass energy achieved in controlled proton–proton collisions. In this chapter, the experimental setup and data taking procedure are briefly described. The details that concerning the analysis procedure, or how the information from each detector is used, is discussed in the next chapter.

4.1 The Large Hadron Collider (LHC)

The data used in this work was collected with the Large Hadron Collider (LHC). The LHC is the largest and most powerful particle accelerator in operation. It was built from 1998 to 2008 by CERN and it is located in the border of Switzerland and France, around Geneva. There is a complex pre-acceleration system in order to accelerate the particles to TeV scales, as shown in Fig. 4.1. The center-of-mass energy varies for each collision system, as shown in Table 4.1. Most of the LHC data come from proton–proton collisions. Once a year, the LHC changes its beams to provide heavy-ion collisions to the experiments. The LHC is able to collide, besides proton–proton (pp) collisions, proton with lead (p–Pb) and lead with lead (Pb–Pb). Recently

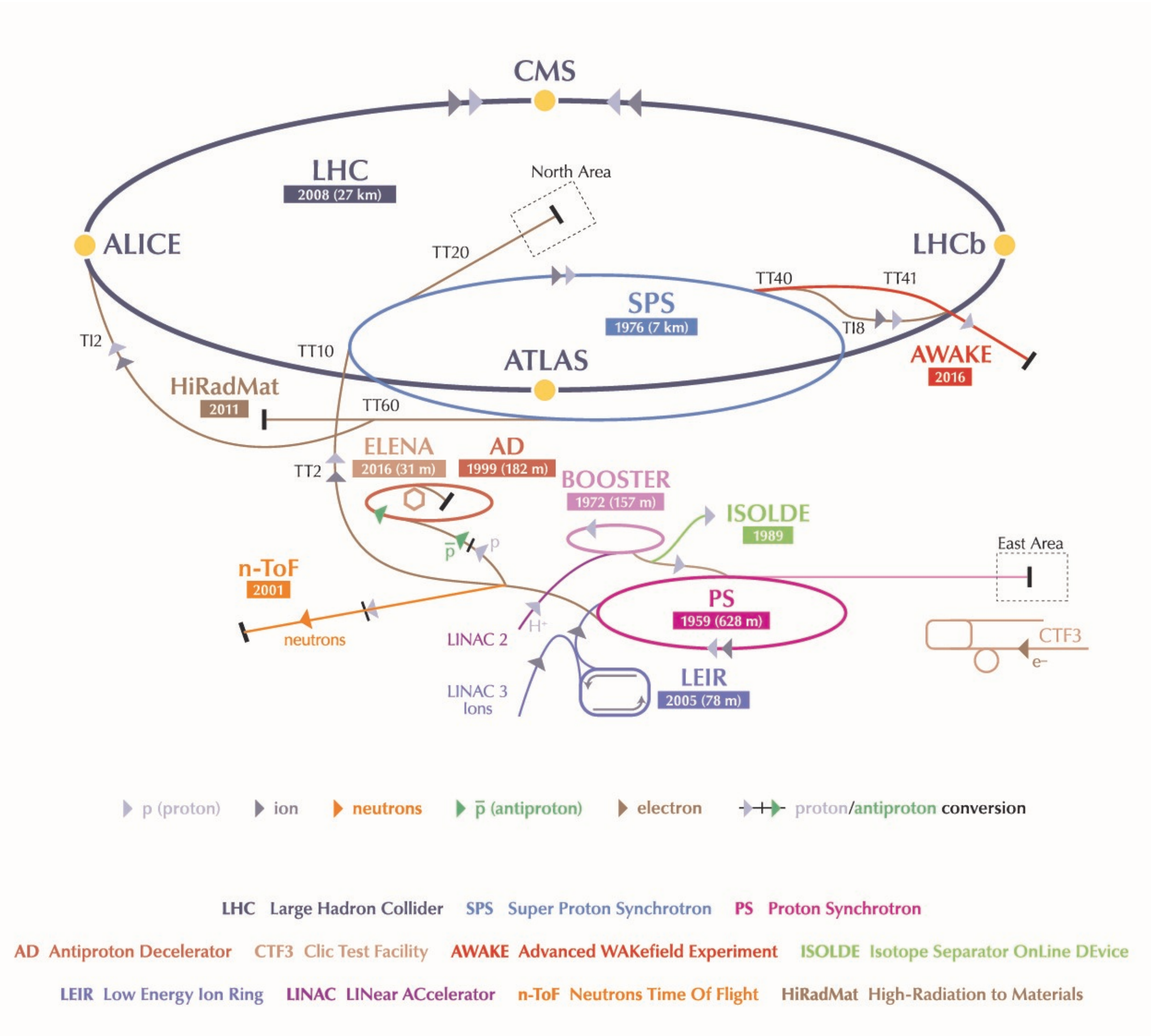

Figure 4.1: Schematic picture of the accelerator complex at CERN. The LHC is the largest ring in dark blue line. The other machines are used in a chain to help boost the particles to their final energies. Figure taken from Ref. [118].

Collision system	Energy (TeV)
pp	0.9, 2.76, 5.02, 7, 8, 13
p–Pb	5.02
Pb–Pb	2.76, 5.02
Xe–Xe	5.44

Table 4.1: Energies ($\sqrt{s_{\mathrm{NN}}}$) available for collisions at the LHC. The Xe–Xe run was very short and not initially planned. All the other collision systems are part of the initial plans for the machine.

it also performed an experimental setup with xenon (Xe) collisions for a short time. It hosts six experiments and each of them have different technical solutions for tracking, particle identification, and event selection. The experiments are:

- ATLAS (A Toroidal LHC Apparatus)
- CMS (Compact Muon Solenoid)
- ALICE (A Large Ion Collider Experiment)
- LHCb (LHC-beauty)
- TOTEM (Total Cross Section, Elastic Scattering and Diffraction Dissociation)
- LHCf (LHC-forward)

CMS and ATLAS are general purpose detectors and are mainly focused on particle physics. They can perform analysis on a variety of topics that include: flavor physics, precision measurements of the standard model, Higgs, search for beyond the standard model physics, heavy-ion collisions and more. The detector design is similar, with a tracking detector close to the beam pipe, followed by an electromagnetic calorimeter, then a hadronic calorimeter and finally a muon detection system. Each experiment works completely independent, in order to provide independent evidence in case of new physics searches. LHCb is focused on performing precision measurements of beauty/charm particles in pp collisions. It covers forward rapidity and it has great particle identification capabilities. TOTEM and LHCf are smaller collaborations that are mostly interested in forward physics.

The data used in this thesis was collected by the ALICE experiment. ALICE is designed to study details of the hot and dense medium formed in Pb–Pb collisions. The LHC provides an increased center of mass energy when compared to the Relativistic Heavy Ion Collider (RICH), in the United States of America. ALICE is optimized to get a full picture of these collisions. Its design includes particle identification up to very low momentum and great tracking capabilities. All parameters are reconstructed in a large phase space by a complex system of detection with different technologies. The next section will describe the detector of ALICE in more detail. Other experiments also join the heavy-ion collision program and are very competitive with ALICE, mainly at high momentum probes, jets, and flow.

4.2 ALICE experimental setup

ALICE is a detector built specifically to study the QGP formed in heavy-ion collisions. The description of the experiment aparatus is presented in Ref. [119]. The choices during its design include great tracking capabilities provided by a gaseous tracking detector and different approaches towards particle identification. All the subsystems, also called detectors, are shown in a schematic illustration in Fig. 4.2.

We can divide the subsystems of ALICE detectors in different classes: tracking detectors (ITS, TPC, TRD), particle identification (TOF, HMPID, TRD), electromagnetic calorimeters (PHOS and EMCal), muon spectrometer, and forward and trigger detectors (T0, V0, ACORDE, FMD, PMD, ZDC). These detectors are briefly described in the next sections. The L3 magnet provides a 0.5 T magnetic field in the central barrel.

4.2.1 Tracking detectors

The tracking detectors aim to recover the trajectory of the particles from the collision using different techniques. The main tracking detectors used in ALICE are the ITS and the TPC. The TRD can be used in a few cases to improve the tracking at high momentum, but it will not be discussed here. The TPC, ITS, and TRD share the acceptance in pseudorapidity of $|\eta| < 0.9$ and a full azimuthal coverage. The ITS and TPC are described bellow.

Inner Tracking System

The ITS (Inner Tracking System) surrounds the beam pipe and it consists of six cylindrical layers of silicon. The ITS provides support for the beam pipe and it cannot move during operation. It aims to determine the interaction point of the collision (primary vertex) and secondary vertexes of decays of heavy flavor and strange particles. It can also perform low momentum particle identification and provide better impact parameter resolution. The ITS is a crucial detector for the operation of ALICE because it contributes to practically all the analysis performed in ALICE.

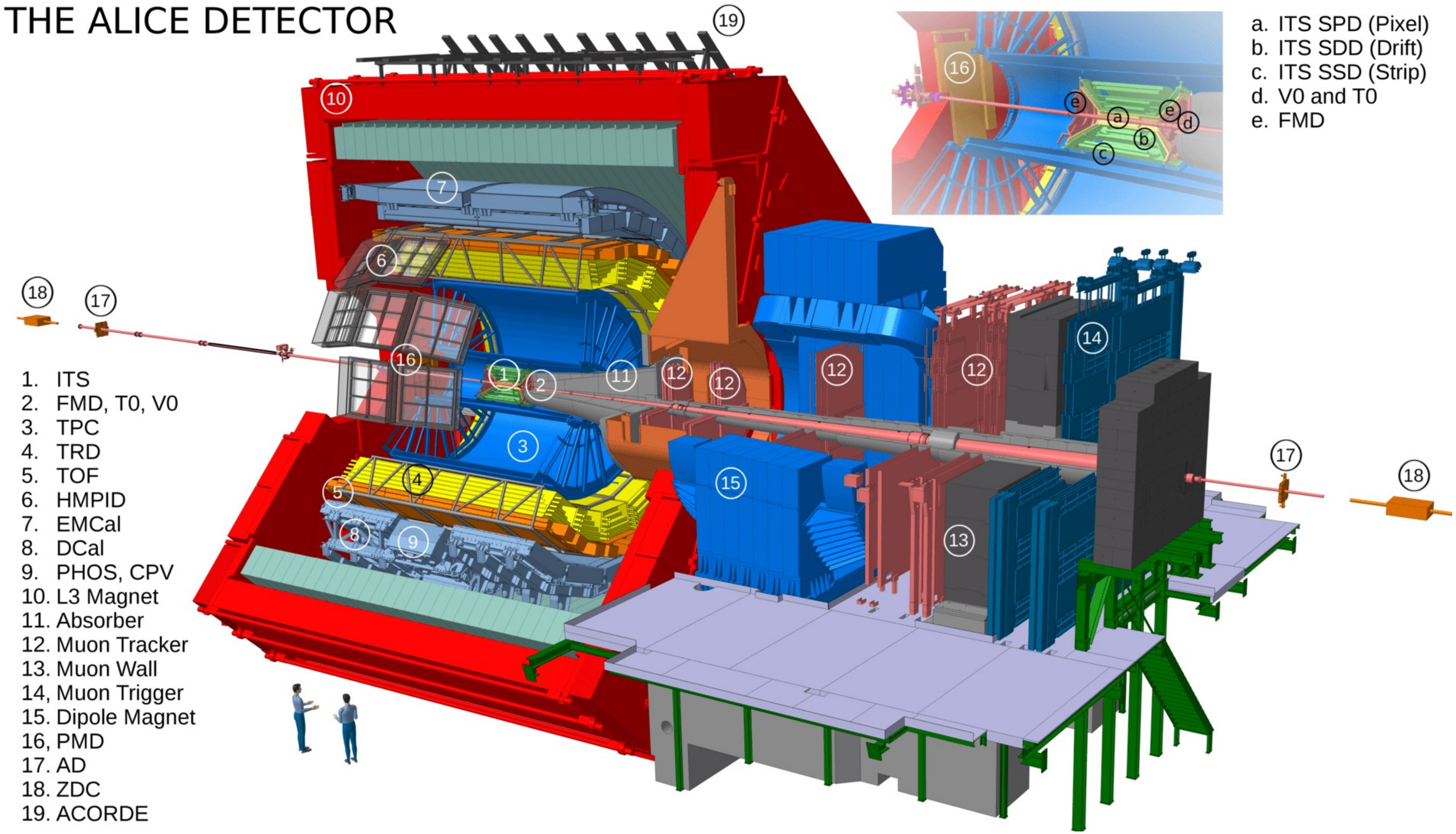

Figure 4.2: Schematic picture of ALICE during the LHC Run 2.

Layer	Type	radius (cm)	z lenght (cm)	Area (m^2)	Channels
1	pixel	3.9	14.1	0.07	3 276 800
2	pixel	7.6	14.1	0.14	6 553 600
3	drift	15.0	22.2	0.42	43 008
4	drift	23.9	29.7	0.89	90 112
5	strip	38.0	43.1	2.20	1 148 928
6	strip	43.0	48.9	2.80	1 459 200

Table 4.2: Main dimensions and parameters of the ITS. Table taken from Ref. [119].

It is composed of 3 sub-detectors, each one with two layers. The number and positions were designed taking into account the precision needed to perform the functions described in the previous paragraph. From the innermost layers to the outermost, the sub-detectors are the Silicon Pixel Detector (SPD), the Silicon Drift Detector (SDD) and the Silicon Strip Detector (SSD). The details of the radius, length in the beam direction, active area and the number of channels on the readout are summarized on Table 4.2.

The total material used in the ITS was kept to a minimum, to improve the momentum and impact parameter resolution for low momentum particles. The granularity was optimized to handle up to 8000 tracks per unit of rapidity in the central barrel. The detector was also designed and tested for its radiation hardness, given the expected radiation during the data taken periods.

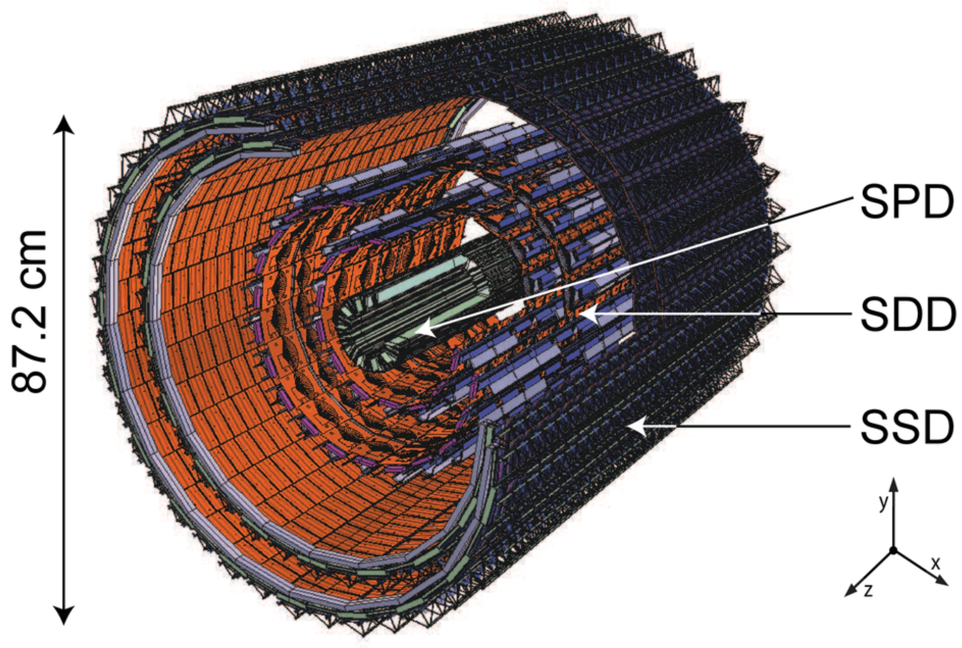

Figure 4.3: Schematic picture of the ITS and its components. Figure taken from Ref. [120].

Time Projection Chamber

The TPC (Time Projection Chamber) is a chamber of 90 m^3 that can reconstruct trajectories of more than 10 000 charged particles at the same time. It is filled by a gas mixture that is ionized by charged particles when they pass through the detector. Due to the electric field present in the TPC, electrons (and ions) from this ionization are collected in the xy plane, and the z component is reconstructed based on the known drift velocity of the particles and time signal measured in the xy plane. The maximum time of drift of those particles is about 88 μs.

The TPC has an inner radius of 85 cm and outer radius of 250 cm. The length along the beam axis is approximately 5 meters. In the middle of the detector, a thin central membrane allows the electric field to be generated, as indicated in Fig 4.4. The design trigger rate limits are about 300 Hz for central Pb–Pb events and 1 kHz for pp events. The detector is segmented in 18 sectors and electrons that are produced in the ionization are collected in multi-wire proportional chambers in the xy plane at the end of the detector. The TPC can reconstruct particles with p_T in the range of 0.1 GeV/c to 100 GeV/c with good momentum resolution. When the particle is travelling in the gas, part of its energy is lost and this can be used for particle identification, as it will be discussed on Chapter 5. The resolution of the specific ionization energy loss (dE/dx) is about 5% for isolated tracks, allowing the separation of different species such as pions, kaons and electrons [121].

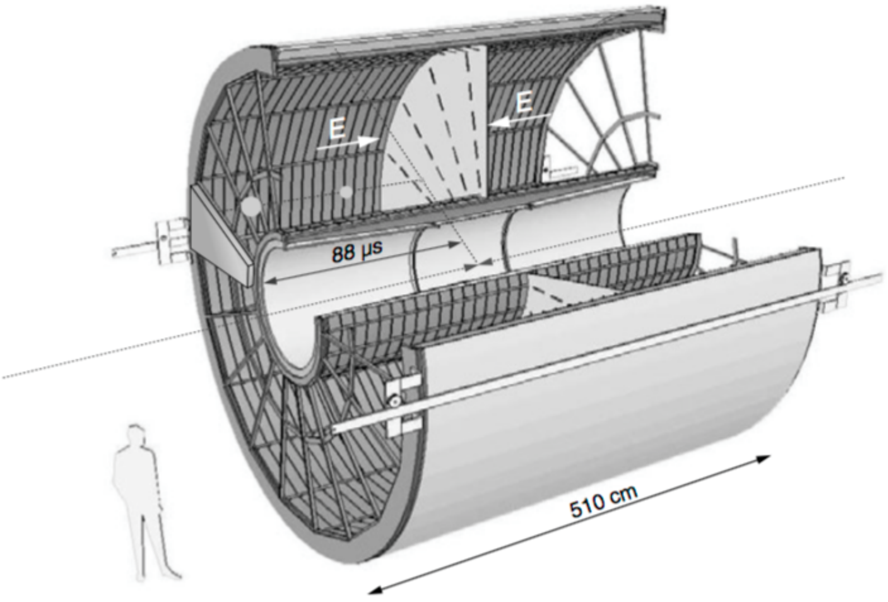

Figure 4.4: Schematic picture of TPC. Figure taken from [122].

4.2.2 Particle Identification

The PID (Particle IDentification) on ALICE relies upon the information of different detectors which are often combined. The detectors that were built exclusively to perform PID are the TOF, HMPID, and TRD. The TPC also provides important information for particle identification, as mentioned previsously. The HMPID (The High Momentum Particle Identification) uses Cherenkov radiation to identify mainly protons and pions. For electrons with $p_T > 1$ GeV/c we can also use TRD information about the specific energy loss in a gas mixture to identify them. The TOF detector was used in the identification of electrons in this work and it is described in more detail bellow.

Time of Flight

The TOF (Time of Flight) detector is a set of multi-gap resistive-plate chambers (MRPC) with full coverage in azimuth. The chamber is composed of a stack of resistive plates filled with gas. It operates with a high and uniform electric field over the full sensitive gaseous volume of the detector. When particles travel in the gas, they ionize it and an avalanche of electrons is started. The avalanche development is stopped by the resistive plates in each gap, but the resistive plates are transparent to the fast signal induced on the pickup electrodes by the movement of the electrons. The induced signal read on the electrodes is then the sum of the signal in all the gaps. The signal can be measured and the time information is very precise. A illustration of this setup is shown Fig. 4.5 . TOF is based in a modular structure, with 18 modules (sectors) in φ and 5 in the beam direction (z). It has an area of 150 m^2 with more than 150 000 readout channels. This detector can measure the time with precision to determine the different times of flights . This information is used together with TPC to improve the PID in the intersection of the TPC dE/dx lines.

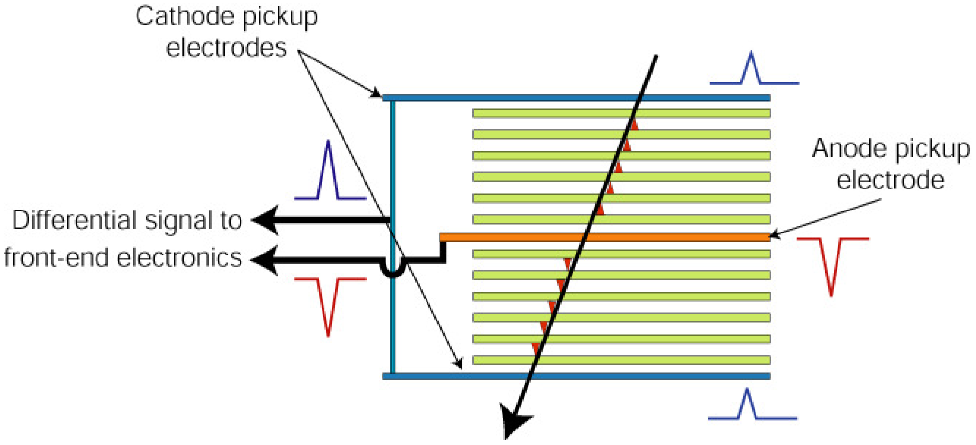

Figure 4.5: Operational principle of the MRPC chambers used in the TOF detector. Figure taken from [123].

4.2.3 Calorimeters

ALICE calorimeters are PHOS (PHOton Spectrometer) and EMCal (ElectroMagnetic CALorimeter) with its extension (DCal). PHOS can identify photons and neutral mesons using very dense scintillators. It has a multiwire chamber to stop charged particles. EMCal is made of Pb and scintillators and can identify electrons and photons using the energy deposited by this particle in the calorimeter. The separation between photons and electrons can be done using tracking information, since photons are neutral particles and do not leave tracks in the TPC. The shape of the shower that is produced in the calorimeter is also used to distiguish between electrons, photons and hadrons. EMCal enhances the capability of ALICE to identify high momentum electrons, since the TPC and TOF cannot identify electrons with high purity at high momentum. There is also a muon spectrometer that is focused on providing information about heavy-quarkonia decays. It has a complex system that can filter other particles from the collisions and it can identify muons with very good efficiency.

4.2.4 Forward and trigger detectors

The forward and trigger detectors are used to measure global variables and to provide different event selections to specific purposes. The V0 detectors are forward detectors made of scintillators that provide trigger and multiplicity information. The ZDCs (Zero Degree Calorimeter) are calorimeters that are more than 100 m distant from the interaction point. The ZDC can detect the remaining nucleon and provide precise information concerning the event centrality/multiplicity. ACORDE (ALICE COsmic Ray DEtector) is used as a trigger for cosmic rays data, which is taken when no beam is present in the accelerator. The Forward Multiplicity Detector (FMD) and PMD (Photon Multiplicity Detector) also provide event multiplicity information.

4.2.5 Triggering

ALICE operated mostly with a minimum bias trigger: the detector usually takes data with the minimum requirements to capture a random collision. Most of the minimum bias triggers require to have a signal in each side of the V0 detector (V0-A and V0-C) and from the SPD. Additional triggers can be used to search for specific signals, such as high momentum particles, di-muon pairs, etc. The hardware level triggers in ALICE are defined as L0, L1, and L2. Different trigger levels are employed due to the arrival times of the trigger inputs and different time requirements of each detector to start the readout process. The L0 trigger receives detectors that can provide information up to 1.2 μs after the collision takes place. The next level, L1, includes detectors with up to 6.5 μs and finally, the last decision step (L2) is taken after the end of the drift time in the TPC (approximately 88 μs). They share the same principle of operation: each detector can provide a logic trigger signal that characterizes a specific detection in this particular system, for example, a high multiplicity collision or a high transverse momentum particle. The signals are sent to the Central Trigger Processor (CTP) where the signals are processed. They are combined using logical operations inside an FPGA (Field Programmable Gate Array) and the event is selected or not based on the available triggers. The CTP can reduce or enhance a particular trigger, depending on the configurations of the run. It also takes care of verifying if all the detectors are ready for data taking and the synchronization with the machine clock. More details about the triggering system can be found in Ref. [124].

4.3 Data reconstruction and analysis

The data is collected from the detector using the Data Acquisition System (DAQ) and saved for offline processing. The raw data is captured in in-site storage units and quickly moved to one of the clusters that are part of the distributed computing system of the LHC. The next step is to convert all those signals into tracks, vertexes, clusters in the calorimeters, etc. This stage is usually designed as the data reconstruction process. The reconstruction is a complicated process and we cover it briefly. For more details, please check Ref. [125] which most of the section is based on.

The reconstruction framework in ALICE is based on ROOT [126] and it is called AliROOT [127]. ROOT is built on top of C++ and it can be used as an external library or as interpreter to scripts developed in C++. Each subsystem provides the framework to calculate centralized calibrations which will result in a unified file that has all the information available for each event. Those files are called Event Data Summary (ESD) files. The ESDs files are considerably large and most of the information is not necessary to the analyzer, so the file is further skimmed into the Analysis Object Data (AOD) files, that contain only information relevant to the particular analysis. The AOD files are shared between different analyses and from that point on each working group has written classes that perform the relevant methods. All the code is available to the public in an open Github repository available in Ref. [128].

4.3.1 Track and vertex reconstruction

The central barrel detectors are used for tracking, as previously mentioned. The whole central barrel is immersed on a 0.5 T field that allows the momentum and charges determination. The main information for tracking comes from the TPC, that can collect up to 159 points from the trajectories. During its propagation in the TPC, charged particles ionize the gas. The electrons produced in the processed are amplified by the 400 V/cm electric field present on the TPC. This field points from the central area towards the borders, parallel to the beam-line direction. These electrons are collected in the xy plane and they are used to determine the position that the ionization happened in the x and y-direction. The position on the z-direction is obtained from the time taken by the signal to arrive in the readouts. This is possible because the particles coming from the collision have higher speeds when compared to the one traveling in the gas. In that way, the start time can be taken as the collision time and the z-direction is calculated using the known drift velocity. The precise measurement of the drift velocity is crucial to the good performance of the reconstruction algorithm. The drift velocity is computed using a laser that ionizes the TPC every hour during the data taking. Since we can keep track of the time that the laser was fired and the distance is known, maps with the drift speed for the different sector of the TPC are calculated with great precision.

After the data collection, the offline reconstruction reconstructs the tracks using Kalman filtering [129]. This technique allows the track finding and track fitting to take place at the same time. The primary vertex (the vertex that corresponds to the point that the collision took place) is also obtained at this stage. The first estimation of the primary vertex is obtained using the point with the highest density of tracklets (lines connecting a pair of clusters in each SPD layer). Then the tracking is performed first from the outer radius to the inner radius. The track seeds are obtained using two TPC clusters that are close in space. Then the next point is found using a proximity cut and the goodness of fit. The procedure is repeated until the track reaches the inner part of the TPC. The tracks are propagated to the ITS until the matched clusters are found. They are propagated to the closest position to the primary vertex and refitted using the already identified clusters. The tracks are further propagated to the detectors located after the TPC, such as TRD, TOF, and EMCal, and matched to clusters on those detectors. The tracks are again propagated to the primary vertex and used to fit a global vertex, with more precise information in comparison to the preliminary that used only the ITS information. The resulting tracks are called global tracks and are most likely coming from primary particles. Particles coming from late decays, such strange mesons, follow a different reconstruction as described in [125].

After the reconstruction of the events, the analysis software will use the information to identify the electrons and perform the measurement here reported. The details of the analysis are described in the next chapter.

4.4 Chapter summary

The Large Hadron Collider (LHC) is the host of multiple particle physics experiments, reaching the highest center of mass energy ever achieved in the laboratory.

Different collision systems, pp, p–Pb and Pb–Pb, are used to study the basic properties of the particle and nuclear physics. One of those experiments is ALICE, a detector specially optimized to record details from heavy-ion collisions and study properties of the QGP. ALICE is made of several detectors that together provide great tracking and particle identification on a large phase space. The main detector is the TPC, a large gas detector that provides excellent tracking in high-density environments. The data is taken mostly using minimum bias triggers and then reconstructed offline using a framework developed on top of ROOT. The data is analyzed in order to extract the physical observable, using different techniques, as it will be discussed in the next chapter.

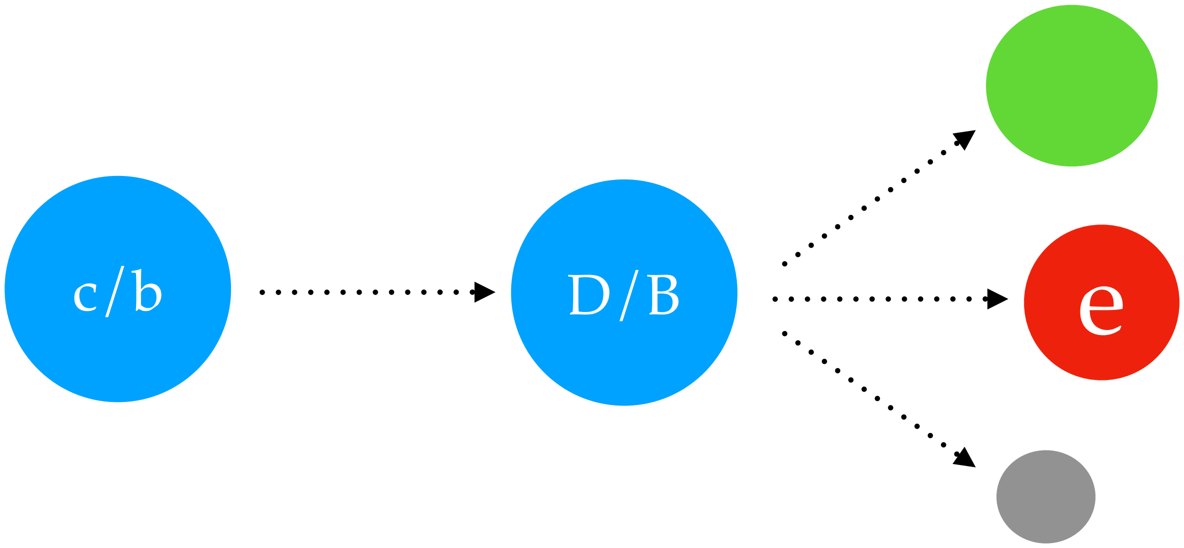

5 — Analysis procedure and methods

This work studies the azimuthal correlation function of heavy-flavor electrons, defined as electrons coming from the decays of particles containing charm or beauty quarks, and charged particles. The semi-leptonic decay channels of D and B mesons involving electrons have roughly a 10% branching ratio [8], which provides more particles when compared to the hadronic decays. However, the comparison with models is not straightforward since the original quark p_T and the decay electron p_T are not directly comparable. That is possible for mesons due to the hard fragmentation of heavy quarks. But the increased number of events is vital for this analysis and that is the reason behind the choice of heavy-flavor electrons over fully reconstructed heavy-flavor mesons or baryons. In the thesis, these electrons are referred to as heavy-flavor hadron decay electrons, heavy-flavor electrons or simply HFe.

The correlation function of heavy-flavor electrons with charged particles (called also hadrons for simplicity), used to study two different data samples from the LHC Run 1 and LHC Run 2, are going to be reported in the next chapters. Since most of the analysis procedure is identical, they are going to be presented only in one chapter. The procedure for the calculation of the final observables, such as the v_2 for the Run 2 analysis, is going to be discussed in each analysis specifically since it is more convenient for the discussion.

The analysis starts by identifying the electrons using TPC and TOF, as described in Sec. 5.1. Then electrons from other sources are subtracted, as described in Sec. 5.2. The calculation of the two-particle correlations needs a few special prescriptions to correctly subtract the contamination from hadrons in the electron sample and to remove the electrons from other sources. These procedures are described in detail on Sec. 5.3.

5.1 Electron identification

Electrons are identified using the specific ionization energy loss in the TPC ($\mathrm{d}E/\mathrm{d}x$) and the time of flight from TOF. When particles are traveling in the TPC, a fraction of their energy is deposited in the interaction with the gas. This energy depends on the particle mass and velocity and it follows the Bethe-Bloch formula. In ALICE, the following form is used [125]:

$$\left\langle \frac{\mathrm{dE}}{\mathrm{dx}} \right\rangle = \frac{P_1}{\beta^{P_4}} \left[P_2 - \beta^{P_4} - \ln\left(P_3 + \frac{1}{(\beta\gamma)^{P_5}} \right) \right], \tag{5.1}$$

where $\beta = v/c$ is the particle velocity normalized by the speed of light, $\gamma = 1/\sqrt{(1-\beta^2)}$ is the Lorentz factor and P_{1-5} are fit parameters that depend on the particle species, charged tracks multiplicity, pseudo-rapidity (η) and transverse momentum (p_T). An example of this fit is shown on Fig. 5.1 where the lines represent the fit of the points. The lines of the TPC $\mathrm{d}E/\mathrm{d}x$ cross each other making the particle identification ambiguous. So additional information from the time of flight measured by the TOF detector is used.

The time of flight is calculated with respect to the start time of the event determined

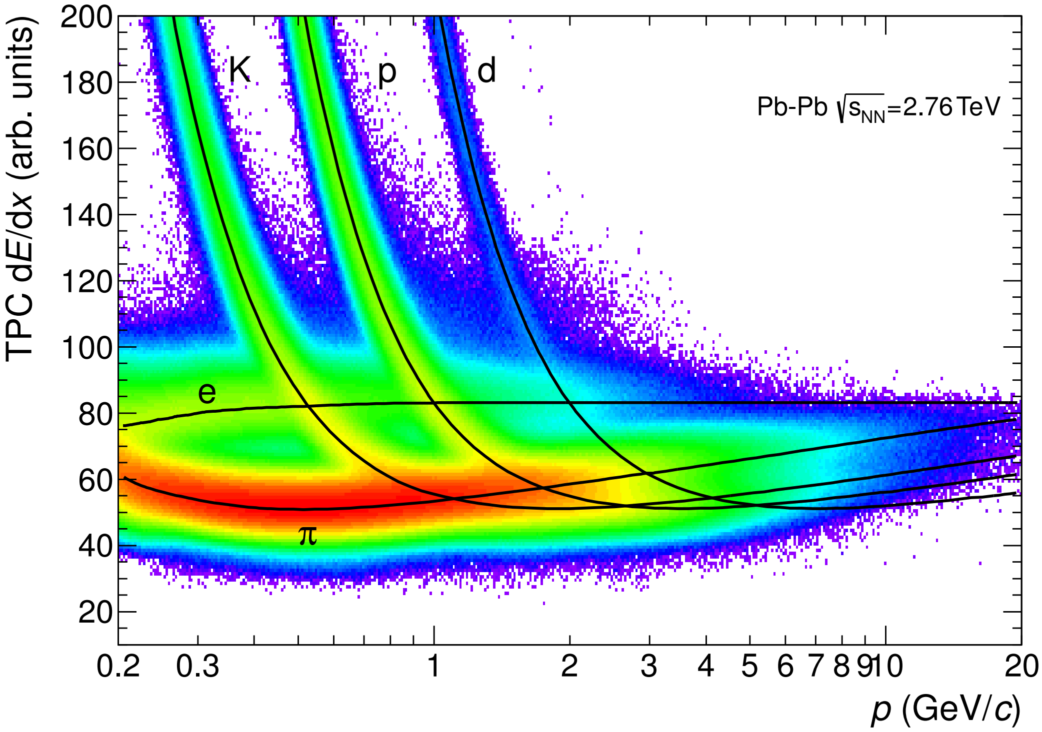

Figure 5.1: Specific ionization energy loss for particles traveling in the TPC gas as function of the momentum in Pb–Pb collisions at $\sqrt{s_{\mathrm{NN}}}$ = 2.76 TeV. The lines represent the fit of the Bethe-Bloch formula for each particle species indicated. Plots for pp and p–Pb collisions are very similar. Figure taken from Ref. [125]

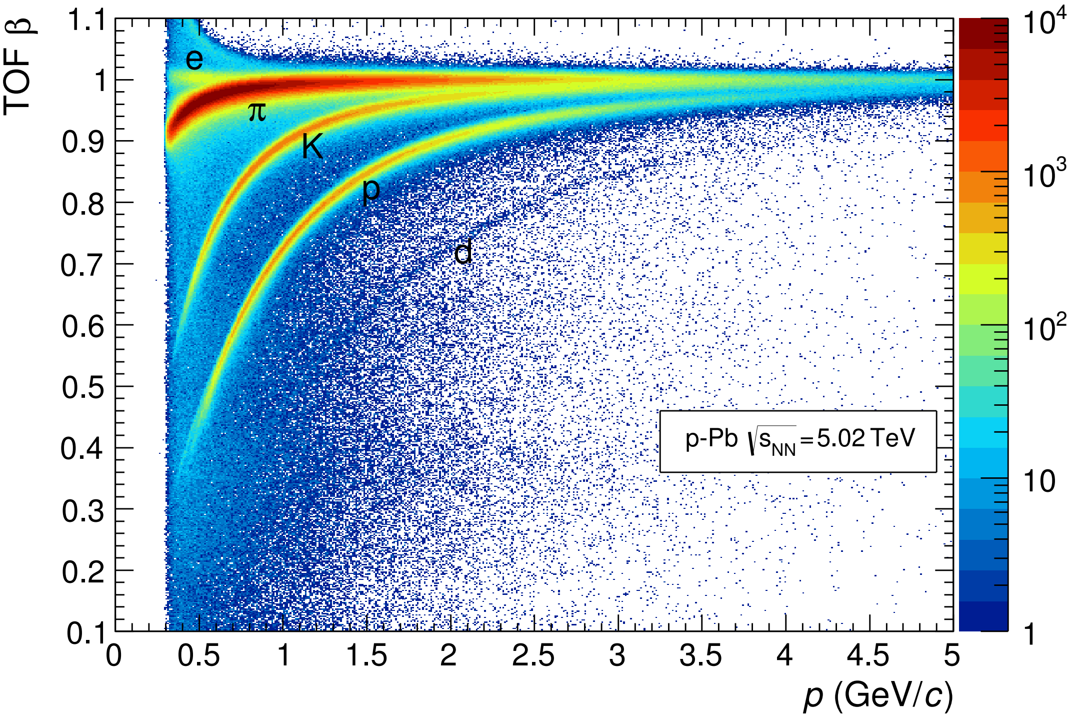

Figure 5.2: β measured in the TOF detector as function of the particle momentum measured by the TPC. The labels indicate the particles species. Figure taken from Ref. [125]

by the T0 detector. This measurement allows us to determine the velocity of the particle and consequently its $\beta = v/c$. Using the expressions $p = \gamma m v$ and $\gamma^2 = \frac{1}{1-\beta^2}$, we can write β as function of the particle mass (m) and momentum (p):

$$\beta(m,p) = \frac{1}{\sqrt{1+\frac{m^2c^2}{p^2}}}, \tag{5.2}$$

resulting in different β values for each particle type at the same momentum. The particle momentum is measured by the TPC and Fig. 5.2 shows the TOF β as function of the momentum. The precise measurement of the time from TOF provides good separation for low momentum particles. At high momentum ($p^2/m^2c^2 \gg 1$) the separation is no longer present and TOF does not provide particle identification anymore.

The ALICE software has an unified particle identification framework that provides selection based on detector responses ($n\sigma$) rather than raw values, such as TPC dE/dx or the TOF β. That means that each detector reports its particle identification estimation ($n\sigma$) based on the deviation of the observed value ($R_{dectector}$) with respect to the expected value for electrons ($< R^e_{dectector} >$) divided by the detector resolution (σ_R):

$$n\sigma^e = \frac{R_{dectector} - < R^e_{dectector} >}{\sigma_R}. \tag{5.3}$$

One example of nσ^{e}_{TPC} distribution as function of the transverse momentum in p–Pb collisions obtained in this analysis is shown on Fig. 5.3. It is possible to see the crossing of the different particles in the electron band (around zero) before using the TOF information. The nσ^{e}_{TPC} has a much more clear electron band when the TOF information ($-3 <$ n$\sigma^{e}_{TOF} < 3$) is used as shown in Fig. 5.4. All the intersections are removed and the sample is dominated by electrons around n$\sigma^{e}_{TPC} \approx 0$.

The selection criteria depends mostly on how much contamination from other particles the analysis can tolerate. For the results of this thesis, a sample with high purity is requested. The tracks are requested to have $-1 <$ n$\sigma^{e}_{TPC} < 3$ and $-3 <$ n$\sigma^{e}_{TOF} < 3$. The asymmetric selection in the TPC is driven by the remaining contamination from pions for n$\sigma^{e}_{TPC} < -1$. The contamination was estimated by fitting the projected distribution with two Gaussians to describe the pions and one gaussian to describe the electrons as shown in Fig. 5.5. At low momentum electron, an additional gaussian is included the contribution from protons at the right side of the figure (high values of nσ^{e}_{TPC}). The remaining contamination is shown on Fig. 5.6. It was found to be below 1% for $1 < p_T < 4$ GeV/c and smaller than 10% for $4 < p_T < 6$ GeV/c and it is statistically subtracted from the total number of electrons.

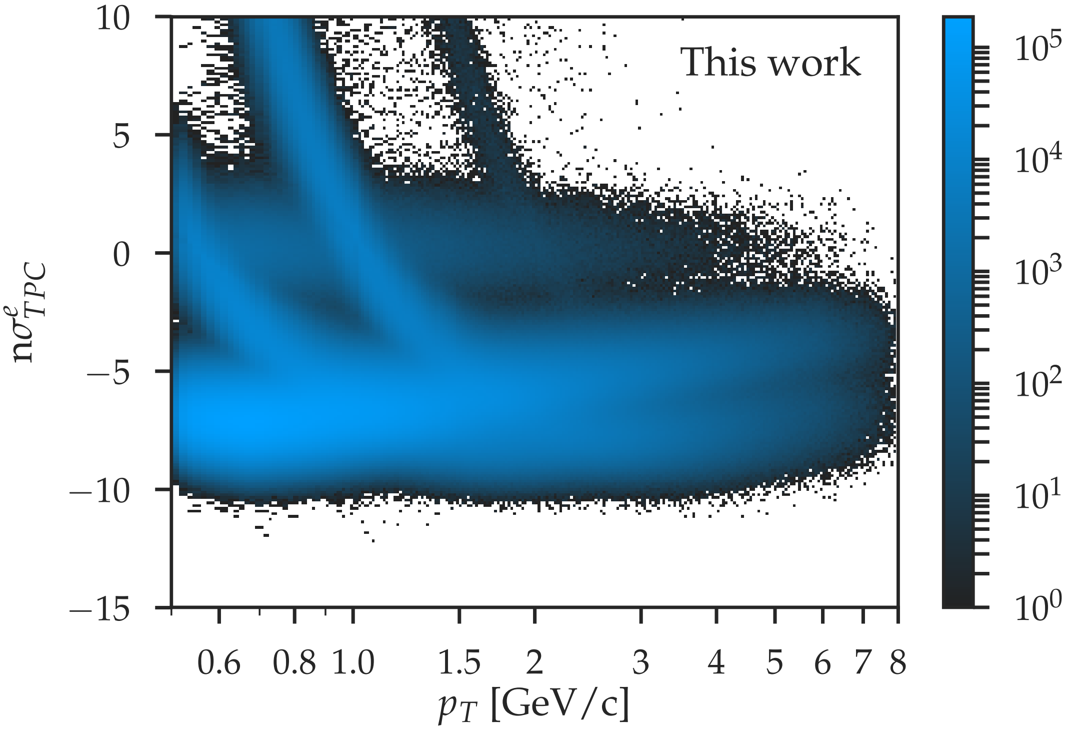

Figure 5.3: Detector response in the TPC for the electron hypothesis ($n\sigma^{e}_{TPC}$) as function of the transverse momentum (p_T) before using the TOF information in p–Pb collisions with $\sqrt{s_{\rm NN}}$ = 5.02 TeV.

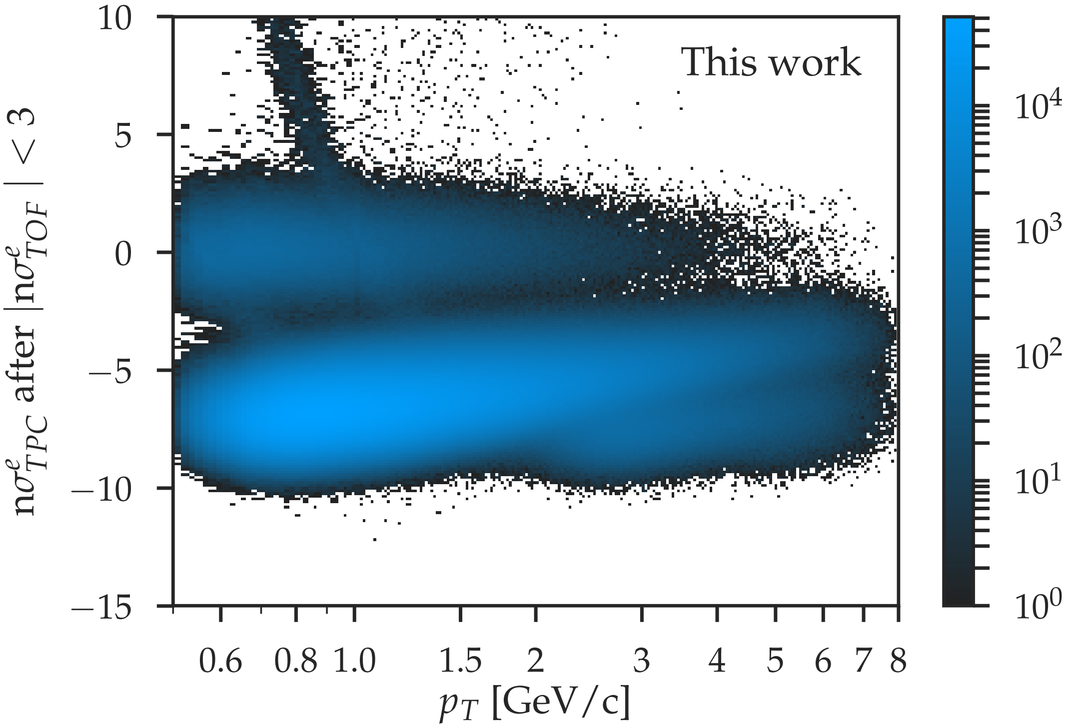

Figure 5.4: Detector response in the TPC for the electron hypothesis ($n\sigma^{e}_{TPC}$) as function of the transverse momentum (p_T) after using the TOF information in p–Pb collisions with $\sqrt{s_{\rm NN}}$ = 5.02 TeV.

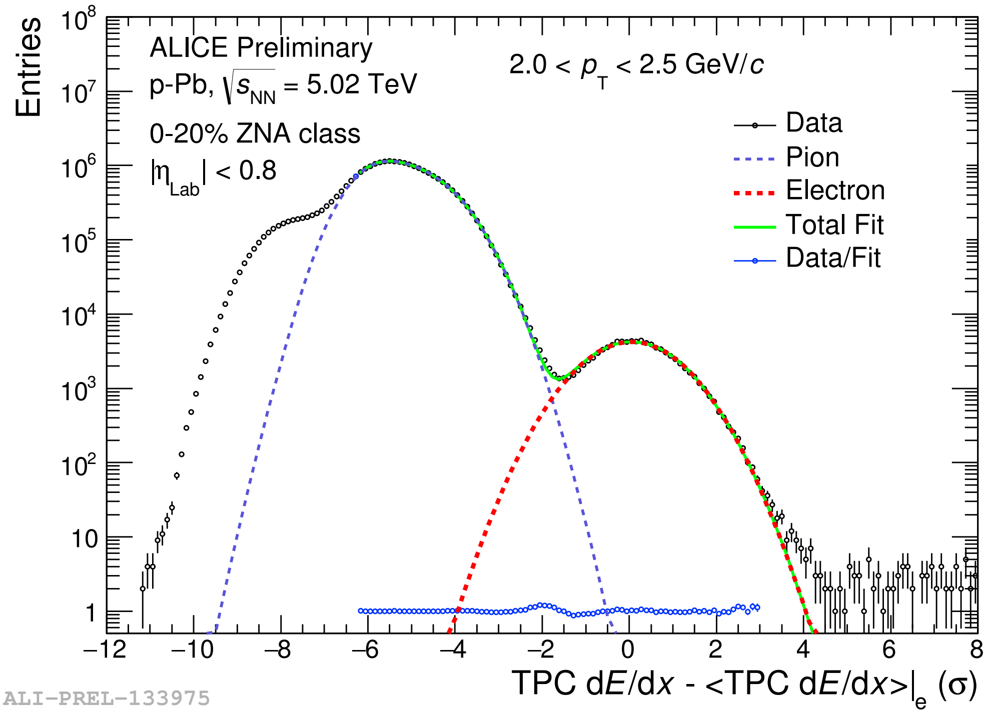

Figure 5.5: Projection of the detector response in the TPC for the electron hypothesis ($n\sigma^{e}_{TPC}$) for $2 < p_T < 2.5$ GeV/c after using the TOF information in p–Pb collisions with $\sqrt{s_{\mathrm{NN}}}$ = 5.02 TeV.

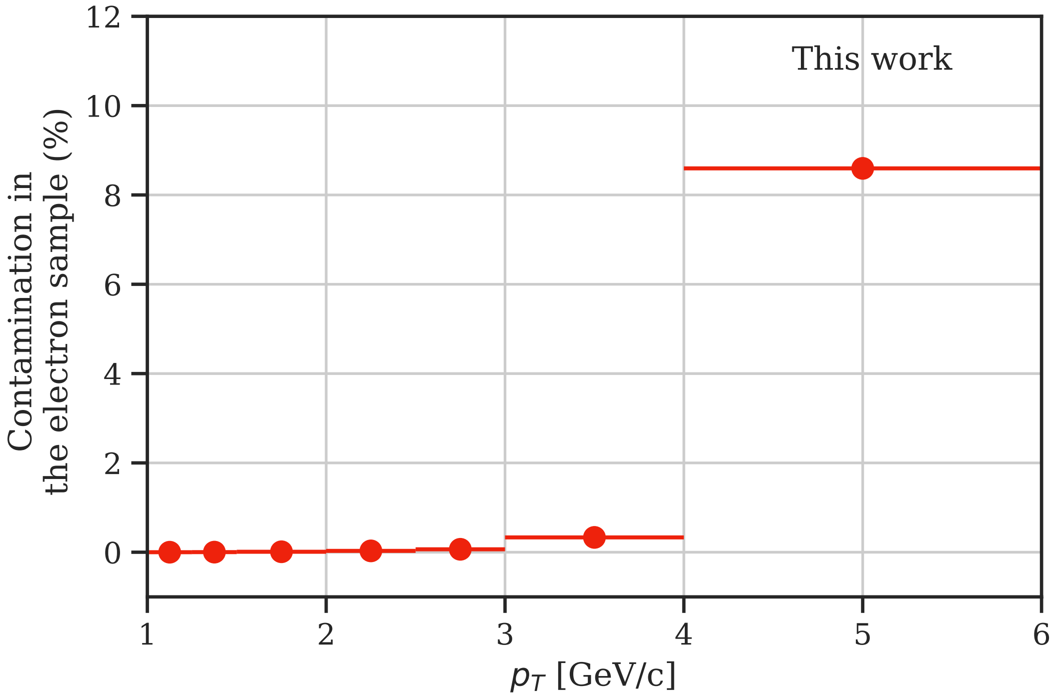

Figure 5.6: Contamination of other particles in the electron sample after using the TPC and TOF selection as function of the transverse momentum in p–Pb collisions with $\sqrt{s_{\mathrm{NN}}}$ = 5.02 TeV. The results do not depend on the multiplicity.

5.2 Subtraction of electrons from other sources

After separating electrons from other particles it is necessary to identify the source that they come from. We are only interested in electrons from decays of mesons and baryons containing c and b. There are significant contributions from other particle decays at low and high momentum. For high momentum electrons ($p_T > 20$ GeV/c) the contribution of vector-boson decays, such as Z and W, is relevant and is usually subtracted using simulations reweighed to data. In the low momentum region, photon conversions in the detector material ($\gamma \to e^+e^-$) and Dalitz decays of neutral mesons ($\pi^0 \to \gamma e^+e^-$ and $\eta^0 \to \gamma e^+e^-$) are the dominant contribution. They can be removed by studying the invariant mass of electron-positron pairs in a technique called photonic electron tagging method. Since the measurement is restricted to $p_T < 6$ GeV/c, only the photonic electron tagging method, which will be described in detail in the next paragraphs, is used to subtract the background electrons. Electrons from J/ψ, Υ, kaons and other Dalitz decays of light mesons that are also present were in this kinetic range were estimated using a simulation weigthed to data in previous an analysis (shown on Figure 5.7) and they have a negligible yield, so no corrections were applied.

The photonic electron tagging method can identify an electron-positron pair that

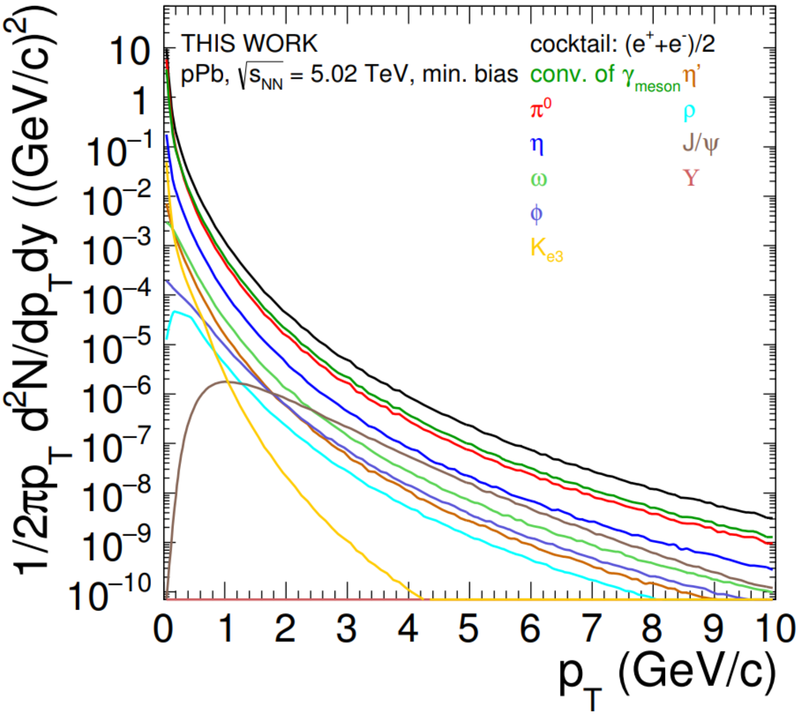

Figure 5.7: Electron production in p–Pb collisions using the cocktail method. The contributions from light mesons are based in the transverse mass scaling of the π^0 spectrum and the conversions take into account the ALICE geometry. Calculation and figure from Ref. [130].

comes from the same decay in case both electrons have left tracks in the detector (left side of Fig. 5.8). Each selected electron from the analysis is combined with other opposite electrons from the same event (partners). The unlike-sign pair has its invariant mass calculated and it is considered to be a background electron if $m(e^+,e^-) < 140$ MeV/c^2. The combinatorial contribution to the unlike-sign distribution is evaluated by combining electrons that have the same charge and calculating their invariant mass. An example of this distribution is shown in Fig. 5.9, where we can observe the peaked distribution at low $m(e^+,e^-)$ due to the photonic background. Both unlike-sign and like-sign distributions are very similar for $m(e^+,e^-) > 140$ MeV/c because no more significant correlation is found. This is due to the fact that heavy-flavor electrons have are part of semi-leptonic decays and do not have another electron in the decays. Partners fulfill looser particle identification requirements ($-3 < \mathrm{n}\sigma^{e}_{TPC} < 3$ and no TOF requirement) and are not requested points in the ITS. This is done to improve the chance of identifying the pair. The number of identified background electrons (N_{NonHFe}) is obtained by subtracting the number of electron in unlike-sign pairs (N_{ULSe}) from the number of like-sign pairs (N_{LSe}):

$$N^{\mathrm{ID}}_{\mathrm{NonHFe}} = N_{\mathrm{ULSe}} - N_{\mathrm{LSe}}. \tag{5.4}$$

On the other hand, if one of the electrons has not been reconstructed the decay cannot be identified (right side of Fig. 5.8). This can happen if the electron is out of the acceptance or if it cannot be reconstructed due to the tracking requirements (p_T, number of points in the TPC, etc). Since these electrons do not have a partner, there

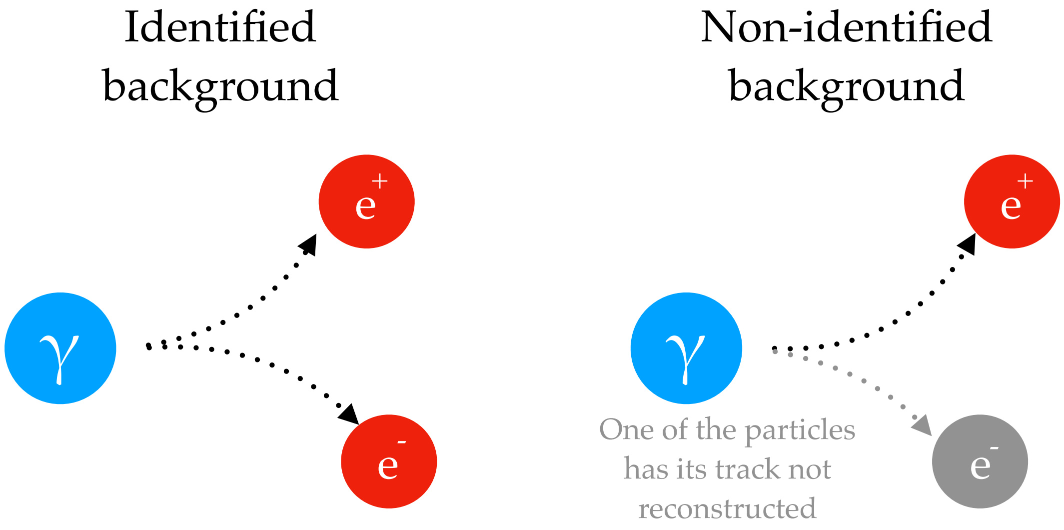

Figure 5.8: The photonic electron tagging method can identify electrons coming from γ, π^0 and η if both electrons from the decay are reconstructed in the tracks (left side). In case one of the tracks is not present in the sample, the electron cannot be identified as background (right side).

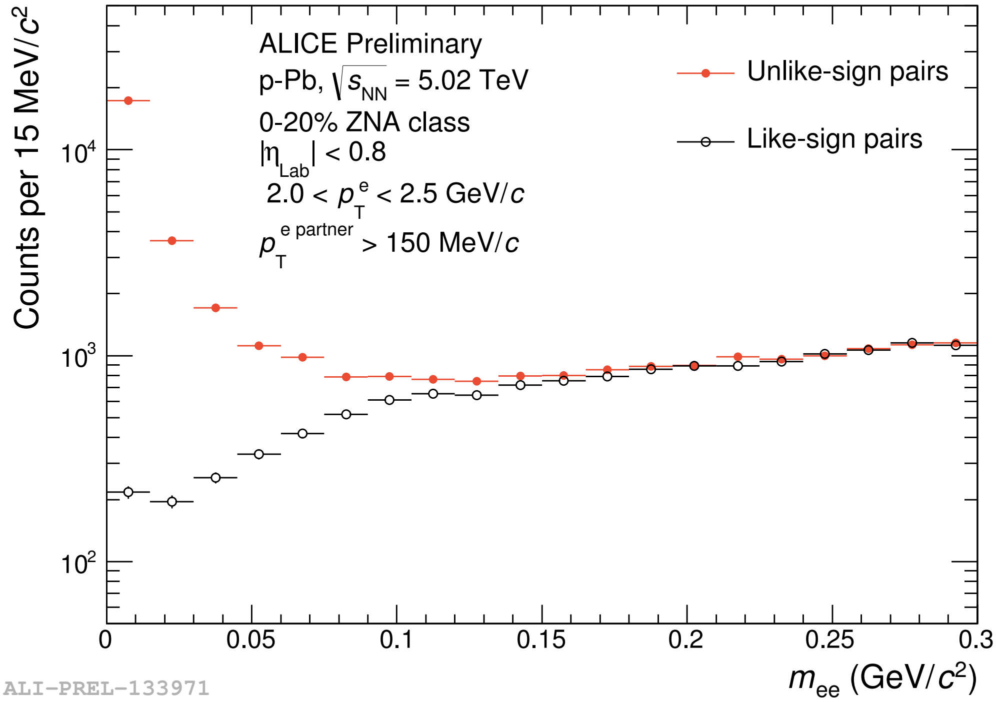

Figure 5.9: Invariant mass distribution for unlike-sign and like-sign pairs used for the background tagging.

is no data-driven way of identifying them. The solution is to remove them statistically by calculating the probability of reconstructing the electron partner (ϵ_{tag}, tagging efficiency).

Detector response simulations of p–Pb collisions were done using HIJING [131] to generate events and GEANT3 [132] to propagate them through the detector. So it is possible to access information from the kinematic level (HIJING) and the tracks and other quantities measured by the detector. The simulation is run-by-run calibrated to match the detector conditions in each of the ALICE subsystems. At the kinematic level, the spectra of π^0 and η in the sample are weighted to match the measured data since they are not correctly reproduced by HIJING. This is necessary since the momentum of the daughter electrons is sensitive to the mother particle p_T distribution. Then the photonic electron tagging method is applied in the same way it would be applied in data and compared to the information from the simulation. The tagging efficiency is calculated as

$$\epsilon_{tag} = \frac{N^{reco}_{\mathrm{ULSe}} - N^{reco}_{\mathrm{LSe}}}{N^{true}_{NonHF}}, \tag{5.5}$$

where N^{reco}_{ULSe} and N^{reco}_{LSe} are the number of unlike-sign and like-sign electrons found in the tracks and N^{true}_{NonHF} is the number of background electrons identified using the information from the simulation. The calculated values are shown in Fig. 5.10. The total number of non-heavy-flavor electrons can be obtained by simply dividing $N^{\mathrm{ID}}_{\mathrm{NonHFe}}$ by

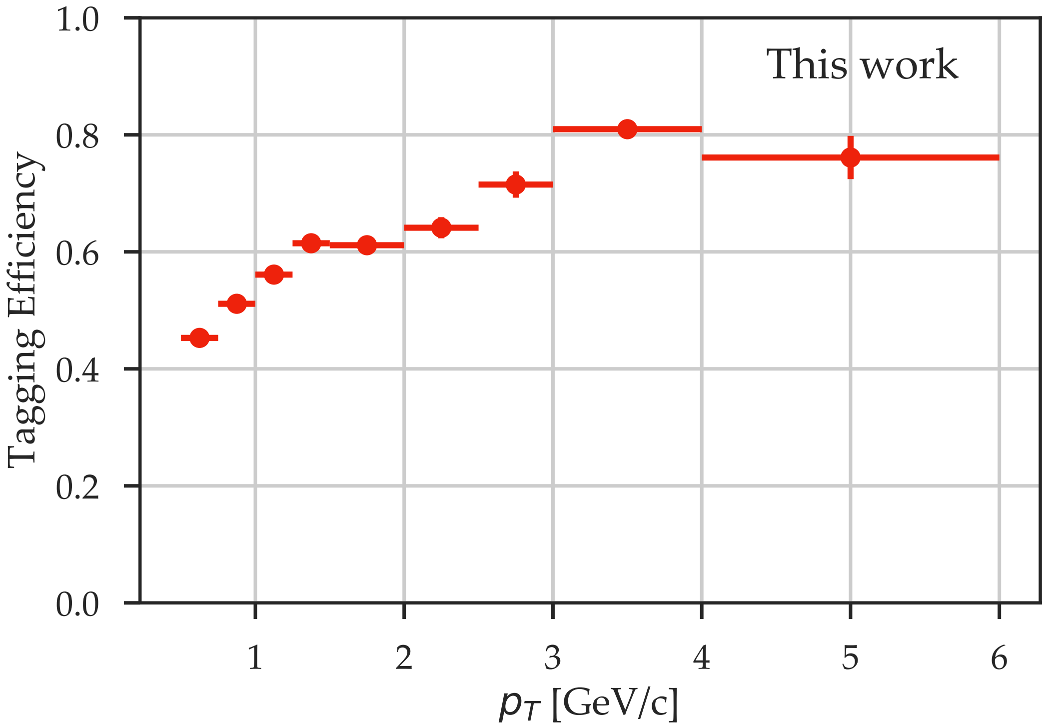

Figure 5.10: Probability of reconstructing the electron partner (tagging efficiency) as function of the transverse momentum (p_T) using the photonic electron tagging method in p–Pb collisions.

the tagging efficiency as in

$$N_{\mathrm{NonHFe}} = \frac{N^{\mathrm{ID}}_{\mathrm{NonHFe}}}{\epsilon_{tag}}. \tag{5.6}$$

And finally, it is possible to obtain the number of heavy-flavor electrons as

$$N_{\mathrm{HFe}} = N_e - N_{\mathrm{NonHFe}} = N_e - \frac{N_{\mathrm{ULSe}} - N_{\mathrm{LSe}}}{\epsilon_{tag}}. \tag{5.7}$$

This equation is used when obtaining the spectra, but it will be more convenient when handling correlation distributions to write N_{NonHFe} as function of the identified and non-identified background. This separation is achieved by summing $N^{\mathrm{ID}}_{\mathrm{NonHFe}} - N^{\mathrm{ID}}_{\mathrm{NonHFe}}$ in Eq. 5.6 and grouping one of the terms:

$$N_{\mathrm{NonHFe}} = N^{\mathrm{ID}}_{\mathrm{NonHFe}} + \left(\frac{1}{\epsilon_{tag}} - 1\right) N^{\mathrm{ID}}_{\mathrm{NonHFe}}, \tag{5.8}$$

allowing the identification of the second term as the non-identified background contribution ($N^{\mathrm{noID}}_{\mathrm{NonHFe}}$):

$$N^{\mathrm{NoID}}_{\mathrm{NonHFe}} = \left(\frac{1}{\epsilon_{tag}} - 1\right) N^{\mathrm{ID}}_{\mathrm{NonHFe}}. \tag{5.9}$$

We can rewrite the number of heavy-flavor electrons, by substituting Eq. 5.9 into Eq. 5.7 , as

$$N_{\mathrm{HFe}} = N_e - \left[N^{\mathrm{ID}}_{\mathrm{NonHFe}} + \left(\frac{1}{\epsilon_{tag}} - 1 \right) N^{\mathrm{ID}}_{\mathrm{NonHFe}} \right]. \tag{5.10}$$

5.3 Two-particle correlation distributions

The correlation analysis takes place after identifying the electrons and its source. Two-particle correlation distributions are obtained by calculating the differences in the azimuthal angle and pseudo-rapidity between trigger particles (electrons in this work) and associated particles (unidentified charged particles, also called hadrons for simplicity). This differences are denoted as $\Delta\varphi = \varphi_{hadron} - \varphi_{trigger}$ for the azimuth and $\Delta\eta = \eta_{hadron} - \eta_{trigger}$ for the pseudo-rapidity. It is computed as

$$C(\Delta\varphi, \Delta\eta) = \frac{s(\Delta\varphi, \Delta\eta)}{b(\Delta\varphi, \Delta\eta)}, \tag{5.11}$$

where $s(\Delta\varphi, \Delta\eta)$ is the same event distribution and $b(\Delta\varphi, \Delta\eta)$ is the mixed event distribution. An example of each of those distributions is shown in Fig 5.11. The $s(\Delta\varphi, \Delta\eta)$ is defined as

$$s(\Delta\varphi, \Delta\eta) = \frac{1}{N_{trigger}} \frac{d^2 N^{same}_{e-h}(\Delta\varphi, \Delta\eta)}{d\Delta\varphi d\Delta\eta}, \tag{5.12}$$

and it is obtained by calculating $\Delta\varphi$ and $\Delta\eta$ between trigger particles and hadrons from the same event ($N^{same}_{e-h}(\Delta\varphi, \Delta\eta)$). It is normalized by the total number of trigger particles $N_{triggers}$ at the end of the data processing, not on a event-by-event basis. Moreover, $b(\Delta\varphi, \Delta\eta)$ is calculated by combing trigger electrons with hadrons from different events. The motivation behind mixing events is to cancel effects coming from the limited acceptance. For example it is much more likely to find a pair with $\Delta\eta \approx 0.1$ than one with $\Delta\eta \approx 1$ due to the fact that the TPC can reconstruct tracks only within $|\eta| < 0.9$. Inhomogeneities in the detector that affect the two-particle acceptance are also corrected by this technique. It is normalized by an *ad hoc* factor in order to be one when the particles are traveling in approximately the same direction ($b(0,0) = 1$). So its definition is

$$b(\Delta\varphi, \Delta\eta) = \frac{1}{b(0,0)} \frac{d^2 N^{mixed}_{e-h}(\Delta\varphi, \Delta\eta)}{d\Delta\varphi d\Delta\eta}. \tag{5.13}$$

The same and mixed event distributions are corrected by single particle efficiencies and contamination from secondary charged particles by weighting the correlation distribution. The correction factor of the hadrons is the inverse of the tracking efficiency times the relative contamination ($1/w_h$) taking into account the detector acceptance,

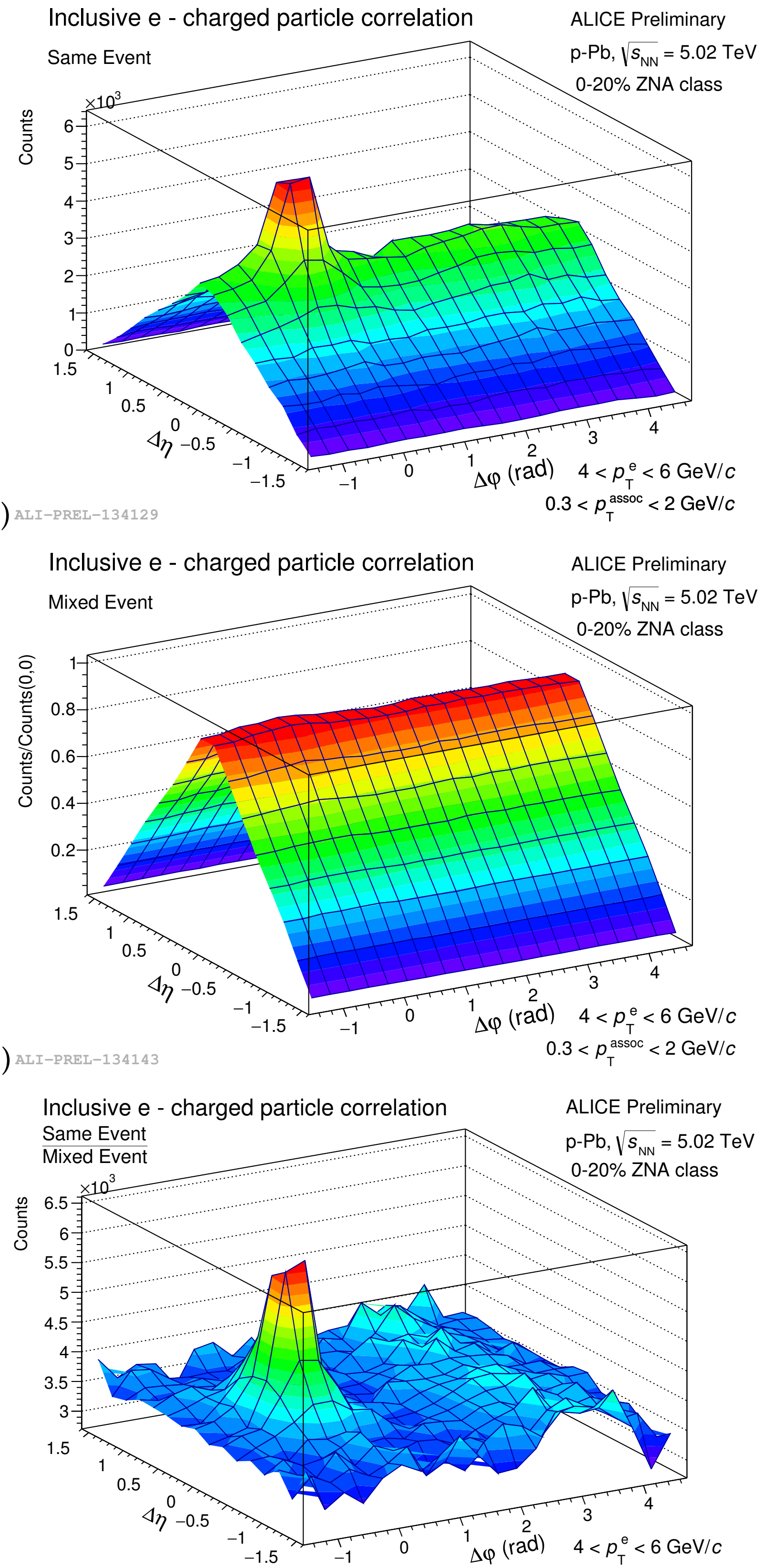

(a) ALI-PREL-134129

(b) ALI-PREL-134143

(c) ALI-PREL-134147

Figure 5.11: Correlation distribution for electron in the same event (a), from mixed events (b) and the corrected distribution (c). See text for details.

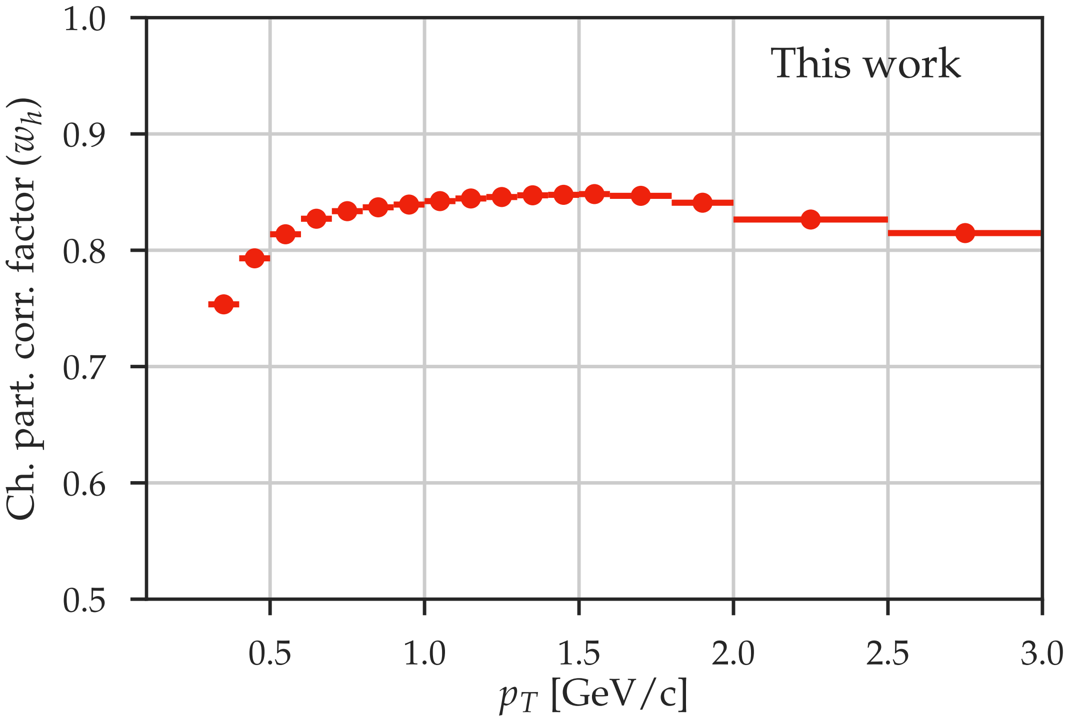

Figure 5.12: Correction factor (w_h, efficiency times contamination) for unidentified charged particles as function of transverse momentum in p–Pb collisions at $\sqrt{s_{\mathrm{NN}}}$ = 5.02 TeV.

the reconstruction efficiency of the tracking algorithm, detector conditions that depend on the data taking period and any remaining secondary particles. The inverse of the weight is calculated using the ratio

$$w_h = \frac{MC\ \textbf{reconstructed}\ \text{tracks}}{MC\ \text{physics primary}\ \textbf{generated}\ \text{tracks}}, \tag{5.14}$$

where the numerator represents the number of reconstructed tracks that fulfill the analysis requirements the denominator is the information obtained from the information of at the generation level of the simulation. An example of w_h as function of p_T is shown on Fig. 5.12.

On the other hand, w_e is calculated as

$$w_e = \frac{MC\ \textbf{reconstructed}\ \text{HFe}}{MC\ \textbf{generated}\ HFe}, \tag{5.15}$$

in the numerator, we have the number of heavy-flavor electrons that fulfills all the requirements of the analysis. The source of these electrons is identified using the MC information with no correction from secondaries. The photonic electron tagging method is not taken into account in the evaluation of this correction factor since is essentially a way of removing secondary electrons and its efficiency, stability and corrections are

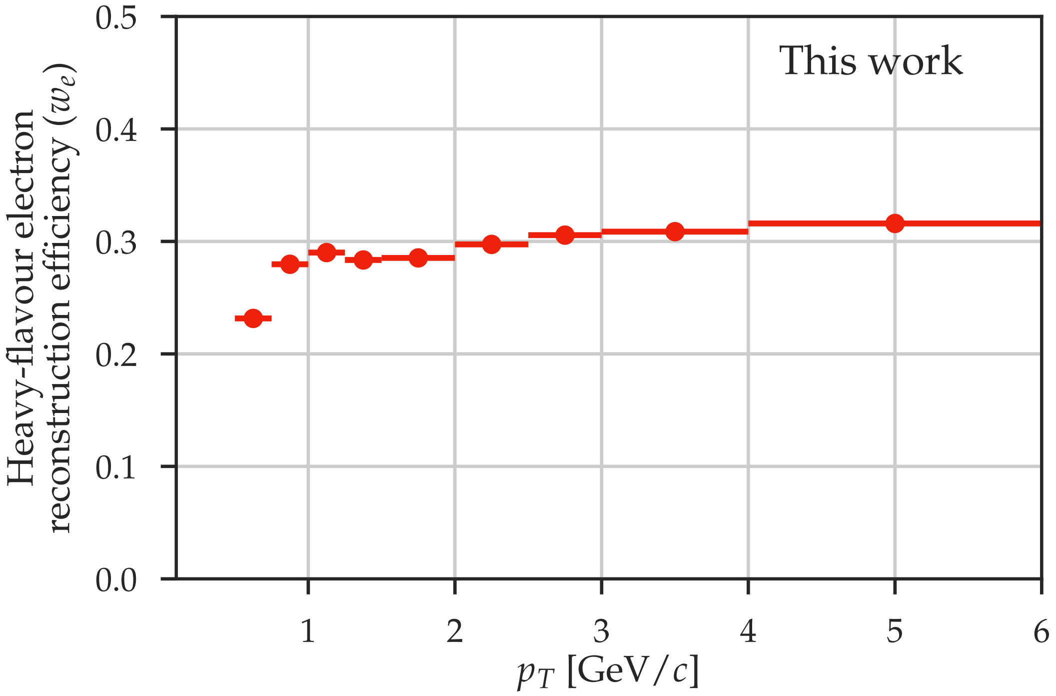

Figure 5.13: Reconstruction efficiency of heavy-flavor electrons as function of the transverse momentum in p–Pb collisions at $\sqrt{s_{\rm NN}}$ = 5.02 TeV.

studied in detail during the analysis. So, w_e is the total heavy-flavor electron efficiency (reconstruction and PID) and does not correct from secondary particles. This correction (Figure 5.13) is applied as function of p_T.

In the next sections, non normalized two-particle correlation distributions are also used. They are the same-event non normalized electron-hadron distribution:

$$S(\Delta\varphi, \Delta\eta) = \frac{d^2N^{same}_{e-h}(\Delta\varphi, \Delta\eta)}{d\Delta\varphi d\Delta\eta}, \tag{5.16}$$

similarly the non normalized mixed-event electron-hadron distributions:

$$B(\Delta\varphi, \Delta\eta) = \frac{d^2N^{mixed}_{e-h}(\Delta\varphi, \Delta\eta)}{d\Delta\varphi d\Delta\eta}, \tag{5.17}$$

and also the non-normalized correlation distribution:

$$H(\Delta\varphi, \Delta\eta) = S(\Delta\varphi, \Delta\eta)/b(\Delta\varphi, \Delta\eta). \tag{5.18}$$

Note that in the expression of H, only the same event distribution is not normalized, so we have $h(\Delta\varphi, \Delta\eta) = H(\Delta\varphi, \Delta\eta)/N_{triggers}$. Now that most of the terminology of the two-particle correlation has been defined, we will explain details of the procedures: the subtraction of the hadron contamination, the subtraction of the non-heavy-flavor electrons in the correlation distributions and the estimation of the Fourier coefficients

(v_n).

5.3.1 Subtraction of the contamination in the selected electrons

The hadron contamination in the electron sample is small due to the selections discussed on Sec. 5.1. But nevertheless, it is necessary to subtract it at correlation level. When calculating the number of heavy-flavor electrons, it is only necessary to subtract the total number of hadrons ($N_{hadrons}$) in the sample obtained by fitting the detector response distributions from the total number of electrons before the removal of the contamination (N_{raw}), obtaining the total number of electrons (N_e):

$$N_e = N_{raw} - N_{hadrons}, \tag{5.19}$$

where $N_{hadrons}$ is the number of hadrons in the electron sample:

$$N_{hadrons} = \alpha \cdot N_{raw}, \tag{5.20}$$

calculated using α, the hadron contamination estimated on Section 5.1.

In the correlation distributions, it is necessary to build charged particle - charged particle correlations (hadron-hadron) distributions in the events that have electrons. Then, to obtain the non-normalized electron-hadron correlation distribution (S_e), we need to subtract the contamination coming from non-electron triggers

$$S_e(\Delta\varphi, \Delta\eta) = S_{raw}(\Delta\varphi, \Delta\eta) - N_{hadrons} \cdot s_{h-h}(\Delta\varphi, \Delta\eta), \tag{5.21}$$

where S_{raw} is the non-normalized electron same event distribution before the hadron contamination is subtracted and s_{h-h} is the hadron-hadron same event correlation distribution which has been obtained using $\sigma^e_{TPC} < -3.5$. This selection is done to get a sample dominated by pions that are the largest source of contamination. The mixed event distributions have been obtained without subtracting any hadronic contribution. It is a reasonable assumption, since the contamination α is small. Also the main correction provided by the mixing is the acceptance one which should not have a strong dependence in the particle species.

5.3.2 Removal of non-heavy-flavor electrons

After the hadron contamination subtraction, we need to remove electrons from other sources ($\gamma \to e^+e^-$, $\pi^0 \to \gamma e^+e^-$ and others as discussed on Sec. 5.2) to obtain the heavy-flavor electron-hadron correlation distribution (H_{HFe}):

$$H_{HFe}(\Delta\varphi, \Delta\eta) = S_{HFe}(\Delta\varphi, \Delta\eta)/b_{HFe}(\Delta\varphi, \Delta\eta). \tag{5.22}$$

where S_{HFe} and b_{HFe} are the same and mixed event heavy-flavor electron-hadron distributions, respectively. So we subtract the non-heavy-flavor (S_{NonHFe}) component from the correlation distributions in the same event distributions:

$$S_{HFe}(\Delta\varphi, \Delta\eta) = S_e(\Delta\varphi, \Delta\eta) - S_{NonHFe}(\Delta\varphi, \Delta\eta, \tag{5.23}$$

And similarly to the mixed event distributions:

$$B_{HFe}(\Delta\varphi, \Delta\eta) = B_e(\Delta\varphi, \Delta\eta) - B_{NonHFe}(\Delta\varphi, \Delta\eta). \tag{5.24}$$

where B_{NHFe} refers to the (non-normalized) non-heavy-flavor electrons mixed event distribution and from which we can obtain b_{HFe}:

$$b_{HFe}(\Delta\varphi, \Delta\eta) = \frac{B_{HFe}(\Delta\varphi, \Delta\eta)}{B_{HFe}(0,0)} = \frac{B_{inc}(\Delta\varphi, \Delta\eta) - B_{NHFe}(\Delta\varphi, \Delta\eta)}{B_{inc}(0,0) - B_{NHFe}(0,0)}. \tag{5.25}$$

The non-heavy-flavor electron background S_{NHFe} can be split into two terms (the same is valid for B_{NHFe}):

$$S_{NHFe}(\Delta\varphi, \Delta\eta) = S^{id}_{NHFe}(\Delta\varphi, \Delta\eta) + S^{\neq id}_{NHFe}(\Delta\varphi, \Delta\eta), \tag{5.26}$$

where:

- S^{id}_{NHFe} refers to the identified background, when both electrons (from the pair) are reconstructed and identified via their invariant mass ($m_{e^+e^-} < 140$ MeV$/c^2$). Also, to take into account the uncorrelated pairs, the corresponding like-sign electron pair distribution that should be statistically identical to this combinatoric background, is subtracted: $S^{id}_{NHFe} = S_{ULS} - S_{LS}$ where S_{ULS} and S_{LS} are the electron-hadron distributions of electron that have been paired, respectively, with an unlike and like-sign electron.

- $S^{\neq id}_{NHFe}$ corresponds to the non identified background, when only one electron from the pair is reconstructed (the second one can be of too low momentum or out of the acceptance).

To evaluate $S^{\neq id}_{NHFe}$ we use the hypothesis that the electron-hadron distribution does not depends on the fact that the second electron of the pair (called partner) is reconstructed. Therefore, to mimic its shape we use S^{id*}_{NHFe} which is the same distribution as S^{id}_{NHFe}, but low invariant mass partners are removed from the hadron pool: $S^{id*}_{NHFe} = S^*_{ULS} - S^*_{LS}$. The total non-identified background electrons distribution is then obtained as following:

$$S^{\neq id}_{NHFe}(\Delta\varphi, \Delta\eta) = (\frac{1}{\epsilon_{tag}} - 1) \times S^{id^*}_{NHFe}(\Delta\varphi, \Delta\eta), \tag{5.27}$$

where ϵ_{tag} is the efficiency (probability) of a electron pair to be reconstructed with the method used, i.e. we calculated it from simulations as following:

$$\epsilon_{tag} = \frac{N^{id}_{NHFe}}{N^{gene}_{NHFe}} = \frac{N^{reco}_{ULS} - N^{reco}_{LS}}{N^{gene}_{NHFe}}. \tag{5.28}$$

The values of these efficiencies ϵ_{tag} are presented Figure 5.14, no multiplicity dependence was found.

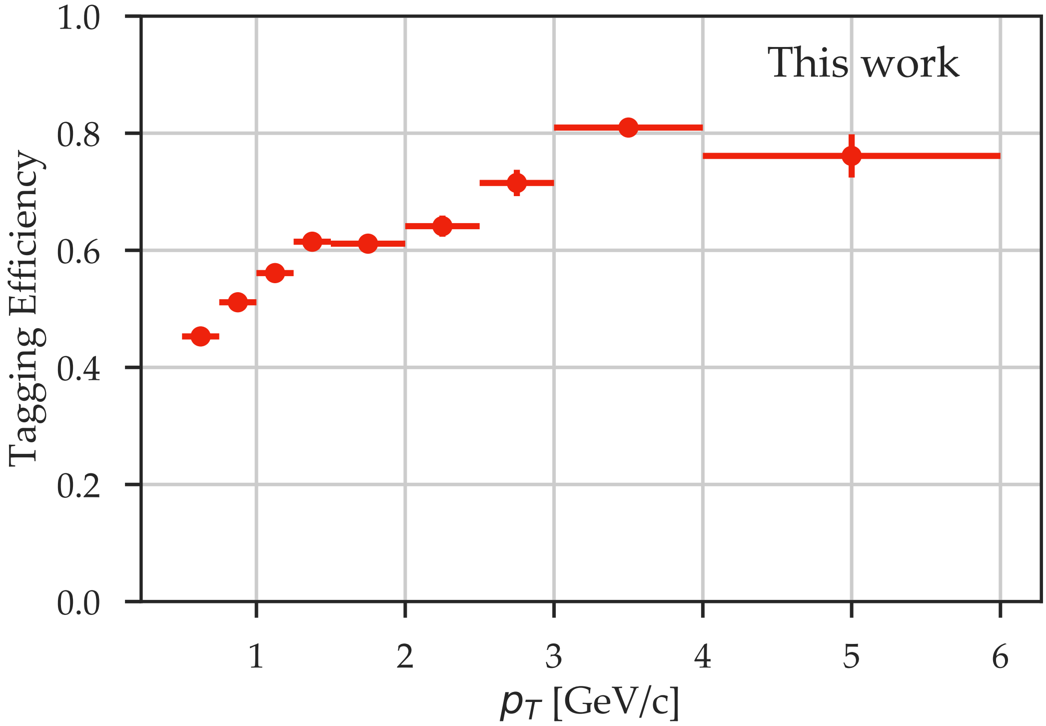

Figure 5.14: Efficiencies of identifying non-heavy-flavor electrons via invariant mass tagging ($m_{e^+,e^-} < 140$ MeV/c^2). No multiplicity dependence was found (not shown).

To demonstrate the relation 5.27 we use normalized distributions. Since we assume that the distribution should not change whether the partner electron is found or not we can write:

$$s^{\neq id}_{NHFe} = s^{id^*}_{NHFe}, \tag{5.29}$$

and we have then:

$$S^{\neq id}_{NHFe} = N^{\neq id}_{NHFe} \times s^{id^*}_{NHFe}. \tag{5.30}$$

Now, using Eq. 5.28 and $N^{\neq id}_{NHFe} = N^{gene}_{NHFe} - N^{id}_{NHFe}$ we have:

$$\epsilon = \frac{N^{id}_{NHFe}}{N^{id}_{NHFe} + N^{\neq id}_{NHFe}} \tag{5.31}$$

Putting this relation in Eq. 5.30, we obtain:

$$S^{\neq id}_{NHFe}(\Delta\varphi, \Delta\eta) = (\frac{1}{\epsilon} - 1) \times N^{id}_{NHFe} \times s^{id^*}_{NHFe}(\Delta\varphi, \Delta\eta) \tag{5.32}$$

Going back to the non-normalized correlation distributions we can identify Eq. 5.27.

Finally, after all the corrections mentioned this chapter, we can obtain the corrected heavy-flavor electron–charged particles correlation function, by dividing Eq. 5.22 by the number of heavy-flavor electrons (Eq. 5.10):

$$h_{HFe}(\Delta\varphi, \Delta\eta) = \frac{H_{HFe}(\Delta\varphi, \Delta\eta)}{N_{HFe}} \tag{5.33}$$

5.4 Chapter summary

The procedure used to obtain the heavy-flavor electron - charged particle correlation was discussed in this chapter. Details on each step of the procedure were given. The identification of the electrons employs information from the TPC and TOF, that is suitable to separate them from hadrons with good precision at low momentum. The electrons coming from other sources, mainly conversion of photons in the beam pipe and in the first layers of the ITS or Dalitz decays of neutral mesons, are subtracted using a data-driven approach. Di-electron pairs are combined and an invariant mass analysis is performed. The correlation function is calculated by calculating azimuthal and pseudorapidity differences between electrons and charged particles. Each electron is combined with charged particles from other events, to remove detector and acceptance effects. The correlation function also used the invariant mass analysis to identify the different sources and combine them properly, which allow us to obtain the heavy-flavor electron - charged particle correlations.

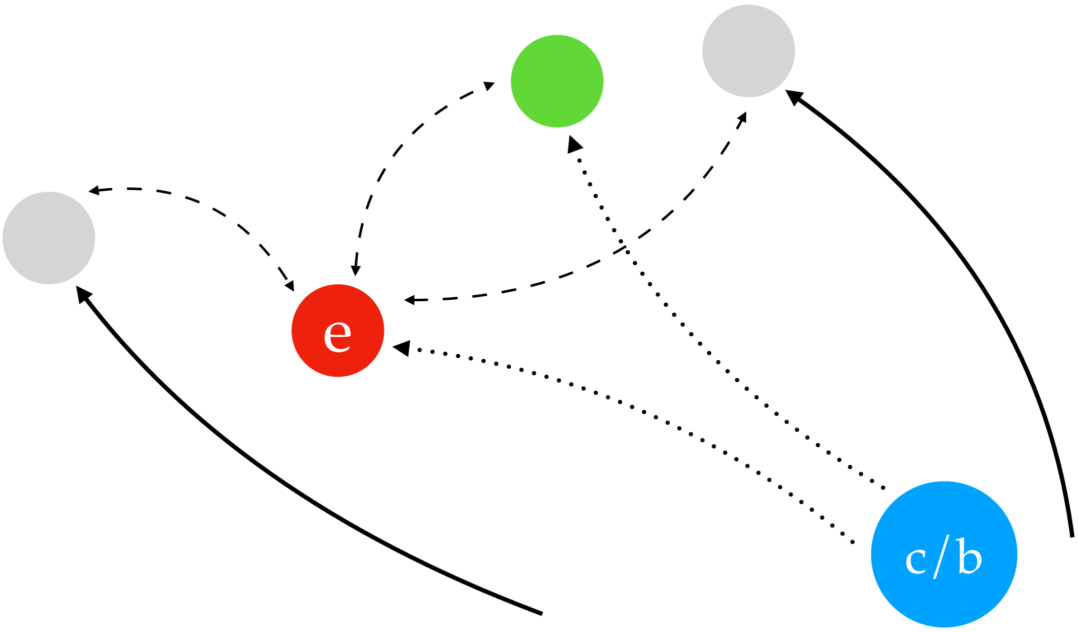

6 — Two-particle correlation of heavy-flavor electrons with charged particles in p-Pb collisions

As discussed in Chapters 2 and 3, the study of two-particle angular correlation functions in small systems has found unexpected results, such as the long-range v_2-like double-ridge structure. Further study of the ridge is necessary to shed light on the origin of such effects. One possible strategy is to look at the mass dependence of the v_2 extracted in such collisions. The analysis reported in this thesis are contributing to the field by studying the ridge structure in particles from heavy-flavor quark decays.

The analysis of the correlation function between heavy-flavor electrons and charged particles in p–Pb collisions was evaluated using the methods discussed in Chapter 5. The data sample analyzed consisted of approximately 100 million p–Pb events, selected with a minimum bias trigger. The analysis was fully validated in this stage, including tests in simulations and data. The results of the correlation functions are reported in this chapter. The available number of events was not enough to access the heavy-flavor electron v_2 in this data set. The analysis was redone with data from the LHC Run 2, as it will be discussed on Chapter 7.

6.1 Data sample

The data sample analyzed was collected in 2013 during the LHC p–Pb run at $\sqrt{s_{\rm NN}} = 5.02$ TeV. This was part of the LHC Run 1 program and the first p–Pb beams of the LHC. Due to the magnet configuration, the center-of-mass energy of the protons and lead ions were different.T he center-of-mass reference frame of the nucleon–nucleon collision was shifted in rapidity by 0.465 units in the proton-going direction with respect to the laboratory frame.

A minimum-bias trigger was employed during the data taking, requiring coincident signals in the V0-A and V0-C arrays. Pile-up was rejected offline using information from the V0s and ZDCs timing. Events were only analyzed if their primary vertex was within ±10 cm from the center of the detector along the beam axis. The total number of events analyzed using this selection was about 10^8, corresponding to an integrated luminosity of $48.6 \pm 1.6\ \mu b^{-1}$.

6.2 Multiplicity selection

The multiplicity estimation uses the Glauber model [22] to calculate geometrical quantities of p–Pb. This model uses the impact parameter b to control the average number of participating nucleons and the number of collisions, and it allows the calculation of the probability distributions for each one of those quantities. Since it is not possible to measure this quantities directly, they have to be related to another measured observable usually called centrality/multiplicity estimators. This connection is then verified experimentally in each collision system and energy by comparing the measured and expected probability densities for a given centrality/multiplicity estimator. The details of the procedure used to obtain the multiplicity estimation are given in Ref. [133]. An example of the Glauber fit of the V0A estimator, used as a multiplicity estimator in this analysis, is given on Fig. 6.1. The events analyzed were divided into two multiplicity classes using the amplitude of the signal in the V0-A detector: high (0–20%) and low multiplicity (60–100%) classes. Other multiplicity classes or estimators were not considered.

6.3 Azimuthal correlation distributions

The two-particle correlation distributions were obtained following the procedure from Chap. 5. The two-dimensional analysis was not possible due to the large statistical uncertainties. So, the angular and pseudrapidity correlation distributions were projected onto $\Delta\varphi$ for $|\Delta\eta| < 1.6$. The correlation distributions were obtained for the electron transverse momentum intervals of $1.5 < p_T^e < 2$ GeV/c, $2 < p_T^e < 4$ GeV/c

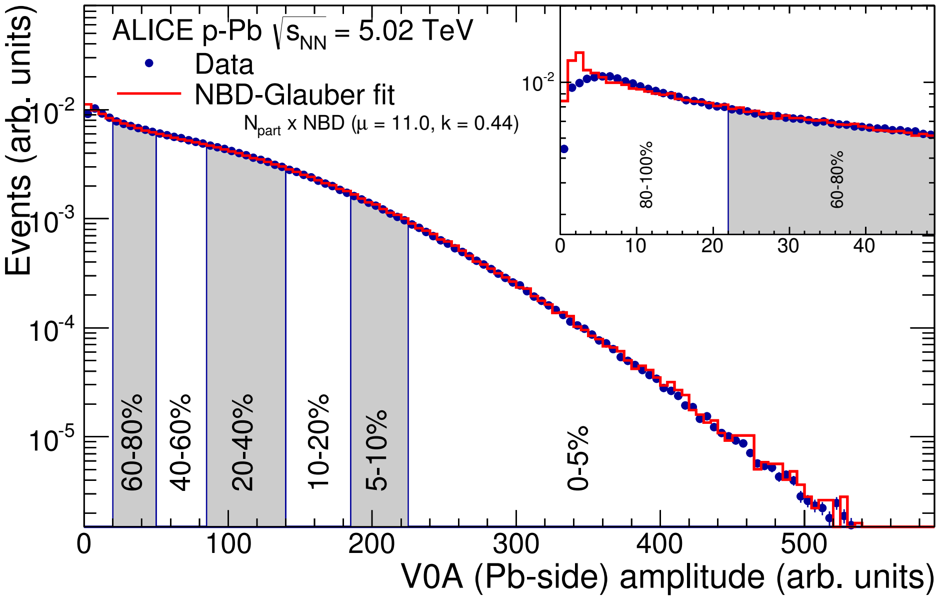

Figure 6.1: Sum of amplitudes in the V0A detector (Pb-going) and its Glauber fit. Centrality classes are indicated by vertical lines. The most peripheral events are zoomed on the top of the plot. Figure taken from Ref. [133].

and $4 < p_T^e < 6$ GeV/c. The electrons with $p_T^e < 1.5$ GeV/c were not considered due to the low signal/background ratio present in that region, which considerably increases the systematic uncertainties. The momentum range for charged particles studied was set to $0.3 < p_T^h < 2$ GeV/c. The correlation distributions in the two considered multiplicity classes (0–20% and 60–100%) are shown in Fig. 6.2-6.4. The study of the systematical uncertainties was also performed to access the bias in the analysis procedure and it is described in the next section.

The differences in the correlation at low- and high-multiplicity collisions are not found in the interval studied. If there are modifications from low- to high-multiplicity collisions, they are not seen with the statistical and systematical uncertainties available. Quantifications of such modifications, such as the subtraction of the two-particle correlation distributions or the integral in the near/away side have less than 1.5 sigma significance when considering all the uncertainties, and they are not presented.

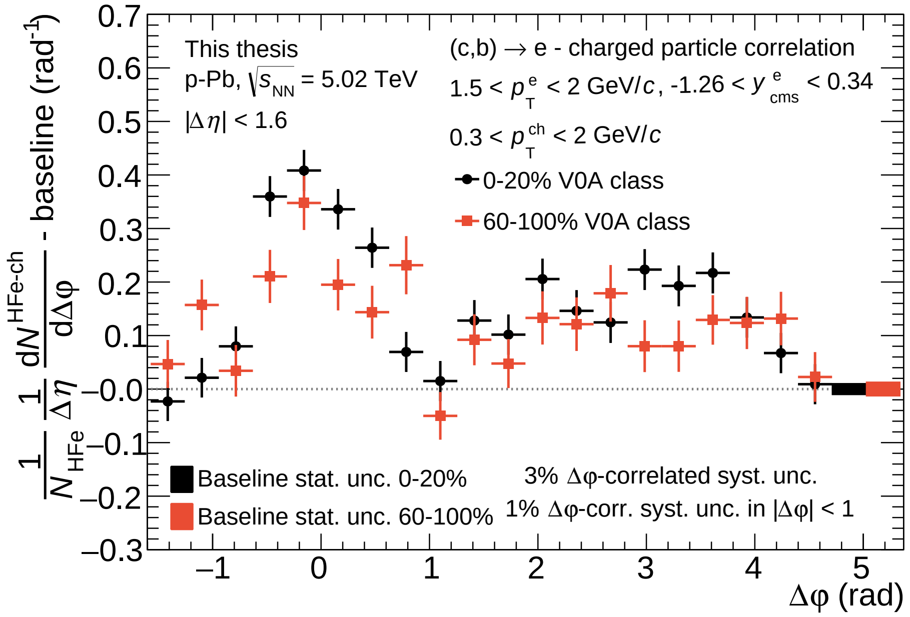

Figure 6.2: Azimuthal correlations between heavy-flavour decay electrons and charged particles, for high-multiplicity (red circles) and low-multiplicity (magenta triangle) p–Pb collisions, after subtracting the baseline. The distributions shown are for $1.5 < p_T^e < 2$ GeV/c and $0.3 < p_T^{ch} < 2$ GeV/c.

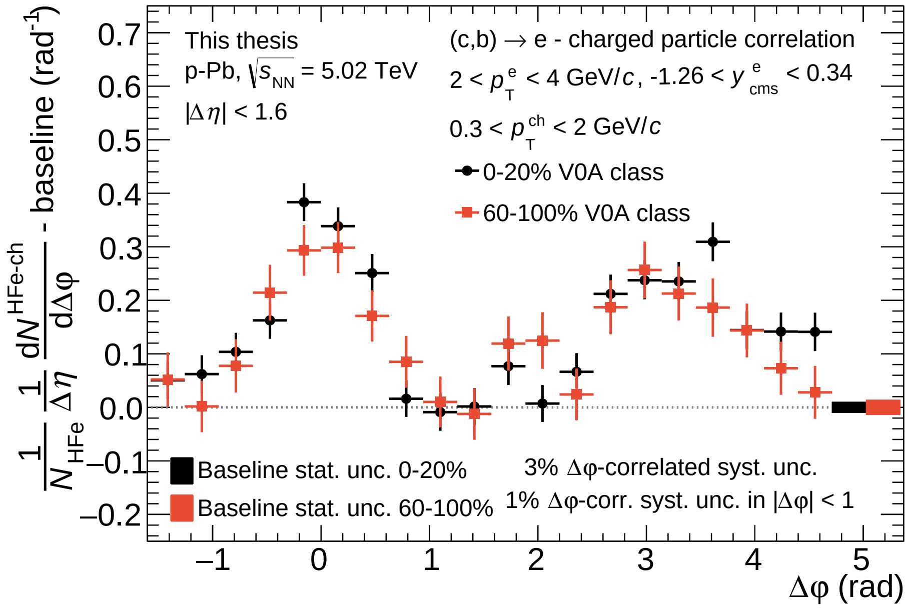

Figure 6.3: Azimuthal correlations between heavy-flavour decay electrons and charged particles, for high-multiplicity (red circles) and low-multiplicity (magenta triangle) p–Pb collisions, after subtracting the baseline. The distributions shown are for $2 < p_T^e < 4$ GeV/c and $0.3 < p_T^{ch} < 2$ GeV/c.

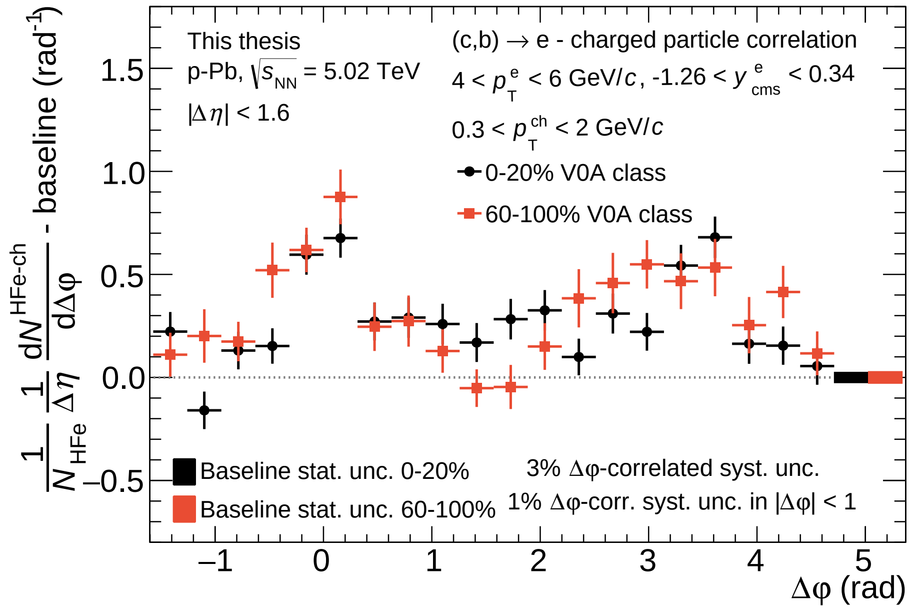

Figure 6.4: Azimuthal correlations between heavy-flavour decay electrons and charged particles, for high-multiplicity (red circles) and low-multiplicity (magenta triangle) p–Pb collisions, after subtracting the baseline. The distributions shown are for $4 < p_{\mathrm{T}}^{\mathrm{e}} < 6$ GeV/c and $0.3 < p_{\mathrm{T}}^{\mathrm{ch}} < 2$ GeV/c.

6.4 Systematic uncertainties on the azimuthal correlation distribution

The systematic uncertainties on the azimuthal correlation distribution can originate from:

(i) Potential biases in the procedure employed to select electron candidates and estimate the hadron contamination;

(ii) Removal of the background electrons not produced in heavy-flavor hadron decays;

(iii) Choice of the associated particle selection.

Each one of these items was studied to access the systematic uncertainties. The procedure is described below and the specific cuts varied are reported on Table 6.1.

A systematic uncertainty related to the electron reconstruction efficiency arises from imprecisions in the description of the detector response. It was studied by varying the electron selection in the ITS and TPC. The uncertainty affecting the removal of the hadron contamination was estimated by varying the particle identification criteria in the TPC ($n_{\sigma}^{\mathrm{TPC}}$). A total uncertainty of less than 0.5% was estimated from these sources.

Table 6.1: Sources of systematic uncertainties studied.

Variable/Method	**Default**	**Alternative values**
Tracking and particle identification		
Minimum number of clusters on the TPC	100	80 120
Nσ in the TPC	-0.5 to 3.0	-0.75 to 3.0 -1.0 to 3.0
Distance of closest approximation to the primary vertex (xy/z)	0.25 cm /1 cm	1 cm/2 cm 1.5 cm / 2.5 cm
Minimum Number of Clusters on the ITS	2	3 4
Non-heavy-flavour electron identification		
Maximum Invariant Mass	140 MeV/c^2	160 MeV/c^2 120 MeV/c^2 100 MeV/c^2
Minimum value of p_{T} to reconstruct the pair	0.10 GeV/c	0.15 GeV/c 0.20 GeV/c 0.25 GeV/c
Minimum number of TPC points	50	60 70 80
Secondary hadrons contamination		
Distance of closest approximation to the primary vertex (xy/z)	0.25 cm /1 cm	0.5 cm / 1 cm 0.75 cm / 1 cm 1 cm / 1 cm

The uncertainty related to the efficiency of finding the partner electron and to the stability of the S_{NonHFe} distribution, evaluated from its two contributions $S^{\mathrm{ID}}_{\mathrm{NonHFe}}$ and $S^{\mathrm{nonID}}_{\mathrm{NonHFe}}$, was studied by varying the selection for partner tracks and pair invariant mass, resulting in an uncertainty of less than 0.5%.

The uncertainty on the associated track reconstruction efficiency, obtained by varying the associated track selection criteria and by comparing the probabilities of track prolongation from TPC to ITS in data and simulations, was estimated to be 3% [54].

A systematic effect due to the contamination of the associated particles by secondaries comes from the residual discrepancy between Monte Carlo and data in the relative abundances of particle species and was studied by varying the selection on the distance of closest approach to the primary vertex. It was quantified to be 1% (correlated in $\Delta\varphi$), with an additional 1% (correlated) for $|\Delta\varphi| <1$.

Combining the uncertainties from all the above sources results in a 3% total systematic uncertainty (correlated in $\Delta\varphi$) and an additional 1% (also correlated) for $|\Delta\varphi| < 1$, as reported on Table 6.1.

Table 6.2: Summary of systematic uncertainties at correlation level

Systematic uncertainty (%)	$\mathbf{p_T}$ range [GeV/c]		
	1.5 - 2	2 - 4	4 - 6
Tracking and particle identification	$< 0.5\%$	$< 0.5\%$	$< 0.5\%$
Non-heavy-flavour identification	$< 0.5\%$	$< 0.5\%$	$< 0.5\%$
Hadron tracking	3%	3%	3%
Secondary hadrons cont.	1% (+ 1% NS)	1% (+ 1% NS)	1% (+ 1% NS)
Total	3% (+ 1% NS)	3% (+ 1% NS)	3% (+ 1% NS)

6.5 Chapter summary

The two-particle correlations between electron from heavy-flavour hadron decay and charged particles in high- and low-multiplicity collisions was reported for the electron p_T ranges $1.5 < p_T^e < 2$ GeV/c, $2 < p_T^e < 4$ GeV/c and $4 < p_T^e < 6$ GeV/c; and charged particles interval $0.3 < p_T^c h < 2$ GeV/c. No modification from high to low-multiplicity is found with the available statistical uncertainties. In case the effect observed for light-flavour hadrons was also present, the current uncertainties would not allow us to drive conclusions. This motivated to repeat the analysis in a larger data sample in the LHC Run 2, as it will be discussed in the next chapter.

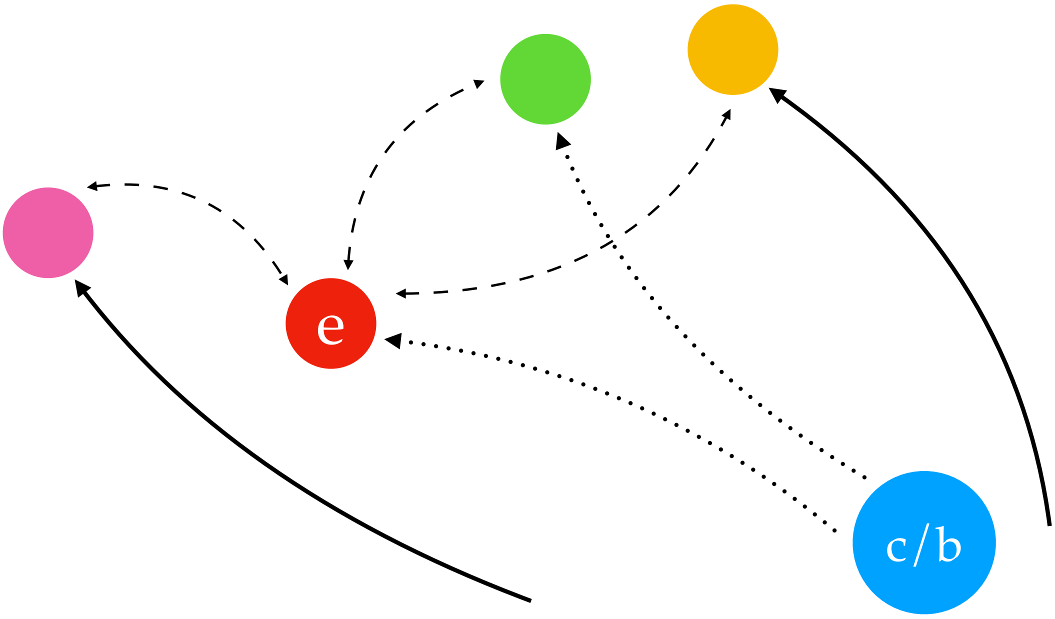

7 — Heavy-flavor electron v_2 in high-multiplicity p–Pb collisions

Although the procedure was fully validated during the Run 1 analysis discussed in the previous chapter, the statistical uncertainty was not enough to address the question about the presence of long-range angular correlations in the heavy-flavor electron – charged particles correlations in p–Pb collisions.

This raised the interest of repeating the analysis using another recently collected data sample. The results of this study were compiled into a paper, available in Ref. [134]. This new data sample has approximately six times more events and was vital to obtain the v_2 results. The extraction of the v_2 was carried out using a method to subtract the contribution from jets.

In this chapter, the information about the data sample analyzed and data taking conditions are described in Sec. 7.1. Then the correlation functions are presented on Sec. 7.2, including a brief report of the systematic uncertainties. The modifications from high and low multiplicity collisions are studied in Sec. 7.3 and the v_2 is extracted and reported on Sec. 7.4. Further discussion of the results is provided in Chapter 9.

7.1 Data sample

The data sample used for the analysis was collected in 2016 during the LHC p–Pb run at $\sqrt{s_{\rm NN}} = 5.02$ TeV. This was a special run requested by ALICE aiming to increase significantly the total number of events when compared to the Run 1 in 2013. This is especially important for analysis involving heavy-flavor particles that require a considerable number of events.

The center-of-mass reference frame of the nucleon-nucleon collision was shifted in rapidity by 0.465 units in the proton direction with respect to the laboratory frame, due to the different per-nucleon energies of the proton and the lead beams. The events were recorded using a minimum-bias trigger which required coincident signals in the V0-A and V0-C arrays. All the data was taken with this trigger setting and one of the ALICE detectors, the SDD, was only partially enabled. The events were recorded even in case the SDD was not ready for data taking, producing events with no information from the SDD. This impacted in a few percents on the efficiency of the tracking algorithm and half of the events were collected in this configuration. The total amount of data is more than 6 times the one recorded in Run 1. Only events with a primary vertex reconstructed within ±10 cm from the center of the detector along the beam axis were considered. After the selection, about 6×10^8 events were analyzed (integrated luminosity of 295 ± 11 μb^{-1}), avoiding areas where the acceptance of ALICE would be affected. Only events in high (0–20%) and low multiplicity (60–100%) classes, evaluated using the amplitude of the signal in the V0-A detector [133], were considered.

7.2 Azimuthal correlation distributions

The analysis procedure followed the one described in Chapter 5. The two-dimensional correlation distribution was projected onto $\Delta\varphi$ for $|\Delta\eta| < 1.2$ and divided by the width of the selected $\Delta\eta$ interval. In order to compare the jet-induced correlation peaks from different multiplicity ranges, a "baseline" term, constant in $\Delta\varphi$, was calculated from the weighted average of the three lowest points of the correlation. The resulting correlation distributions in the two considered multiplicity classes (0–20% and 60–100%) are shown in Figs. 7.1 and 7.2. An enhancement of the near- and away-side peaks is present in high-multiplicity collisions and it will be quantified in the next section. But first, the systematic uncertainties in the correlation function are discussed in the next subsection.

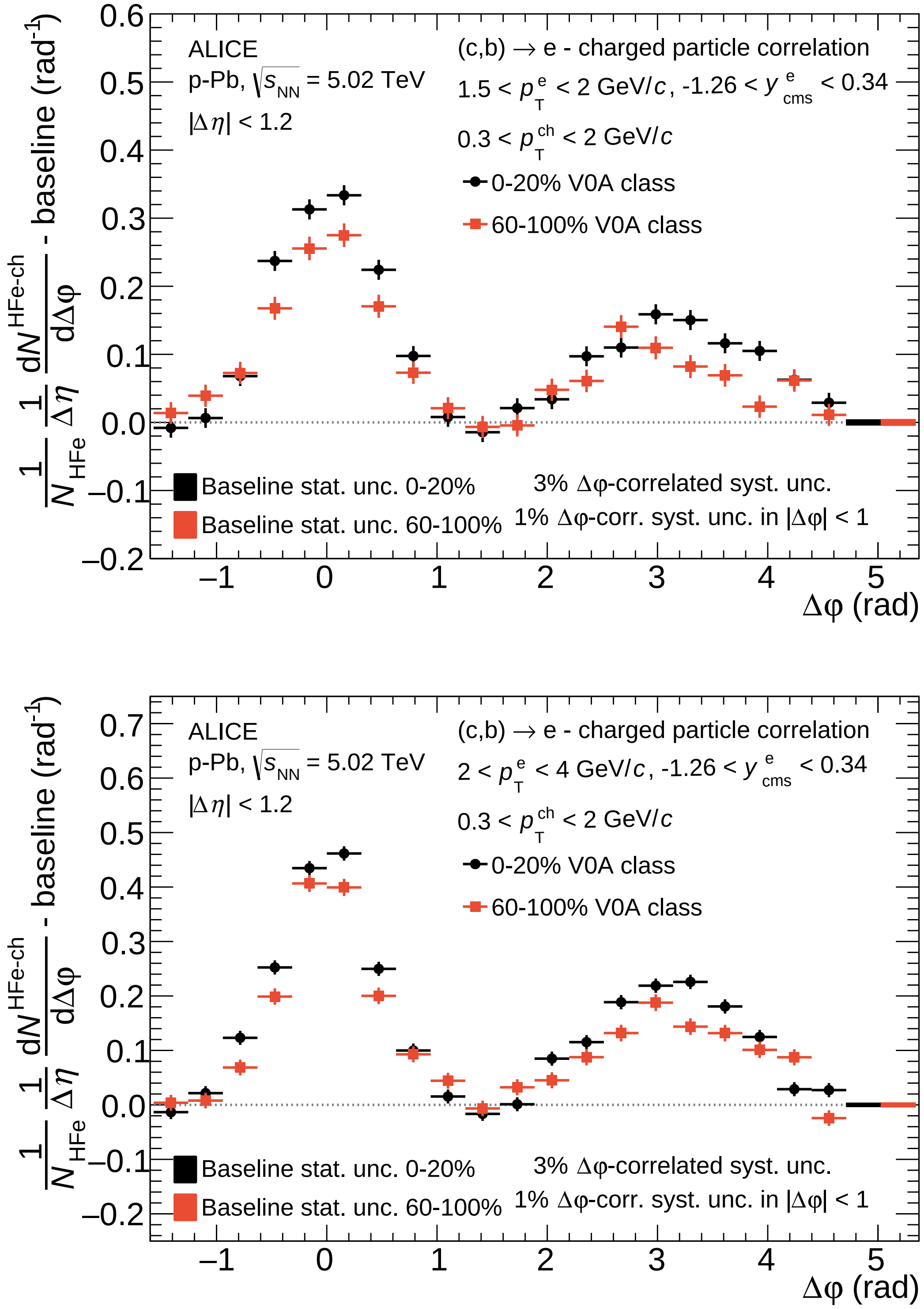

Figure 7.1: Azimuthal correlations between heavy-flavor decay electrons and charged particles, for high-multiplicity (black circles) and low-multiplicity (red squares) p–Pb collisions, after subtracting the baseline. The distributions are shown for $1.5 < p_T^e < 2$ GeV/c (top) and $2 < p_T^e < 4$ GeV/c (bottom); and $0.3 < p_T^{ch} < 2$ GeV/c. Only statistical uncertainties are shown as error bars. The statistical uncertainties on the baseline subtraction are shown as boxes at $\Delta\varphi \approx 5$.

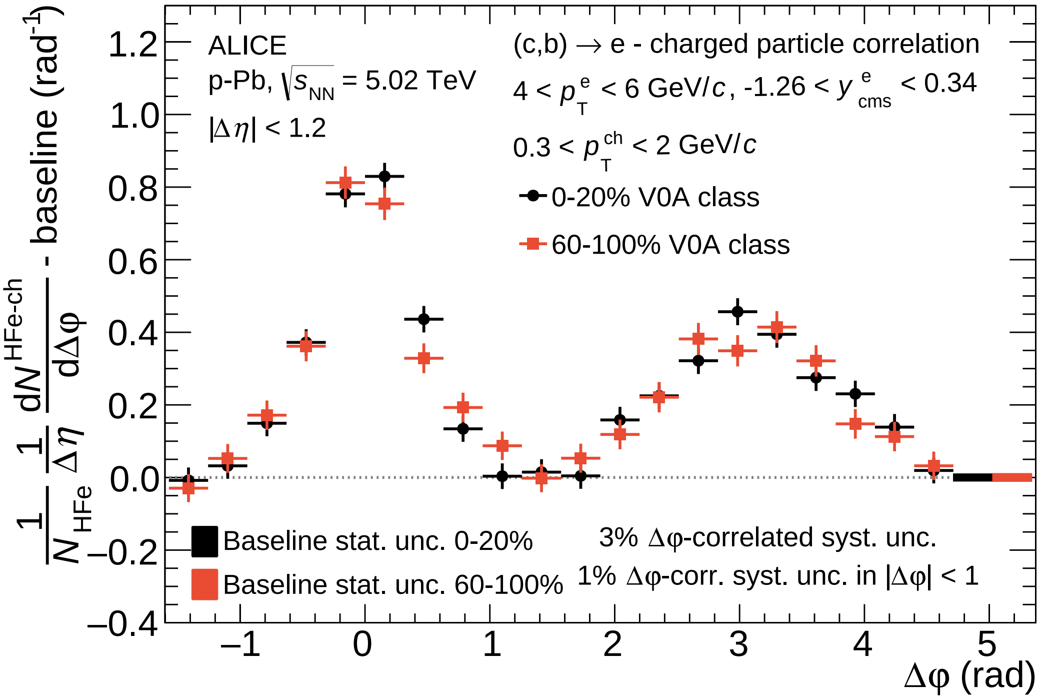

Figure 7.2: Azimuthal correlations between heavy-flavor decay electrons and charged particles, for high-multiplicity (black circles) and low-multiplicity (red squares) p–Pb collisions, after subtracting the baseline. The distributions are shown for $4 < p_T^e < 6$ GeV/c and $0.3 < p_T^{ch} < 2$ GeV/c. Only statistical uncertainties are shown as error bars. The statistical uncertainties on the baseline subtraction are shown as boxes at $\Delta\varphi \approx 5$.

7.2.1 Systematic uncertainties

The estimation of the systematic uncertainties was performed following the same procedure adopted in the Run 1 analysis, as described in Sec. 6.4. The systematic was grouped into three classes that correspond to a possible bias in the analysis. A few default values were changed from Run 1 to Run 2 and all the variations are reported again on Table 7.1. There groups are:

(i) **Tracking and particle identification**, where a potential biases in the procedure employed to select electron candidates and estimate the hadron contamination could arise from the imprecision in the description of the detector response. This source was studied by varying the electron selection in the main tracking detectors, the ITS and the TPC, such as the number of clusters required in each detector. The hadron contamination and its systematic uncertainties were studied by varying the particle identification criteria in the TPC (n_σ^{TPC}). A total uncertainty of less than 0.5% was estimated in all the momentum range. Most of the uncertainties cancel since the correlation distributions are normalized to the number of electrons;

(ii) **Non-heavy-flavour electron identification**, which is related to biases in the process of the removal of background electrons (the ones not coming from heavy-flavor hadron decays). The efficiency of finding the partner electron can be biased by differences in the simulations and data. The simulations where reweighted to match the same cross section of π^0 and η in data, the main background sources, and this process has its statistical and systematical limitations. The systematic uncertainties are studied by checking stability of the correlation function of non-heavy-flavour electrons (S_{NonHFe} distribution), evaluated from its two contributions $S^{\mathrm{ID}}_{\mathrm{NonHFe}}$ and $S^{\mathrm{nonID}}_{\mathrm{NonHFe}}$, when varying the selection for partner tracks and pair invariant mass. The effect on the correlation function of heavy-flavor electron and charged particles is less than 0.5%;

(iii) **Choice of the associated particle selection**. The main component is linked to the uncertainty on the associated track reconstruction efficiency. A detailed study was performed in Ref. [54] and was estimated to be 3%. The value was obtained by varying the associated track selection criteria and by comparing the probabilities of track prolongation from TPC to ITS in data and simulations. Another possible source of systematical uncertainties is the contamination from secondary particles. It comes from the residual discrepancy between Monte Carlo and data in the relative abundances of particle species. The distance of closest approach to the primary vertex was varied to evaluate the impact of these discrepancies. It was found to be 1% (correlated in $\Delta\varphi$), with an additional 1% (correlated) for $|\Delta\varphi| < 1$.

Combining the uncertainties from all the sources mentioned in this section, a total of 3% total systematic uncertainty (correlated in $\Delta\varphi$) and an additional 1% (also correlated) for $|\Delta\varphi| < 1$ is found. The conclusion on the final values of the systematic uncertainties is the same as in Sec. 6.4 and are reported on Table 7.2.

Table 7.1: Sources of systematic uncertainties studied.

Variable/Method	**Default**	**Alternative values**
Tracking and particle identification		
Minimum number of clusters on the TPC	100	80 120
Nσ in the TPC	-1.0 to 3.0	-0.75 to 3.0 -0.5 to 3.0
Distance of closest approximation to the primary vertex (xy/z)	0.25 cm /1 cm	1 cm/2 cm 1.5 cm / 2.5 cm
Minimum Number of Clusters on the ITS	2	3 4
Non-heavy-flavour electron identification		
Maximum Invariant Mass	140 MeV/c^2	160 MeV/c^2 120 MeV/c^2 100 MeV/c^2
Minimum value of p_{T} to reconstruct the pair	0.15 GeV/c	0.10 GeV/c 0.20 GeV/c 0.25 GeV/c
Minimum number of TPC points	50	60 70 80
Secondary hadrons contamination		
Distance of closest approximation to the primary vertex (xy/z)	0.25 cm /1 cm	0.5 cm / 1 cm 0.75 cm / 1 cm 1 cm / 1 cm

Table 7.2: Summary of systematic uncertainties at correlation level

Systematic uncertainty (%)	$\mathbf{p_T}$ range [GeV/c]		
	1.5 - 2	2 - 4	4 - 6
Tracking and particle identification	$< 0.5\%$	$< 0.5\%$	$< 0.5\%$
Non-heavy-flavour identification	$< 0.5\%$	$< 0.5\%$	$< 0.5\%$
Hadron tracking	3%	3%	3%
Secondary hadrons cont.	1% (+ 1% NS)	1% (+ 1% NS)	1% (+ 1% NS)
Total	3% (+ 1% NS)	3% (+ 1% NS)	3% (+ 1% NS)

7.3 Modulation of the azimuthal correlation function in high-multiplicity collisions

To study the enhancement of the near- and away-side peaks, the baseline-subtracted correlation distribution obtained in low-multiplicity events was subtracted from the correlation distribution measured in high-multiplicity events, as described in [90]. This removes the jet-induced correlation peaks, under the assumption that they are the same in low- and high-multiplicity events. The correlation distribution was restricted to the $(0,\pi)$ range by reflecting the symmetrical points. The resulting distribution shows an azimuthal anisotropy compatible with the presence of a dominant second-order ($V_{2\Delta}^{\mathrm{HFe-ch}}$) modulation in its Fourier decomposition, as shown in Fig. 7.3. The $V_{2\Delta}^{\mathrm{HFe-ch}}$ coefficient was quantified by fitting the distribution with the function:

$$\frac{1}{\Delta\eta}\frac{1}{N_{\mathrm{HFe}}}\frac{\mathrm{d}N_{\mathrm{HFe-ch}}(\Delta\varphi)}{\mathrm{d}\Delta\varphi} = a[1 + 2V_{1\Delta}^{\mathrm{HFe-ch}}\cos(\Delta\varphi) + 2V_{2\Delta}^{\mathrm{HFe-ch}}\cos(2\Delta\varphi)]. \tag{7.1}$$

The measured $V_{2\Delta}^{\mathrm{HFe-ch}}$ in high-multiplicity events does not exclude the possibility of having a $V_{2\Delta}^{\mathrm{HFe-ch}}$ contribution in the low-multiplicity events, as described in [135].

The values of $V_{2\Delta}^{\mathrm{HFe-ch}}$ obtained from the fit in the three $p_{\mathrm{T}}^{\mathrm{e}}$ intervals are reported on Table 7.3. The $V_{1\Delta}^{\mathrm{HFe-ch}}$ fit values are compatible with zero in all the $p_{\mathrm{T}}^{\mathrm{e}}$ intervals. The measured $V_{2\Delta}^{\mathrm{HFe-ch}}$ is larger than zero with a significance of 4.6σ for the $2 < p_{\mathrm{T}}^{\mathrm{e}} < 4$ GeV/c range. The significance for $V_{2\Delta}^{\mathrm{HFe-ch}} > 0$ in at least one of the $p_{\mathrm{T}}^{\mathrm{e}}$ intervals , $1.5 < p_{\mathrm{T}}^{\mathrm{e}} < 2$ GeV/c and $2 < p_{\mathrm{T}}^{\mathrm{e}} < 4$ GeV/c, combining statistical and systematical uncertainties to calculate the probability, is more than 6σ.

Table 7.3: $V_{2\Delta}^{\mathrm{HFe-ch}}$ obtained by fitting the jet-subtracted correlation function

$\mathbf{p_T^e}$ **range (GeV/c)**	$\mathbf{V_{2\Delta}^{HFe-ch}}$	**Significance (nσ)**
$1.5 < p_{\mathrm{T}}^{\mathrm{e}} < 2$	0.0038 ± 0.0008(stat) $\pm$ 0.0006(syst)	3.8
$2 < p_{\mathrm{T}}^{\mathrm{e}} < 4$	0.0040 ± 0.0007(stat) $\pm$ 0.0005(syst)	4.6
$4 < p_{\mathrm{T}}^{\mathrm{e}} < 6$	0.0019 ± 0.0019(stat) $\pm$ 0.0003(syst)	1.0

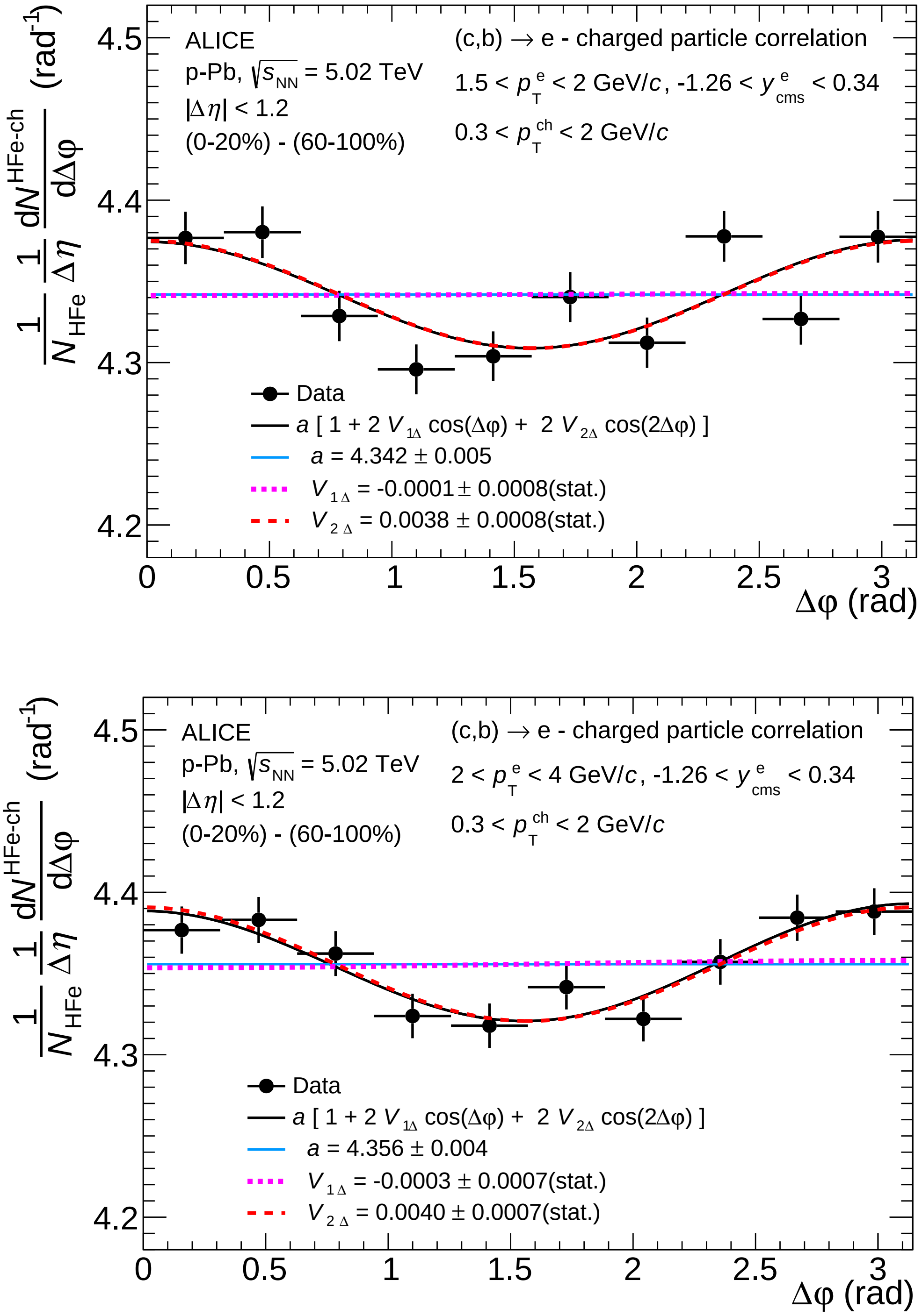

Figure 7.3: Azimuthal correlation distribution between heavy-flavor decay electrons and charged particles, for high-multiplicity p–Pb collisions after subtracting the jet contribution based on low-multiplicity collisions. The distribution is shown for $1.5 < p_{\mathrm{T}}^{\mathrm{e}} < 2$ GeV/c (top) and $2 < p_{\mathrm{T}}^{\mathrm{e}} < 4$ GeV/c (bottom); and $0.3 < p_{\mathrm{T}}^{\mathrm{ch}} < 2$ GeV/c. The best fit (Eq. 7.1) to the data points is shown as black solid line. The cyan solid line, pink dotted and red dashed lines indicate the fit parameter a, and the $\cos(\Delta\varphi)$, $\cos(2\Delta\varphi)$ modulations around that value due to the $V_{1\Delta}$ and $V_{2\Delta}$ terms, respectively.

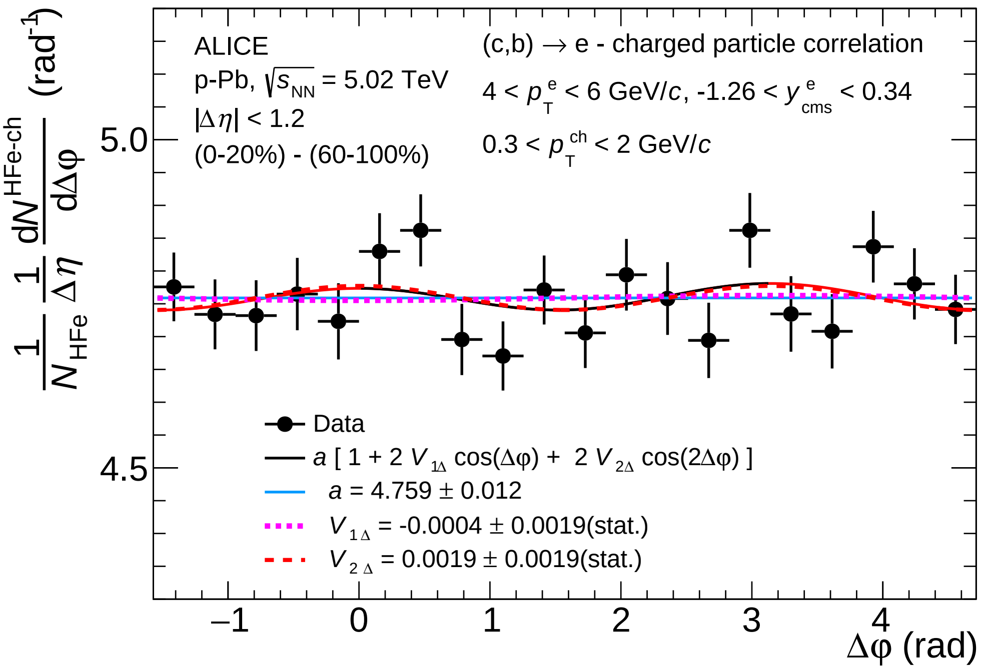

Figure 7.4: Azimuthal correlation distribution between heavy-flavor decay electrons and charged particles, for high-multiplicity p–Pb collisions after subtracting the jet contribution based on low-multiplicity collisions. The distribution is shown for $4 < p_T^e < 6$ GeV/c and $0.3 < p_T^{ch} < 2$ GeV/c. The best fit (Eq. 7.1) to the data points is shown as black solid line. The cyan solid line, pink dotted and red dashed lines indicate the fit parameter a, and the $\cos(\Delta\varphi)$, $\cos(2\Delta\varphi)$ modulations around that value due to the $V_{1\Delta}$ and $V_{2\Delta}$ terms, respectively.

7.3.1 Systematic uncertainties

The sources of systematic uncertainties mentioned on Sec. 7.2.1 are also present in the $V_{2\Delta}^{\mathrm{HFe-ch}}$ and were also studied here using the variations listed on the Table 7.1.

The uncertainty related to the electron selection and the identification of non-heavy-flavor decay electrons on $V_{2\Delta}^{\mathrm{HFe-ch}}$ were quantified to be about 2–3% and 5%, respectively. The contamination of the associated particles by secondaries leads to a 3% systematic uncertainty.

Other sources that are specific for the $V_{2\Delta}^{\mathrm{HFe-ch}}$ extraction were also studied. In order to test whether the observed modulation and the non-zero $V_{2\Delta}^{\mathrm{HFe-ch}}$ could originate from a residual jet contribution, due to possible differences between the jet structures in low- and high-multiplicity collisions, the $\Delta\eta$ range used to obtain the $\Delta\varphi$ projection was varied. The observed variation on $V_{2\Delta}^{\mathrm{HFe-ch}}$ was 11–15%, depending on the electron p_{T} interval, and was taken as the systematic uncertainty from the jet subtraction. The stability of the $V_{2\Delta}^{\mathrm{HFe-ch}}$ value against the variation of the $\Delta\eta$ range suggests a long-range nature of the observed anisotropy. The inclusion of a $V_{3\Delta}^{\mathrm{HFe-ch}}$ term in the fit function, in Eq. 7.1, affects the $V_{2\Delta}^{\mathrm{HFe-ch}}$ estimation by less than 0.5%.

A summary of the values obtained for the $V_{2\Delta}^{\mathrm{HFe-ch}}$ is listed on Table 7.3 and its systematical uncertainties are on Table 7.4. Combining the different uncertainty sources results in a total systematic uncertainty on $V_{2\Delta}^{\mathrm{HFe-ch}}$ of 13–16% depending on $p_{\mathrm{T}}^{\mathrm{e}}$.

Table 7.4: Summary of systematic uncertainties on the $V_{2\Delta}$

Systematic uncertainty (%)	**1.5-2 GeV/c**	**2-4 GeV/c**	**4-6 GeV/c**
Tracking and particle identification	3%	2%	2%
Non-heavy-flavor identification	5%	5%	5%
Secondary hadrons contamination	3%	3%	3%
$\Delta\eta$ dependence and jet contamination	15%	11%	11%
v_3 inclusion	0.5%	0.5%	0.5%
Total $V_{2\Delta}$	16%	13%	13%

7.4 Azimuthal anisotropy of heavy-flavor electrons

Assuming its factorization in single-particle v_2 coefficients [95], the $V_{2\Delta}^{\mathrm{HFe-ch}}$ can be expressed as the product of the second-order Fourier coefficients of the heavy-flavor decay electron (v_2^{HFe}) and charged particle (v_2^{ch}) azimuthal distributions, hence $v_2^{\mathrm{HFe}} = V_{2\Delta}^{\mathrm{HFe-ch}}/v_2^{\mathrm{ch}}$. The v_2^{ch} value in the range $0.3 < p_{\mathrm{T}}^{\mathrm{ch}} < 2$ GeV/c was obtained from the weighted average of the values measured in smaller $p_{\mathrm{T}}^{\mathrm{ch}}$ ranges in [95], providing v_2^{ch} = 0.0594 ± 0.0010(stat) ± 0.0059 (syst).

The v_2^{HFe} values are reported in Fig. 7.5 and compared to those measured for charged particles, dominated by light-flavor hadrons, and inclusive muons at large rapidity (in p-going and Pb-going directions), which are mostly coming from heavy-flavor hadron decays for $p_{\mathrm{T}} > 2$ GeV/c. The strength of the modulation for heavy-flavor particles is smaller than the one for light-flavor particles, although the uncertainties are large and the p_{T} interval of electron parents (heavy-flavor hadrons) is considerably broader than the range addressed in the light-flavor hadron measurement. The comparison of v_2^{HFe} at mid-rapidity with v_2 of inclusive muons at forward and backward rapidity is not straightforward, due to the different cold nuclear matter effects affecting heavy-flavor production at different rapidities [136] and to the non-heavy-flavor contamination for muons at low $\bar{p}_{\mathrm{T}}$. The values are comparable in the range addressed by both analyses. A comparison of v_2^{HFe} with the J/ψ results [137] is also challenging, considering the different production process of heavy quarks to open and hidden mesons, and is not presented here. The v_2^{HFe} in p–Pb collisions is found to be similar in magnitude to the one in non-central Pb–Pb collisions at $\sqrt{s_{\mathrm{NN}}} = 2.76$ TeV [138]. The significance for $v_2^{\mathrm{HFe}} > 0$ is 5.1σ for $1.5 < p_{\mathrm{T}}^{\mathrm{e}} < 4$ GeV/c, which provides a very strong indication for the presence of long-range anisotropies for heavy-flavor particles also in

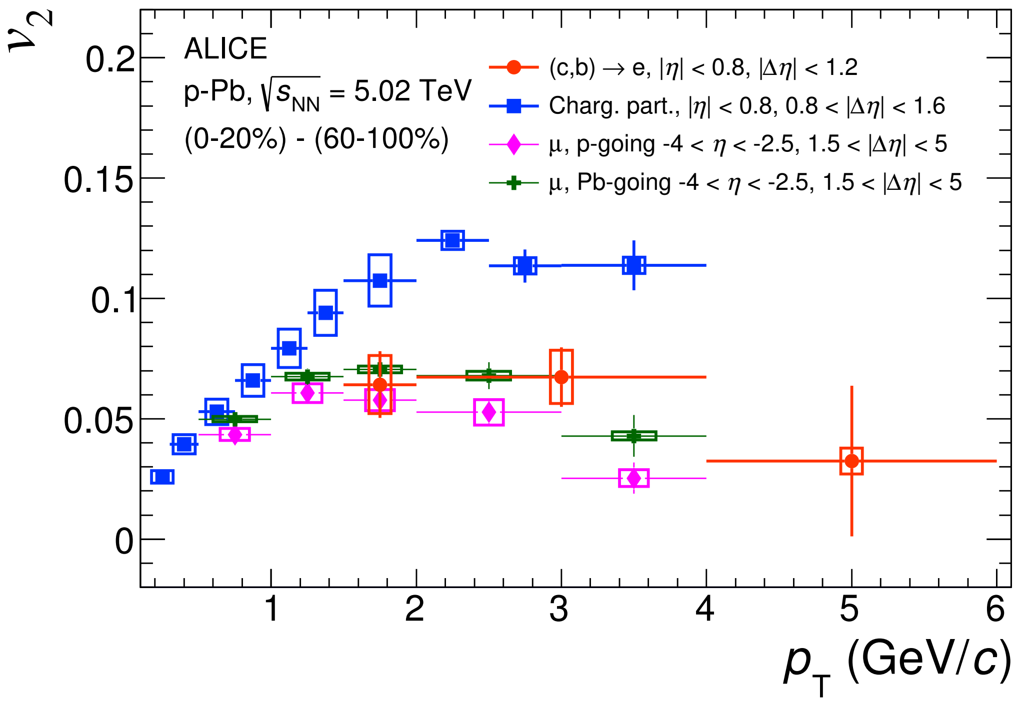

Figure 7.5: Heavy-flavor hadron decay electron v_2 as a function of transverse momentum compared to the v_2 of unidentified charged particles [95] and inclusive muons at forward rapidities [139]. Statistical and systematic uncertainties are shown as bars and boxes, respectively.

high-multiplicity p–Pb collisions.

7.5 Chapter summary

In summary, we report the measurement of v_2 for open heavy-flavor particles at mid-rapidity in high-multiplicity p–Pb collisions. The analysis was carried out via a Fourier decomposition of the azimuthal correlation distribution between heavy-flavor decay electrons and charged particles. After the removal of the jet contribution a $V_{2\Delta}$-like modulation was obtained in the high-multiplicity correlation distributions, similarly to what was previously observed for light-flavor di-hadron correlations. A fit to the correlation distributions was used to characterize the modulation. The heavy-flavor decay electron v_2 was found to be smaller than the charged particle v_2 in the common p_T interval [90] and similar to the inclusive muon v_2 at forward and backward rapidities [139]. The measured heavy-flavor decay electron v_2 is positive with a significance of more than 5σ in the $1.5 < p_T^e < 4$ GeV/c range. This result complements previous measurements for light-flavor hadrons [90], providing new information on the behavior of heavy-flavor hadrons to understand the azimuthal anisotropies observed in small collision systems. The results are reported in a paper have been accepted by Physics Review Letters [134].

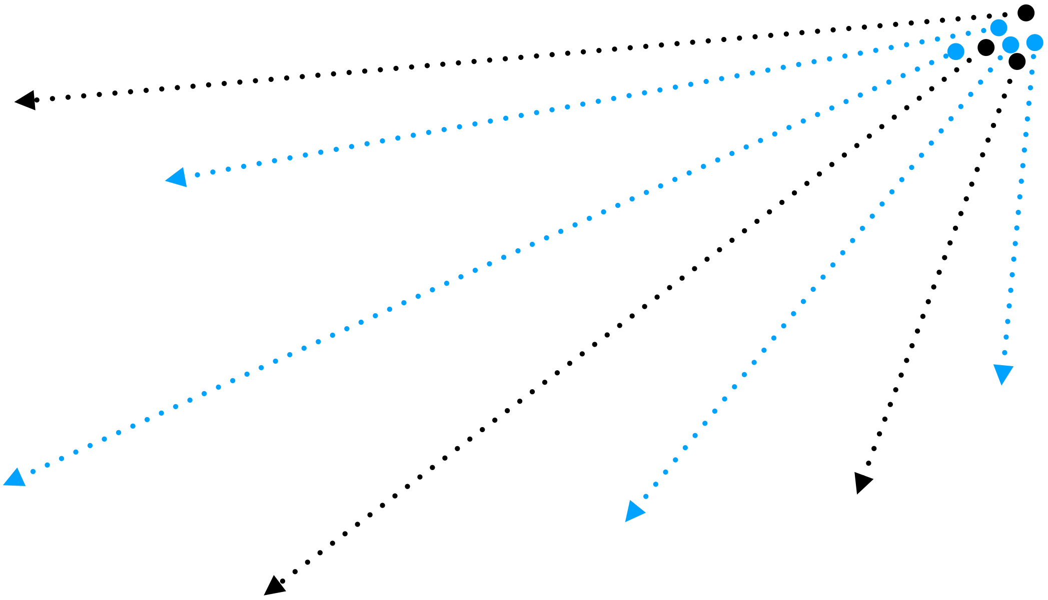

8 — Perspectives for heavy-flavor electron azimuthal anisotropy measurements in the LHC Run 3

The ALICE experiment will undergo a major upgrade during the years of 2019 and 2020. The detector will improve its capabilities by introducing new detectors and upgrading the capabilities of current detectors. The details of the whole upgrade program are found on Ref. [140]. The main upgrades include improvements on the TPC, ITS, muon spectrometer, and in the readout of the detectors. The software will also be redesigned, in the O^2 project [141], to match the huge amount of data generated.

In this chapter, the impact of such upgrades is briefly discussed. The main focus is to show the improvement of the measurement presented in the previous chapter. They are achieved mainly due to an increase in the total number of collected events. First, the key elements of the upgrade are reported, in both hardware and software levels. Then, the impacts of such increase on the number of events are discussed.

8.1 The ALICE upgrade

The ALICE experiment upgrade will change components of hardware and software. The hardware needs to handle higher interaction rates which demand faster readout and resistance to radiation. An illustration of the upgraded detector is shown in Fig. 8.1. The main changes at hardware level are briefly summarized below [140]:

- The Time Projection Chambers will have its readout upgraded. It will use gas electron multiplier (GEM) to provide a continuous readout. That will largely remove the TPC dead times, associated with the current readout technology (wired chambers). This is a major point of the upgrade since the TPC is the main tracking detector. At the same time, the TPC is one of the slowest detectors in ALICE. The upgrade will allow the TPC to take data at the rate provided by the LHC (50 kHz) keeping the current tracking capabilities. The ALICE Brazilian group is involved actively in the upgrade by designing part of the electronics needed for the detector [142]. The details of the TPC upgrade are available in Ref. [143].

- The Inner Tracking System has a new design that will improve the impact parameter resolution. The strip and drift layers will be removed and replaced by pixel layers. The upgraded ITS will use 7 layers of pixel detectors that contains less material budget. The new ITS will use Monolithic Active Pixel Sensors (MAPS) that will allow the silicon budget to be reduced by a factor of seven in comparison to the version of the ITS currently installed. With the upgrade, the pixel density will be increased by 50. All these improvements will provide better tracking at low momentum. The readout capabilities will also be upgraded. The readout rate will increase from 1 kHz in the current ITS to 100 kHz (Pb–Pb collisions) and 400 kHz (pp collisions) in the new ITS. The technical design report [144] presents each of those changes in detail.

- Reduction of the beampipe diameter from 29 mm to 17.2 mm. This reduction is vital for the new ITS. It will be possible to install the first layer of the ITS closer to the collisions and improve the resolution of the impact parameter.

- The muon spectrometer includes now tracking capabilities before the absorbers to increase the matching ratio with the ITS tracks.

- TRD, TOF, and PHOS detectors will have new readout electronics to support high rate operation.

- Forward detectors (V0 and T0) will be merged into a single and more precise detector.

The upgrade will allow the TPC, ITS, and TOF to record all minimum-bias Pb–Pb interactions at the rate of 50 kHz. Information from other detectors will be added to this minimum set whenever they are available. This upgrade required the efforts from the whole collaboration and its installation will take place during 2019 and 2020.

On the software side, the total amount of data will increase by a factor of 100 with respect to Run 1 and Run 2. The current data rate for Pb–Pb collisions is of about 10 GB/s and after the upgrade it will reach 1 TB/s. The data taking rates will be 50 kHz for Pb–Pb collisions and 200 kHz for pp and p–Pb collisions. All the software is restructured to support this increase in demand, given that computation power and

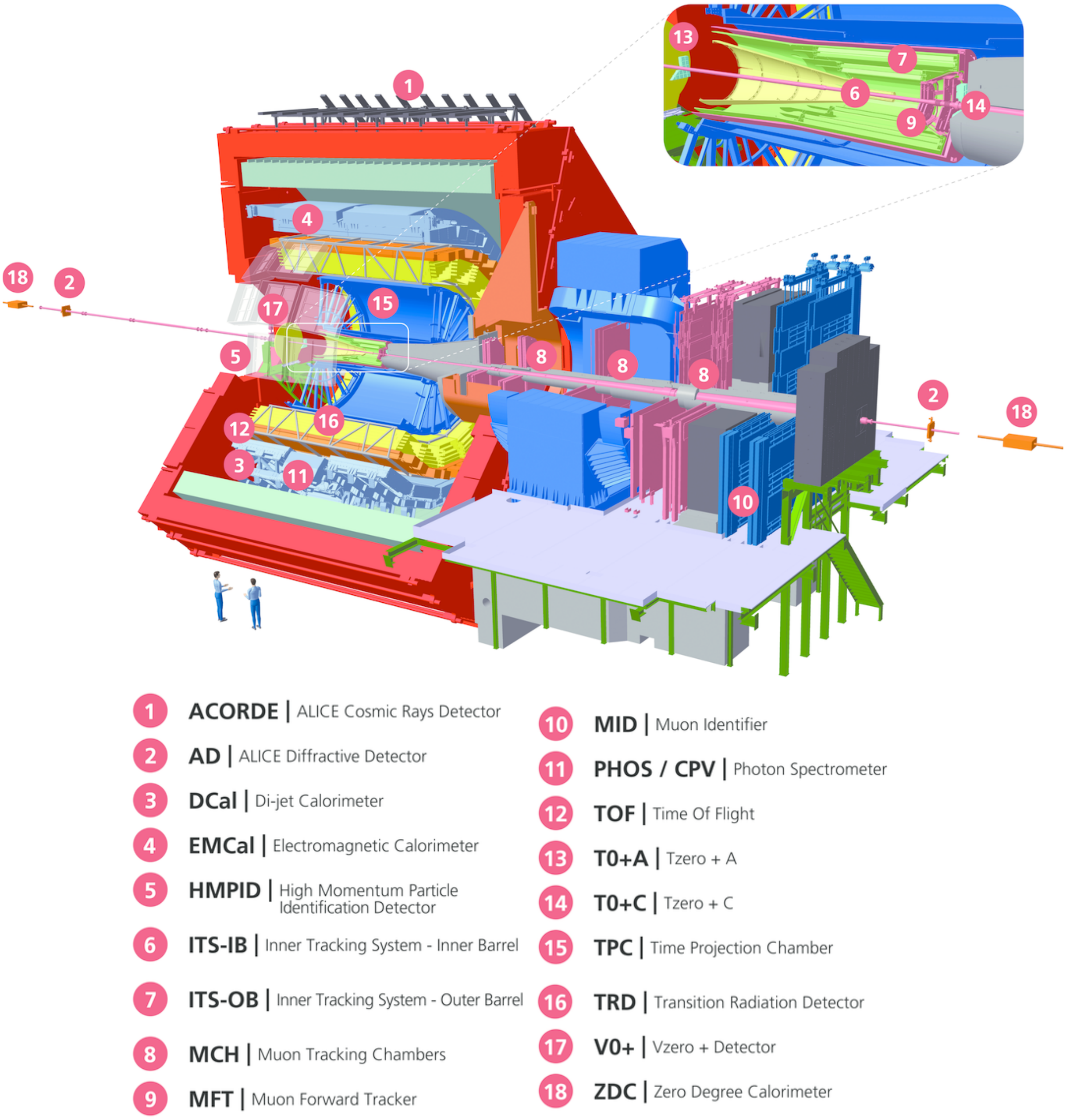

Figure 8.1: ALICE schematics for Run 3.

storage space did not increase by such factor. The merging of the online and offline (O^2) framework is the main change and it is reported are in detail in Ref. [141]. The data will be reconstructed in parallel with the data collection in a local computing system, the O^2 cluster, following the procedure reported in Fig. 8.2. The data will consist in structures denominated Time Frames, that contains the information obtained from detectors that take data continuously over a period of 20 ms, and triggered data for detectors that cannot take data continuously. The calibration with on-the-fly correction will allow the system to replace the original raw data with compressed and partially reconstructed data which will save a considerable amount of space. It is estimated that the size of one Time Frame on the TPC, which contains most of the data, can be reduced from a factor 20 using different compression techniques [143]. Refined calibrations will be employed offline to improve the final analysis.

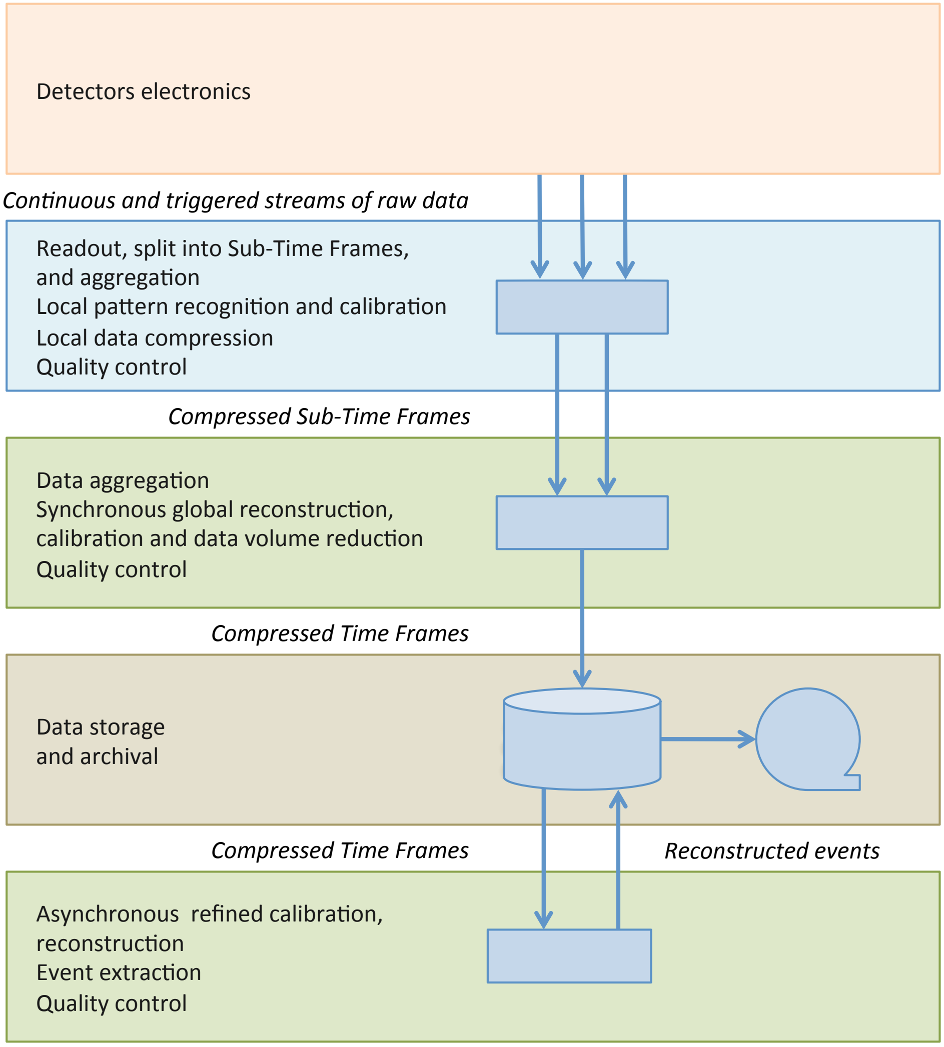

Figure 8.2: Data flow of the O^2 computing system for the LHC Run 3/4. Figure taken from Ref. [141].

8.2 Perspectives for heavy-flavor electron azimuthal anisotropy measurements during the LHC Run 3

The upgrade will drastically increase the number of events available for the analysis, which is the main limitation of measurements reported for the Run 2 analysis. The LHC will deliver up to 150 times more events in comparison to the p–Pb Run 2 measurement. Apart from a large number of events, the main new changes that impact on the measurement of the heavy-flavor electron v_2 analysis are those related to the tracking, impact parameter resolution, and material budget.

The new ITS will have approximately seven times less material budget than the current ITS which will result in fewer pairs of electrons and positrons produced by photonic conversions. In case the interaction with the material happens and the electron-positron pair is formed, the improved tracking down to very low momentum will help to identify them with much more precision. This is particularly important on the low momentum part of the analysis where the background is dominant. We expect to be able to extend the measurement to, at least, $p_T = 0.5$ GeV/c. Also, the improved impact parameter resolution will make it easier to separate electrons from charm and beauty. This will allow the study of the mass dependence in more details.

Unfortunately, no simulation with heavy-flavor electrons is available for the Run 3 upgrade yet, so it is not possible to access directly the effect of the upgrade on the results. Instead, the projections were performed using the data and simulations for Run 2, but extrapolating the results in thinner bins and in a broader momentum range. The v_2 was assumed to increase linearly from $p_T = 0$ up to the bin where the Run 2 measurements are available. The result of this study is shown in Fig. 8.3 and 8.4. These studies are based on simplified simulations that take into account the correlation functions obtained with the Run 2 preliminary results, separately for signal and background. Each one of the components had its statistical uncertainty reduced based on the total number of events predicted for the Run 3. The statistical uncertainties in the v_2 will be smaller than 6% for all the momentum range. At intermediate momentum, the uncertainties will be less than 4% and the measurement will be likely limited only by the systematic uncertainties. The systematic uncertainties are also expected to decrease since they are dominated by the jet component subtraction. This component is related to the poor statistical uncertainties on the low multiplicity sample which does not allow the imposition of an η gap. The total gain will be even greater when we consider the improved detectors.

The ALICE upgrade will be of great benefit to the measurement of the v_2 of heavy-flavor decay electrons in p–Pb collisions. We expect that the statistical uncertainties will be enough to study the details of the mass dependence and it will be likely to

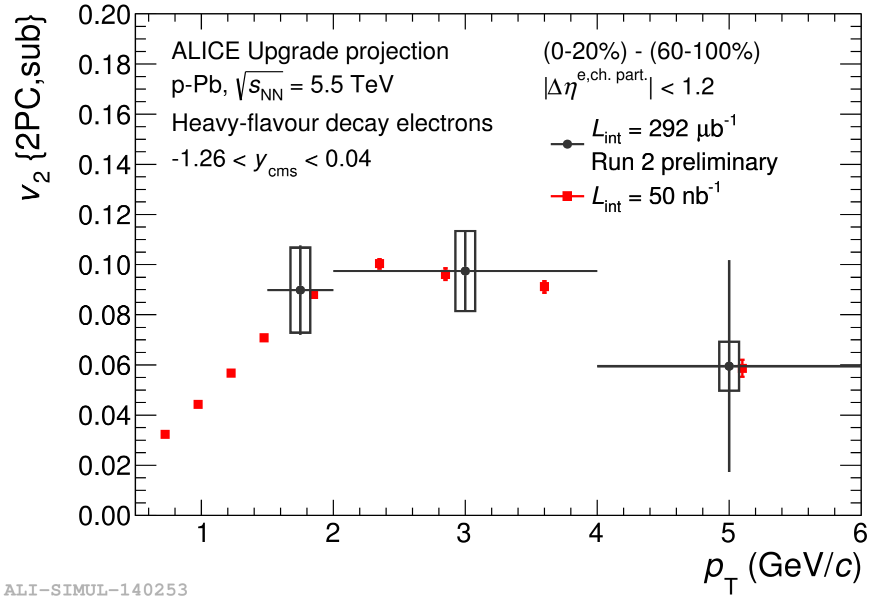

Figure 8.3: Projection for the heavy-flavor decay electron v_2 for Run 3 as a function of the transverse momentum compared to the preliminary results from Run 2. Statistical and systematic uncertainties are shown as bars and boxes, respectively.

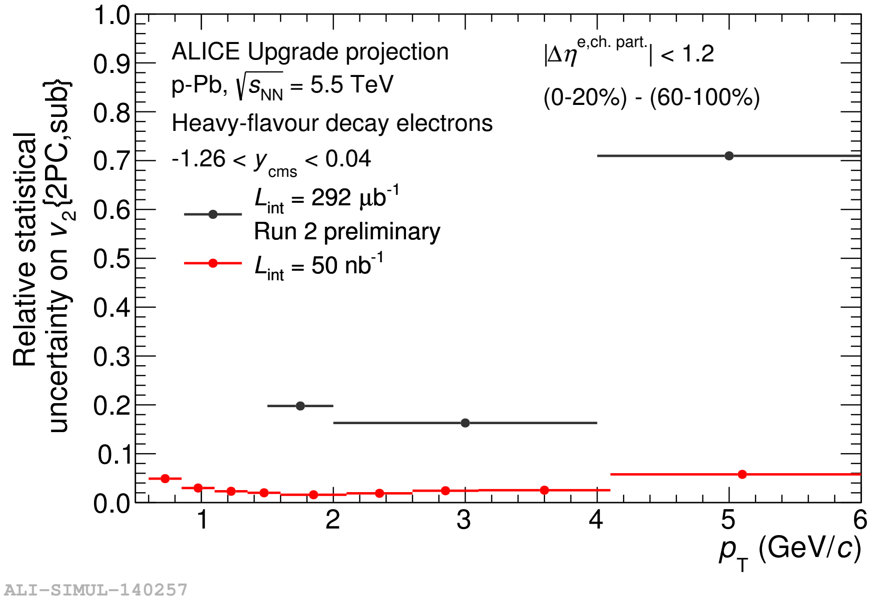

Figure 8.4: Projection for the statistical uncertainties of the heavy-flavor decay electron v_2 for Run 3 as a function of the transverse momentum compared to the preliminary results obtained in Run 2.

perform the separation of electrons from charm and beauty. Detailed studies are not possible yet, since no Run 3 simulations are available for heavy-flavor electrons. The upgrade will help to reduce both statistical uncertainties, by a factor of 12, or less in case the measurement is done in smaller p_T bins; and the systematical uncertainties, which need additional simulations to be quantified.

8.3 Chapter summary

In this brief chapter, the possibilities of performing the same measurement on the next data-taken period of the LHC (Run 3) was discussed. Most of the upgrade consists in an improved TPC and ITS. They will provide continuous readout and save all data taken. This data will move to a local cluster for further processing and reconstruction. We expect about 150 times more minimum bias p–Pb events to be collected during the Run 3 period, which will improve the statistical and systematical precision of the heavy-flavor electron v_2 measurement. The statistical uncertainties should be enough to study the mass dependence in more detail and likely perform the separation of charm and beauty electrons.

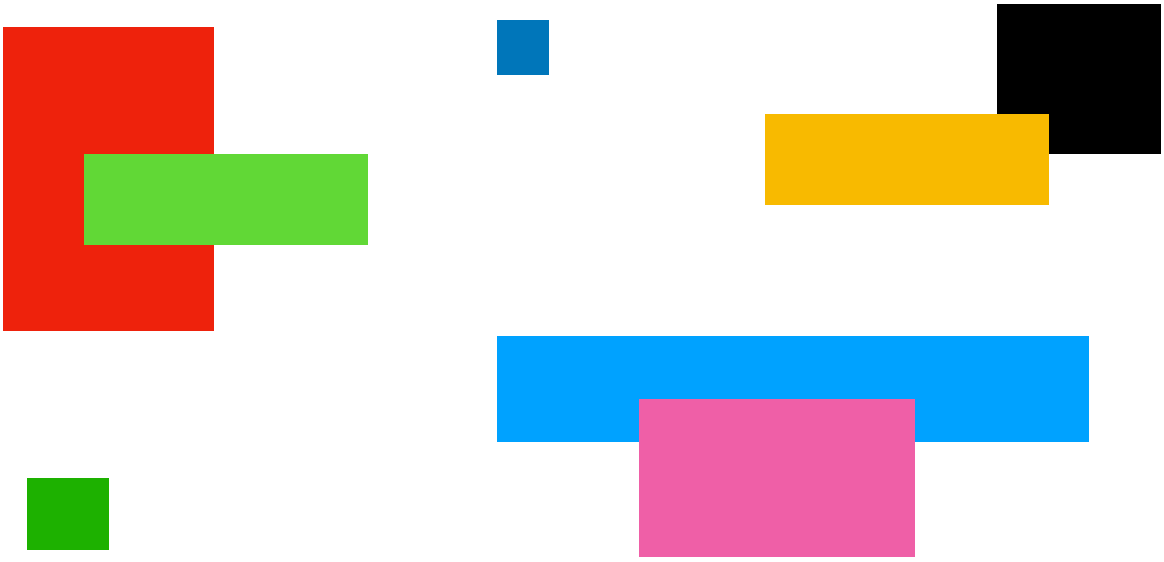

9 — Discussion and final remarks

The discovery of the long-range double-ridge structure on the two-particle correlation function has generated excitement on the particle/nuclear physics community. The main point of this discussion is that standard state-of-the-art generators, such as PYTHIA, were not able to describe this phenomenon. That raised the question: where does this effect come from?

Several studies have been performed to shed light into this problem. The first studies are with pp and those measurements were later extended with p–Pb collisions. The effect is quantified by the second Fourier coefficient (v_2) and it has been measured for different particle species. The v_2 follows a similar mass ordering in p–Pb and Pb–Pb collisions, as discussed in Chapter 3. Several measurements were presented in that chapter, to discuss the problem. Another recent result, shown in Fig. 9.1, is also very interesting and adds more information to this discussion. The v_2 is calculated using muti-particle cumulants with a different number of particles. In some cases, the additional η separation is imposed by diving the events into 2 or 3 sub-events. This is introduced to suppress the non-flow effects event more. We have to acknowledge that the v_2 is present in pp and p–Pb collisions even when more sophisticated techniques to suppress the non-flow effects are used. All the evidence points to a positive v_2 for charged particles that comes from genuine correlations between multi-particles. The results are less favorable to a v_2 coming from jets or resonances. In summary, the current understanding is that charged particles and light-flavored hadrons have a positive v_2 in small systems that are not coming from non-flow effects, following a mass ordering similar to the one observed in heavy-ion collisions.

The next step is the study of the v_2 for heavy quarks such as charm and beauty. In case the QGP is present in those collision systems, heavy quarks are interesting probes

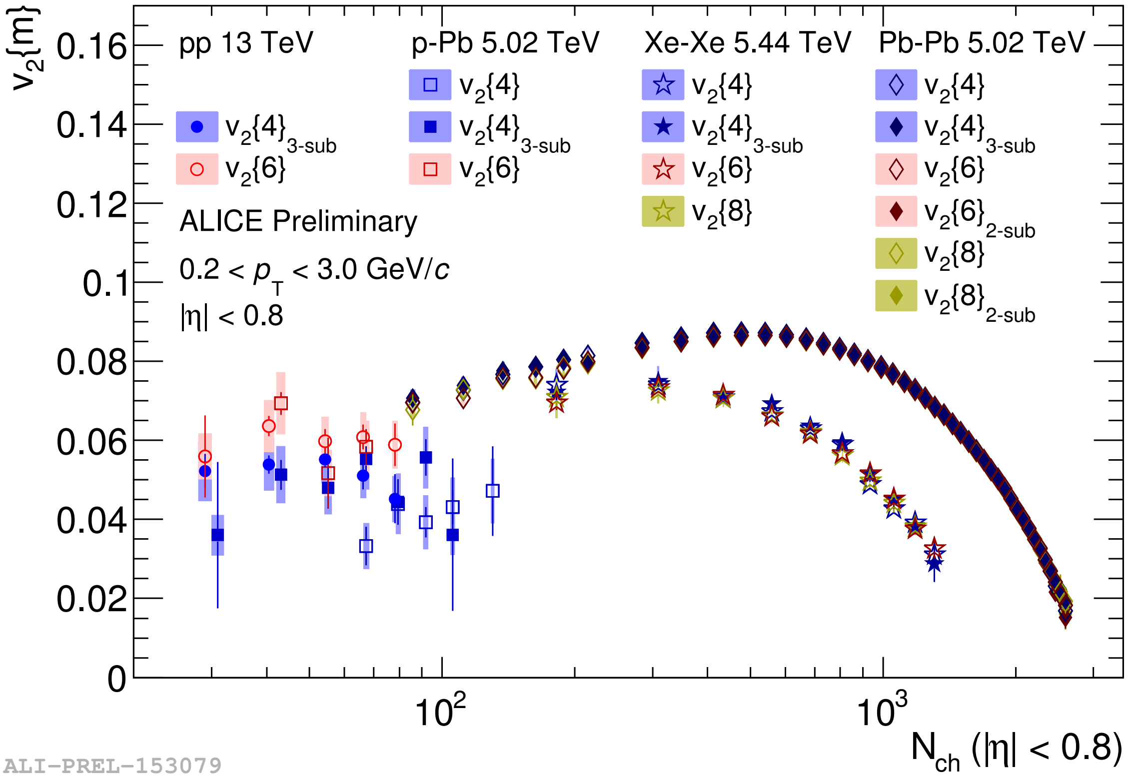

Figure 9.1: Preliminary results for the multiplicity dependence of different flow coefficients $v_n\{m\}$. In some cases an $|\Delta\eta|$ separation is required using sub-events. The results are shown for different collision systems. Figure taken from [145].

due to their early formation time. They experience the whole evolution of the system providing valuable information about the QGP. Heavy quarks are also an important tool in case no QGP is formed. They require different production process with respect to the light quarks, testing the dependence of such effects on the production mechanisms. The result presented in this thesis is one of the first measurements of the v_2 of particles coming from heavy quarks and adds valuable information about the mass dependency of this coefficient. The v_2 is found to be positive with a significance of more than 5σ, providing strong pieces of evidence on the presence of a similar effect in particles from heavy quarks.

Other collaborations have also measured similar features in p–Pb collisions. One of those measurements was performed by the ATLAS Collaboration [146] as shown in Fig. 9.2. The v_2 from electrons (from this thesis) and muons, both coming from heavy-quarks, are compared to the charged-particle v_2. The muon selection in the ATLAS analysis uses a few discriminatory variables to suppress muons from other sources, but no direct subtraction of the background is performed. The required selection is mostly efficient in removing other sources of muons and possible bias due to the non-subtracted background are included on the systematic uncertainties. It is not possible to compare the v_2 for muons and charged particle due to the different momentum re-

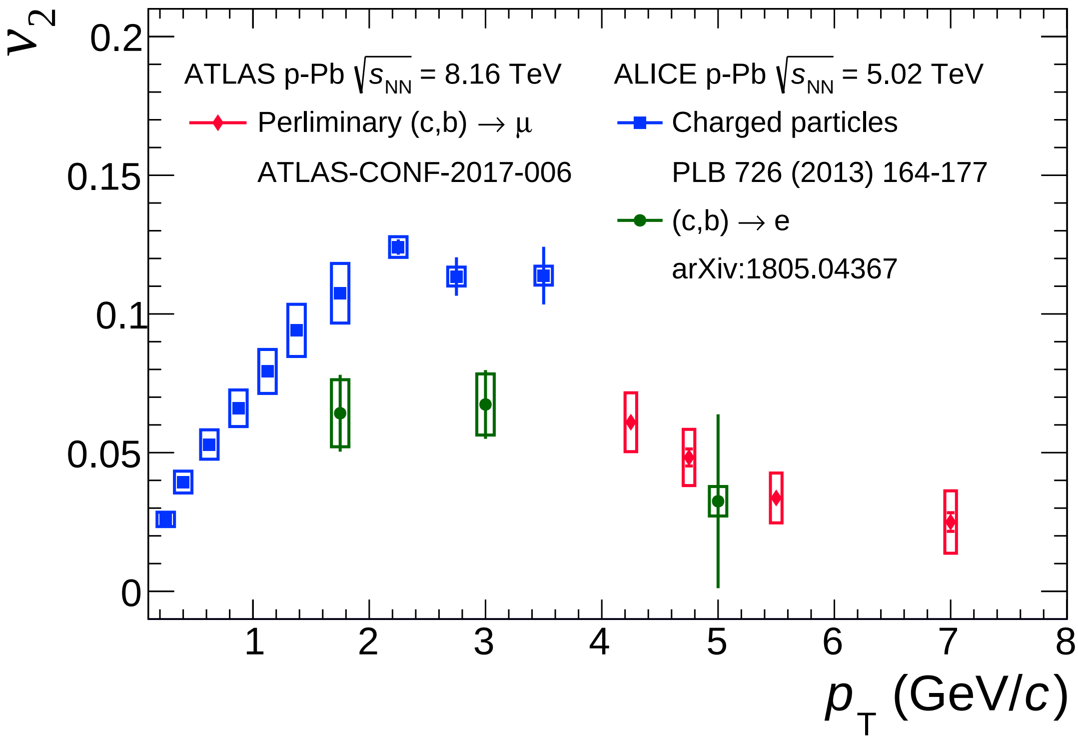

Figure 9.2: Comparison of the v_2 for electrons (from this thesis) and muons [146] from heavy-flavor hadron decays in p–Pb collisions, compared to charged particles.

gion. The charged particles are dominated by light-flavored hadrons, mostly pions, and they have a higher v_2 when compared to the heavy-flavor electron v_2. The measurements of electrons and muons also do not share many points in the same momentum region. The ATLAS measurement is limited to $p_T > 4$ GeV/c due to the trigger configuration and the electron one runs out of events at high momentum since it is taken with a minimum bias trigger. No significant difference is found between the two measurements on the overlapping p_T bin. The different momentum ranges make the measurements complementary. Similar measurements at RHIC also show hints of a non-zero v_2 in small collision systems, as shown in the Quark Matter 2018 [147]. The conclusion is that leptons originating from heavy-quarks have a non-zero v_2 in a broad momentum range.

Similar confirmations of a positive v_2 were also reported for D^0 mesons by the CMS Collaboration [148] and in preliminary results for D^{*+} mesons by the ATLAS collaboration [149]. The ATLAS collaboration measures a positive v_2, but they are unfortunately inconclusive due to the large uncertainties. CMS have employed a dedicated trigger for this measurement and has measured a significant v_2 for D^0 mesons, as shown in the top-left panel of Fig. 9.3. The v_2 is compared to other light-flavor hadrons and the mass hierarchy is similar to the one in Pb–Pb shown in the top right.

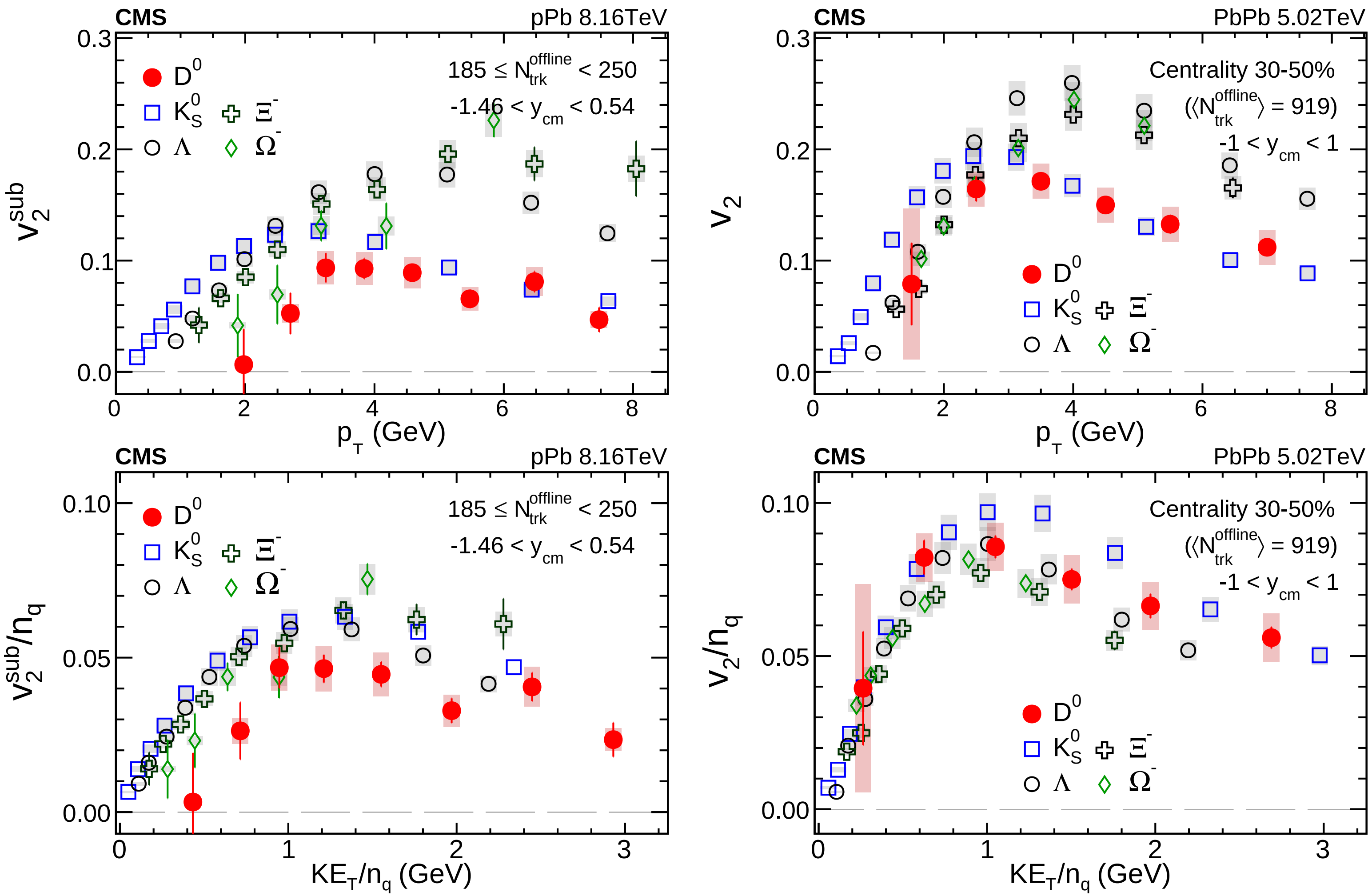

Figure 9.3: Upper: v_2^{sub} results for D^0 mesons, as well as for strange hadrons, as functions of p_{T} in pPb collisions at $\sqrt{s_{\mathrm{NN}}} = 8.16$ TeV (left, [148]) and PbPb collisions at $\sqrt{s_{\mathrm{NN}}} = 5.02$ TeV with centrality between 30 and 50% (right, [72]). Lower: the n_{q}-scaled v_2^{sub} results.

On the bottom of the figure, the v_2 results are scaled by the number of quarks (n_q) in each hadron and the x-axis is transformed into the kinematic energy per constituent quark KE_T/n_q, where $KE_T = \sqrt{m^2 + p_T^2} - m$. This scalling is inspired by the quark-coalescense model [69, 150]. In p–Pb collisions, the light-flavored hadrons converge to a single v_2/n_q value and the D^0 is considerably lower. The same effect is not seen in Pb–Pb collision, where neither the grouping of the lights quarks nor the lower v_2/n_q for D^0 mesons are seen. In any case, this measurement points to a clear positive v_2 for D mesons.

The measurement presented in this thesis, together with measurements from ATLAS and CMS, have pointed to the presence of a non-zero v_2 for particles originating from heavy quarks in p–Pb collisions at LHC energies. All those measurements have been performed recently and they were executed to investigate the origin of the double-ridge structure found in two-particle azimuthal correlations. The origin of this effects is still not clear and those measurements might help to untangle the contributions coming from final-state effects, such as the hydrodynamic evolution of a small QGP medium, or an initial-state effect, linked to the correlations between the colliding particles. The results will shed light on the properties of the QCD and will hopefully help to solve this puzzle. Future measurements in the LHC Run 3 are on the way and they will improve the statistical uncertainties, posing further constraints on models. New observables involving multi-particle correlations with heavy- and light-flavor particles could also bring valuable information. The addition of measurements from particles originating from beauty quarks should be the next step for those analyses.

Bibliography

[1] J. C. Collins and M. J. Perry, "Superdense matter: Neutrons or asymptotically free quarks?," *Phys. Rev. Lett.* **34** (May, 1975) 1353–1356. `https://link.aps.org/doi/10.1103/PhysRevLett.34.1353`.

[2] N. Cabibbo and G. Parisi, "Exponential hadronic spectrum and quark liberation," *Physics Letters B* **59** no. 1, (1975) 67 – 69. `http://www.sciencedirect.com/science/article/pii/0370269375901586`.

[3] J. A. J. Angelo, *Nuclear Technology*. Sourcebooks in Modern Technology. Greenwood (book), 11, 2004.

[4] M. Gell-Mann, "A schematic model of baryons and mesons," *Physics Letters* **8** no. 3, (Feb, 1964) 214–215. `http://linkinghub.elsevier.com/retrieve/pii/S0031916364920013`.

[5] G. Zweig, "An SU_3 model for strong interaction symmetry and its breaking,". `http://cds.cern.ch/record/570209`.

[6] O. W. Greenberg, "Spin and unitary-spin independence in a paraquark model of baryons and mesons," *Phys. Rev. Lett.* **13** (Nov, 1964) 598–602. `https://link.aps.org/doi/10.1103/PhysRevLett.13.598`.

[7] M. Y. Han and Y. Nambu, "Three-Triplet Model with Double SU(3) Symmetry," *Physical Review* **139** no. 4B, (Aug, 1965) B1006–B1010. `http://link.aps.org/doi/10.1103/PhysRev.139.B1006`.

[8] **Particle Data Group** Collaboration, M. Tanabashi *et al.*, "Review of Particle Physics," *Phys. Rev.* **D98** no. 3, (2018) 030001. `https://doi.org/10.1103/PhysRevD.98.030001`.

[9] M. E. Peskin and D. V. Schroeder, *An Introduction to Quantum Field Theory*. Westview Press (book), 1995.

[10] D. J. Gross and F. Wilczek, “Ultraviolet behavior of non-abelian gauge theories,” *Phys. Rev. Lett.* **30** (Jun, 1973) 1343–1346. `https://link.aps.org/doi/10.1103/PhysRevLett.30.1343`.

[11] H. D. Politzer, “Reliable perturbative results for strong interactions?,” *Physical Review Letters* **30** no. 26, (1973) 1346–1349. `https://journals.aps.org/prl/abstract/10.1103/PhysRevLett.30.1346`.

[12] Nobelprize.org, “The Nobel Prize in Physics 2004,” 2014. `http://www.nobelprize.org/nobel_prizes/physics/laureates/2004/`.

[13] K. Olive, “Review of Particle Physics,” *Chinese Physics C* **38** no. 9, (Aug, 2014) 090001. `http://stacks.iop.org/1674-1137/38/i=9/a=090001?key=crossref.47735154e79ac9c858085df9b5a1f93a`.

[14] Clay Mathematics Institute, “Yang–mills and mass gap,” 2018. `http://http://www.claymath.org/millennium-problems/yang%E2%80%93mills-and-mass-gap`.

[15] L. Susskind, “Lattice models of quark confinement at high temperature,” *Phys. Rev. D* **20** (Nov, 1979) 2610–2618. `https://link.aps.org/doi/10.1103/PhysRevD.20.2610`.

[16] P. Petreczky, “Lattice QCD at non-zero temperature,” *J. Phys.* **G39** (2012) 093002, `arXiv:1203.5320 [hep-lat]`.

[17] “The Frontiers of Nuclear Science, A Long Range Plan,” `arXiv:0809.3137 [nucl-ex]`.

[18] **STAR** Collaboration, J. Adams *et al.*, “Experimental and theoretical challenges in the search for the quark gluon plasma: The STAR Collaboration’s critical assessment of the evidence from RHIC collisions,” *Nucl. Phys.* **A757** (2005) 102–183, `arXiv:nucl-ex/0501009 [nucl-ex]`.

[19] G. Martinez, “Advances in Quark Gluon Plasma,” 2013. `arXiv:1304.1452 [nucl-ex]`.

[20] K. Fukushima, “Evolution to the quark–gluon plasma,” *Rept. Prog. Phys.* **80** no. 2, (2017) 022301, `arXiv:1603.02340 [nucl-th]`.

[21] “Evolution of collisions and qgp,” 2018. `https://particlesandfriends.wordpress.com/2016/10/14/evolution-of-collisions-and-qgp/`.

[22] R. J. Glauber and G. Matthiae, “High-energy scattering of protons by nuclei,” *Nucl. Phys.* **B21** (1970) 135–157. `http://doi.org/10.1016/0550-3213(70)90511-0`.

[23] D. d’Enterria, “Jet quenching,” *Landolt-Bornstein* **23** (2010) 471, `arXiv:0902.2011 [nucl-ex]`.

[24] Y. L. Dokshitzer and D. E. Kharzeev, “Heavy quark colorimetry of QCD matter,” *Phys. Lett.* **B519** (2001) 199–206, `arXiv:hep-ph/0106202 [hep-ph]`.

[25] N. Armesto, C. A. Salgado, and U. A. Wiedemann, “Medium induced gluon radiation off massive quarks fills the dead cone,” *Phys. Rev.* **D69** (2004) 114003, `arXiv:hep-ph/0312106 [hep-ph]`.

[26] A. Andronic *et al.*, “Heavy-flavour and quarkonium production in the LHC era: from proton–proton to heavy-ion collisions,” *Eur. Phys. J.* **C76** no. 3, (2016) 107, `arXiv:1506.03981 [nucl-ex]`.

[27] G. Aarts *et al.*, “Heavy-flavor production and medium properties in high-energy nuclear collisions - What next?,” *Eur. Phys. J.* **A53** no. 5, (2017) 93, `arXiv:1612.08032 [nucl-th]`.

[28] **CMS** Collaboration, A. M. Sirunyan *et al.*, “Nuclear modification factor of D^0 mesons in PbPb collisions at $\sqrt{s_{NN}}$ = 5.02 TeV,” `arXiv:1708.04962 [nucl-ex]`.

[29] **CMS** Collaboration, V. Khachatryan *et al.*, “Charged-particle nuclear modification factors in PbPb and pPb collisions at $\sqrt{s_{\mathrm{N\,N}}} = 5.02$ TeV,” *JHEP* **04** (2017) 039, `arXiv:1611.01664 [nucl-ex]`.

[30] **CMS** Collaboration, A. M. Sirunyan *et al.*, “Measurement of the $B^{\pm}$ Meson Nuclear Modification Factor in Pb-Pb Collisions at $\sqrt{s_{NN}} = 5.02$ TeV,” *Phys. Rev. Lett.* **119** no. 15, (2017) 152301, `arXiv:1705.04727 [hep-ex]`.

[31] **CMS** Collaboration, V. Khachatryan *et al.*, “Suppression and azimuthal anisotropy of prompt and nonprompt J/ψ production in PbPb collisions at $\sqrt{s_{\mathrm{NN}}} = 2.76$ TeV,” *Eur. Phys. J.* **C77** no. 4, (2017) 252, `arXiv:1610.00613 [nucl-ex]`.

[32] **CMS** Collaboration, S. Chatrchyan *et al.*, “Study of high-pT charged particle suppression in PbPb compared to pp collisions at $\sqrt{s_{NN}} = 2.76$ TeV,” *Eur. Phys. J.* **C72** (2012) 1945, `arXiv:1202.2554 [nucl-ex]`.

[33] **CMS** Collaboration, S. Chatrchyan *et al.*, “Study of W boson production in PbPb and pp collisions at $\sqrt{s_{NN}} = 2.76$ TeV,” *Phys. Lett.* **B715** (2012) 66–87, `arXiv:1205.6334 [nucl-ex]`.

[34] **ALICE** Collaboration, B. B. Abelev *et al.*, “Suppression of $\Upsilon(1S)$ at forward rapidity in Pb-Pb collisions at $\sqrt{s_{\mathrm{NN}}} = 2.76$ TeV,” *Phys. Lett.* **B738** (2014) 361–372, `arXiv:1405.4493 [nucl-ex]`.

[35] **ALICE** Collaboration, J. Adam *et al.*, “Centrality dependence of the nuclear modification factor of charged pions, kaons, and protons in Pb-Pb collisions at $\sqrt{s_{\mathrm{NN}}} = 2.76$ TeV,” *Phys. Rev.* **C93** no. 3, (2016) 034913, `arXiv:1506.07287 [nucl-ex]`.

[36] **ALICE** Collaboration, J. Adam *et al.*, “Differential studies of inclusive J/ψ and ψ(2S) production at forward rapidity in Pb-Pb collisions at $\sqrt{s_{\mathrm{NN}}} = 2.76$ TeV,” *JHEP* **05** (2016) 179, `arXiv:1506.08804 [nucl-ex]`.

[37] **ALICE** Collaboration, J. Adam *et al.*, “Transverse momentum dependence of D-meson production in Pb-Pb collisions at $\sqrt{s_{\mathrm{NN}}} = 2.76$ TeV,” *JHEP* **03** (2016) 081, `arXiv:1509.06888 [nucl-ex]`.

[38] **ALICE** Collaboration, J. Adam *et al.*, "Measurement of D_s^+ production and nuclear modification factor in Pb-Pb collisions at $\sqrt{s_{NN}} = 2.76$ TeV," *JHEP* **03** (2016) 082, `arXiv:1509.07287 [nucl-ex]`.

[39] **ALICE** Collaboration, S. Acharya *et al.*, "Measurement of Z^0-boson production at large rapidities in Pb-Pb collisions at $\sqrt{s_{NN}} = 5.02$ TeV," *Phys. Lett.* **B780** (2018) 372–383, `arXiv:1711.10753 [nucl-ex]`.

[40] **ALICE** Collaboration, S. Acharya *et al.*, "Transverse momentum spectra and nuclear modification factors of charged particles in pp, p-Pb and Pb-Pb collisions at the LHC," `arXiv:1802.09145 [nucl-ex]`.

[41] **ALICE** Collaboration, J. Adam *et al.*, "$K^*(892)^0$ and $\phi(1020)$ meson production at high transverse momentum in pp and Pb-Pb collisions at $\sqrt{s_{NN}}$ = 2.76 TeV," *Phys. Rev.* **C95** no. 6, (2017) 064606, `arXiv:1702.00555 [nucl-ex]`.

[42] **ATLAS** Collaboration, "Z boson production in Pb+Pb collisions at $\sqrt{s_{NN}}$= 5.02 TeV with the ATLAS detector at the LHC," Tech. Rep. ATLAS-CONF-2017-010, CERN, Geneva, Feb, 2017. `http://cds.cern.ch/record/2244821`.

[43] **CMS** Collaboration, A. M. Sirunyan *et al.*, "Measurement of prompt and nonprompt charmonium suppression in PbPb collisions at 5.02 TeV," *Eur. Phys. J.* **C78** no. 6, (2018) 509, `arXiv:1712.08959 [nucl-ex]`.

[44] **BRAHMS** Collaboration, I. Arsene *et al.*, "Quark gluon plasma and color glass condensate at RHIC? The Perspective from the BRAHMS experiment," *Nucl. Phys.* **A757** (2005) 1–27, `arXiv:nucl-ex/0410020 [nucl-ex]`.

[45] **PHENIX** Collaboration, A. Adare *et al.*, "J/ψ suppression at forward rapidity in Au+Au collisions at $\sqrt{s_{NN}} = 200$ GeV," *Phys. Rev.* **C84** (2011) 054912, `arXiv:1103.6269 [nucl-ex]`.

[46] B. B. Back *et al.*, "The PHOBOS perspective on discoveries at RHIC," *Nucl. Phys.* **A757** (2005) 28–101, `arXiv:nucl-ex/0410022 [nucl-ex]`.

[47] **PHENIX** Collaboration, K. Adcox *et al.*, "Formation of dense partonic matter in relativistic nucleus-nucleus collisions at RHIC: Experimental evaluation by the PHENIX collaboration," *Nucl. Phys.* **A757** (2005) 184–283, `arXiv:nucl-ex/0410003 [nucl-ex]`.

[48] **PHENIX** Collaboration, S. S. Adler *et al.*, "Nuclear modification of electron spectra and implications for heavy quark energy loss in Au+Au collisions at s(NN)**(1/2) - 200-GeV," *Phys. Rev. Lett.* **96** (2006) 032301, `arXiv:nucl-ex/0510047 [nucl-ex]`.

[49] **PHENIX** Collaboration, A. Adare *et al.*, "Heavy Quark Production in $p + p$ and Energy Loss and Flow of Heavy Quarks in Au+Au Collisions at $\sqrt{s_{NN}} = 200$ GeV," *Phys. Rev.* **C84** (2011) 044905, `arXiv:1005.1627 [nucl-ex]`.

[50] **PHENIX** Collaboration, A. Adare *et al.*, "Nuclear-Modification Factor for Open-Heavy-Flavor Production at Forward Rapidity in Cu+Cu Collisions at $\sqrt{s_{NN}} = 200$ GeV," *Phys. Rev.* **C86** (2012) 024909, `arXiv:1204.0754 [nucl-ex]`.

[51] N. Armesto, "Nuclear shadowing," *J. Phys.* **G32** (2006) R367–R394, `arXiv:hep-ph/0604108 [hep-ph]`.

[52] D. Antreasyan, J. W. Cronin, H. J. Frisch, M. J. Shochet, L. Kluberg, P. A. Piroué, and R. L. Sumner, "Production of hadrons at large transverse momentum in 200-, 300-, and 400- GeV $p - p$ and p-nucleus collisions," *Phys. Rev. D* **19** (Feb, 1979) 764–778. `https://link.aps.org/doi/10.1103/PhysRevD.19.764`.

[53] **ALICE** Collaboration, "Preliminary Physics Summary: Measurement of prompt D^0, D^+, D^{*+} and D_s^+ production in p-Pb collisions at $\sqrt{s_{\rm NN}} = 5.02$ TeV,". `http://cds.cern.ch/record/2272160`.

[54] **ALICE** Collaboration, B. Abelev *et al.*, "Transverse momentum distribution and nuclear modification factor of charged particles in p-Pb collisions at $\sqrt{s_{NN}} = 5.02$ TeV," *Phys. Rev. Lett.* **110** no. 8, (2013) 082302, `arXiv:1210.4520 [nucl-ex]`.

[55] **STAR** Collaboration, B. I. Abelev *et al.*, "Long range rapidity correlations and jet production in high energy nuclear collisions," *Phys. Rev.* **C80** (2009) 064912, `arXiv:0909.0191 [nucl-ex]`.

[56] **STAR** Collaboration, J. Adams *et al.*, "Evidence from d + Au measurements for final state suppression of high p(T) hadrons in Au+Au collisions at RHIC," *Phys. Rev. Lett.* **91** (2003) 072304, `arXiv:nucl-ex/0306024 [nucl-ex]`.

[57] **CMS** Collaboration, S. Chatrchyan *et al.*, "Multiplicity and transverse momentum dependence of two- and four-particle correlations in pPb and PbPb collisions," *Phys. Lett.* **B724** (2013) 213–240, `arXiv:1305.0609 [nucl-ex]`.

[58] S. A. Voloshin, A. M. Poskanzer, and R. Snellings, "Collective phenomena in non-central nuclear collisions," *Landolt-Bornstein* **23** (2010) 293–333, `arXiv:0809.2949 [nucl-ex]`.

[59] C. Alves Garcia Prado, *Heavy-flavor nuclear modification factor and event-by-event azimuthal anisotropy correlations in heavy ion collisions*. PhD thesis, Sao Paulo U., 2018. `arXiv:1807.04885 [nucl-th]`.

[60] **CMS** Collaboration, S. Chatrchyan *et al.*, "Studies of azimuthal dihadron correlations in ultra-central PbPb collisions at $\sqrt{s_{NN}} = 2.76$ TeV," *JHEP* **02** (2014) 088, `arXiv:1312.1845 [nucl-ex]`.

[61] M. Luzum and J.-Y. Ollitrault, "Eliminating experimental bias in anisotropic-flow measurements of high-energy nuclear collisions," *Phys. Rev.* **C87** no. 4, (2013) 044907, `arXiv:1209.2323 [nucl-ex]`.

[62] F. G. Gardim, F. Grassi, M. Luzum, and J.-Y. Ollitrault, "Breaking of factorization of two-particle correlations in hydrodynamics," *Phys. Rev. C* **87** (Mar, 2013) 031901. `https://link.aps.org/doi/10.1103/PhysRevC.87.031901`.

[63] **ALICE** Collaboration, K. Aamodt *et al.*, "Harmonic decomposition of two-particle angular correlations in Pb–Pb collisions at $\sqrt{s_{NN}} = 2.76$ TeV," *Phys. Lett.* **B708** (2012) 249–264, `arXiv:1109.2501 [nucl-ex]`.

[64] **STAR** Collaboration, C. Adler *et al.*, "Elliptic flow from two and four particle correlations in Au+Au collisions at s(NN)**(1/2) = 130-GeV," *Phys. Rev.* **C66** (2002) 034904, `arXiv:nucl-ex/0206001 [nucl-ex]`.

[65] **ALICE** Collaboration, B. B. Abelev *et al.*, "Multiparticle azimuthal correlations in p -Pb and Pb-Pb collisions at the CERN Large Hadron Collider," *Phys. Rev.* **C90** no. 5, (2014) 054901, `arXiv:1406.2474 [nucl-ex]`.

[66] P. Huovinen, P. F. Kolb, U. W. Heinz, P. V. Ruuskanen, and S. A. Voloshin, "Radial and elliptic flow at RHIC: Further predictions," *Phys. Lett.* **B503** (2001) 58–64, `arXiv:hep-ph/0101136 [hep-ph]`.

[67] D. Teaney, J. Lauret, and E. V. Shuryak, "Flow at the SPS and RHIC as a quark gluon plasma signature," *Phys. Rev. Lett.* **86** (2001) 4783–4786, `arXiv:nucl-th/0011058 [nucl-th]`.

[68] **ALICE** Collaboration, S. Acharya *et al.*, "Anisotropic flow of identified particles in Pb-Pb collisions at $\sqrt{s_{\mathrm{NN}}} = 5.02$ TeV," *JHEP* **09** (2018) 006, `arXiv:1805.04390 [nucl-ex]`.

[69] D. Molnar and S. A. Voloshin, "Elliptic flow at large transverse momenta from quark coalescence," *Phys. Rev. Lett.* **91** (2003) 092301, `arXiv:nucl-th/0302014 [nucl-th]`.

[70] R. Baier, Y. L. Dokshitzer, S. Peigne, and D. Schiff, "Induced gluon radiation in a QCD medium," *Phys. Lett.* **B345** (1995) 277–286, `arXiv:hep-ph/9411409 [hep-ph]`.

[71] M. Gyulassy and M. Plümer, "Jet quenching in dense matter," *Physics Letters B* **243** no. 4, (1990) 432 – 438. `http://www.sciencedirect.com/science/article/pii/0370269390914095`.

[72] **CMS** Collaboration, A. M. Sirunyan *et al.*, "Measurement of prompt D^0 meson azimuthal anisotropy in Pb-Pb collisions at $\sqrt{s_{NN}}$ = 5.02 TeV," *Phys. Rev. Lett.* **120** no. 20, (2018) 202301, `arXiv:1708.03497 [nucl-ex]`.

[73] **ALICE** Collaboration, J. Adam *et al.*, "Direct photon production in Pb-Pb collisions at $\sqrt{s_{\mathrm{NN}}} = 2.76$ TeV," *Phys. Lett.* **B754** (2016) 235–248, `arXiv:1509.07324 [nucl-ex]`.

[74] **PHENIX** Collaboration, A. Adare *et al.*, "Azimuthally anisotropic emission of low-momentum direct photons in Au+Au collisions at $\sqrt{s_{_{NN}}} = 200$ GeV," *Phys. Rev.* **C94** no. 6, (2016) 064901, `arXiv:1509.07758 [nucl-ex]`.

[75] **PHENIX** Collaboration, A. Adare *et al.*, "Beam-energy and centrality dependence of direct-photon emission from ultra-relativistic heavy-ion collisions," *Submitted to: Phys. Rev. Lett.* (2018) , `arXiv:1805.04084 [hep-ex]`.

[76] F. Karsch, M. T. Mehr, and H. Satz, "Color screening and deconfinement for bound states of heavy quarks," *Zeitschrift für Physik C Particles and Fields* **37** no. 4, (Dec, 1988) 617–622. `https://doi.org/10.1007/BF01549722`.

[77] S. Digal, P. Petreczky, and H. Satz, "Quarkonium feed down and sequential suppression," *Phys. Rev.* **D64** (2001) 094015, `arXiv:hep-ph/0106017 [hep-ph]`.

[78] **CMS** Collaboration, A. M. Sirunyan *et al.*, "Measurement of nuclear modification factors of Υ(1S), Υ(2S), and Υ(3S) mesons in PbPb collisions at $\sqrt{s_{\mathrm{NN}}} = 5.02$ TeV," `arXiv:1805.09215 [hep-ex]`.

[79] **CMS** Collaboration, S. Chatrchyan *et al.*, "Study of Z production in PbPb and pp collisions at $\sqrt{s_{\mathrm{NN}}} = 2.76$ TeV in the dimuon and dielectron decay channels," *JHEP* **03** (2015) 022, `arXiv:1410.4825 [nucl-ex]`.

[80] **ALICE** Collaboration, S. Acharya *et al.*, "Υ suppression at forward rapidity in Pb-Pb collisions at $\sqrt{s_{\mathrm{NN}}}$ = 5.02 TeV," `arXiv:1805.04387 [nucl-ex]`.

[81] J. Rafelski and B. Muller, "Strangeness Production in the Quark - Gluon Plasma," *Phys. Rev. Lett.* **48** (1982) 1066. [Erratum: Phys. Rev. Lett.56,2334(1986)].

[82] **ALICE** Collaboration, J. Adam *et al.*, "Enhanced production of multi-strange hadrons in high-multiplicity proton-proton collisions," *Nature Phys.* **13** (2017) 535–539, `arXiv:1606.07424 [nucl-ex]`.

[83] R. Snellings, "Elliptic Flow: A Brief Review," *New J. Phys.* **13** (2011) 055008, `arXiv:1102.3010 [nucl-ex]`.

[84] **CMS** Collaboration, V. Khachatryan *et al.*, "Observation of Long-Range Near-Side Angular Correlations in Proton-Proton Collisions at the LHC," *JHEP* **09** (2010) 091, `arXiv:1009.4122 [hep-ex]`.

[85] T. Sjostrand, S. Mrenna, and P. Z. Skands, "A Brief Introduction to PYTHIA 8.1," *Comput. Phys. Commun.* **178** (2008) 852–867, `arXiv:0710.3820 [hep-ph]`.

[86] T. Sjostrand, S. Mrenna, and P. Z. Skands, "PYTHIA 6.4 Physics and Manual," *JHEP* **05** (2006) 026, `arXiv:hep-ph/0603175 [hep-ph]`.

[87] M. Bahr *et al.*, "Herwig++ Physics and Manual," *Eur. Phys. J.* **C58** (2008) 639–707, `arXiv:0803.0883 [hep-ph]`.

[88] J. Alwall, R. Frederix, S. Frixione, V. Hirschi, F. Maltoni, O. Mattelaer, H. S. Shao, T. Stelzer, P. Torrielli, and M. Zaro, "The automated computation of tree-level and next-to-leading order differential cross sections, and their matching to parton shower simulations," *JHEP* **07** (2014) 079, `arXiv:1405.0301 [hep-ph]`.

[89] **ATLAS** Collaboration, G. Aad *et al.*, "Observation of Long-Range Elliptic Azimuthal Anisotropies in $\sqrt{s}$ =13 and 2.76 TeV *pp* Collisions with the ATLAS Detector," *Phys. Rev. Lett.* **116** no. 17, (2016) 172301, `arXiv:1509.04776 [hep-ex]`.

[90] **ALICE** Collaboration, B. Abelev *et al.*, "Long-range angular correlations on the near and away side in *p*-Pb collisions at $\sqrt{s_{NN}} = 5.02$ TeV," *Phys. Lett.* **B719** (2013) 29–41, `arXiv:1212.2001 [nucl-ex]`.

[91] **ATLAS** Collaboration, G. Aad *et al.*, "Observation of Associated Near-Side and Away-Side Long-Range Correlations in $\sqrt{s_{NN}}$ = 5.02 TeV Proton-Lead Collisions with the ATLAS Detector," *Phys. Rev. Lett.* **110** no. 18, (2013) 182302, `arXiv:1212.5198 [hep-ex]`.

[92] **CMS** Collaboration, S. Chatrchyan *et al.*, "Observation of long-range near-side angular correlations in proton-lead collisions at the LHC," *Phys. Lett.* **B718** (2013) 795–814, `arXiv:1210.5482 [nucl-ex]`.

[93] **PHENIX** Collaboration, A. Adare *et al.*, "Quadrupole Anisotropy in Dihadron Azimuthal Correlations in Central d+A Collisions at $\sqrt{s_{_{NN}}}$=200 GeV," *Phys. Rev. Lett.* **111** no. 21, (2013) 212301, `arXiv:1303.1794 [nucl-ex]`.

[94] **STAR** Collaboration, L. Yi, "Search for "ridge" in d+Au collisions at RHIC by STAR," *Nucl. Phys.* **A931** (2014) 326–330, `arXiv:1410.1978 [nucl-ex]`.

[95] **ALICE** Collaboration, B. B. Abelev *et al.*, "Long-range angular correlations of ß, K and p in p-Pb collisions at $\sqrt{s_{\rm NN}}$ = 5.02 TeV," *Phys. Lett.* **B726** (2013) 164–177, `arXiv:1307.3237 [nucl-ex]`.

[96] **CMS** Collaboration, V. Khachatryan *et al.*, "Evidence for collectivity in pp collisions at the LHC," *Phys. Lett.* **B765** (2017) 193–220, `arXiv:1606.06198 [nucl-ex]`.

[97] **CMS** Collaboration, V. Khachatryan *et al.*, "Evidence for Collective Multiparticle Correlations in p-Pb Collisions," *Phys. Rev. Lett.* **115** no. 1, (2015) 012301, `arXiv:1502.05382 [nucl-ex]`.

[98] **ATLAS** Collaboration, M. Aaboud *et al.*, "Measurement of long-range multiparticle azimuthal correlations with the subevent cumulant method in pp and $p + Pb$ collisions with the ATLAS detector at the CERN Large Hadron Collider," *Phys. Rev.* **C97** no. 2, (2018) 024904, `arXiv:1708.03559 [hep-ex]`.

[99] **ATLAS** Collaboration, M. Aaboud *et al.*, "Measurement of multi-particle azimuthal correlations in pp, p+Pb and low-multiplicity Pb+Pb collisions with the ATLAS detector," *Eur. Phys. J.* **C77** no. 6, (2017) 428, `arXiv:1705.04176 [hep-ex]`.

[100] **PHENIX** Collaboration, C. Aidala *et al.*, "Measurements of Multiparticle Correlations in d + Au Collisions at 200, 62.4, 39, and 19.6 GeV and p + Au Collisions at 200 GeV and Implications for Collective Behavior," *Phys. Rev. Lett.* **120** no. 6, (2018) 062302, `arXiv:1707.06108 [nucl-ex]`.

[101] **ATLAS** Collaboration, G. Aad *et al.*, "Measurement with the ATLAS detector of multi-particle azimuthal correlations in p+Pb collisions at $\sqrt{s_{NN}}$ =5.02 TeV," *Phys. Lett.* **B725** (2013) 60–78, `arXiv:1303.2084 [hep-ex]`.

[102] B. Schenke, S. Jeon, and C. Gale, "(3+1)D hydrodynamic simulation of relativistic heavy-ion collisions," *Phys. Rev.* **C82** (2010) 014903, `arXiv:1004.1408 [hep-ph]`.

[103] H. Mäntysaari, B. Schenke, C. Shen, and P. Tribedy, "Imprints of fluctuating proton shapes on flow in proton-lead collisions at the LHC," *Phys. Lett.* **B772** (2017) 681–686, `arXiv:1705.03177 [nucl-th]`.

[104] P. Bozek, "Collective flow in p-Pb and d-Pb collisions at TeV energies," *Phys. Rev.* **C85** (2012) 014911, `arXiv:1112.0915 [hep-ph]`.

[105] P. Bozek and W. Broniowski, "Collective dynamics in high-energy proton-nucleus collisions," *Phys. Rev.* **C88** no. 1, (2013) 014903, `arXiv:1304.3044 [nucl-th]`.

[106] C. Shen, J.-F. Paquet, G. S. Denicol, S. Jeon, and C. Gale, "Collectivity and electromagnetic radiation in small systems," *Phys. Rev.* **C95** no. 1, (2017) 014906, `arXiv:1609.02590 [nucl-th]`.

[107] M. Strickland, "Small system studies: A theory overview," in *27th International Conference on Ultrarelativistic Nucleus-Nucleus Collisions (Quark Matter 2018) Venice, Italy, May 14-19*. 2018. `arXiv:1807.07191 [nucl-th]`.

[108] J. L. Nagle and W. A. Zajc, "Small System Collectivity in Relativistic Hadron and Nuclear Collisions," `arXiv:1801.03477 [nucl-ex]`.

[109] Z. Xu and C. Greiner, "Thermalization of gluons in ultrarelativistic heavy ion collisions by including three-body interactions in a parton cascade," *Phys. Rev.* **C71** (2005) 064901, `arXiv:hep-ph/0406278 [hep-ph]`.

[110] Z.-W. Lin, C. M. Ko, B.-A. Li, B. Zhang, and S. Pal, "A Multi-phase transport model for relativistic heavy ion collisions," *Phys. Rev.* **C72** (2005) 064901, `arXiv:nucl-th/0411110 [nucl-th]`.

[111] K. Gallmeister, H. Niemi, C. Greiner, and D. H. Rischke, "Exploring the applicability of dissipative fluid dynamics to small systems by comparison to the Boltzmann equation," *Phys. Rev.* **C98** no. 2, (2018) 024912, `arXiv:1804.09512 [nucl-th]`.

[112] A. Bzdak and G.-L. Ma, "Elliptic and triangular flow in p+Pb and peripheral Pb+Pb collisions from parton scatterings," *Phys. Rev. Lett.* **113** no. 25, (2014) 252301, `arXiv:1406.2804 [hep-ph]`.

[113] K. Dusling, M. Mace, and R. Venugopalan, "Multiparticle collectivity from initial state correlations in high energy proton-nucleus collisions," *Phys. Rev. Lett.* **120** no. 4, (2018) 042002, `arXiv:1705.00745 [hep-ph]`.

[114] M. Mace, V. V. Skokov, P. Tribedy, and R. Venugopalan, "Systematics of azimuthal anisotropy harmonics in proton-nucleus collisions at the LHC from the Color Glass Condensate," `arXiv:1807.00825 [hep-ph]`.

[115] A. Andronic, P. Braun-Munzinger, and J. Stachel, "Thermal hadron production in relativistic nuclear collisions: The Hadron mass spectrum, the horn, and the QCD phase transition," *Phys. Lett.* **B673** (2009) 142–145, `arXiv:0812.1186 [nucl-th]`. [Erratum: Phys. Lett. B678, 516 (2009)].

[116] J. Cleymans, I. Kraus, H. Oeschler, K. Redlich, and S. Wheaton, "Statistical model predictions for particle ratios at $\sqrt{s_{NN}} = 5.5$ TeV," *Phys. Rev.* **C74** (2006) 034903, `arXiv:hep-ph/0604237 [hep-ph]`.

[117] C. Bierlich and J. R. Christiansen, "Effects of color reconnection on hadron flavor observables," *Phys. Rev. D* **92** (Nov, 2015) 094010. `https://link.aps.org/doi/10.1103/PhysRevD.92.094010`.

[118] C. De Melis, "The CERN accelerator complex. Complexe des accélérateurs du CERN,". `https://cds.cern.ch/record/2119882`. General Photo.

[119] **ALICE** Collaboration, K. Aamodt *et al.*, "The ALICE experiment at the CERN LHC," *JINST* **3** (2008) S08002.

[120] **ALICE** Collaboration, K. Aamodt *et al.*, "Alignment of the ALICE Inner Tracking System with cosmic-ray tracks," *JINST* **5** (2010) P03003, `arXiv:1001.0502 [physics.ins-det]`.

[121] **ALICE** Collaboration, G. Dellacasa *et al.*, *ALICE time projection chamber: Technical Design Report*. Technical Design Report ALICE. CERN, Geneva, 2000. `https://cds.cern.ch/record/451098`.

[122] ALICE Collaboration, F. Carminati, P. Foka, P. Giubellino, A. Morsch, G. Paic, J.-P. Revol, K. Safarík, Y. Schutz, and U. A. W. (editors), "ALICE: Physics Performance Report, Volume I," *Journal of Physics G: Nuclear and Particle Physics* **30** no. 11, (Nov, 2004) 1517–1763. `http://stacks.iop.org/0954-3899/30/i=11/a=001?key=crossref.549e5139025a3f3c3793968198808795`.

[123] **ALICE** Collaboration, "The alice time of flight detector," 2018. `http://aliceinfo.cern.ch/Public/en/Chapter2/Chap2_TOF.html`.

[124] **ALICE** Collaboration, C. W. Fabjan, L. Jirdén, V. Lindestruth, L. Riccati, D. Rorich, P. Van de Vyvre, O. Villalobos Baillie, and H. de Groot, *ALICE trigger data-acquisition high-level trigger and control system: Technical Design Report*. Technical Design Report ALICE. CERN, Geneva, 2004. `https://cds.cern.ch/record/684651`.

[125] **ALICE** Collaboration, B. B. Abelev *et al.*, "Performance of the ALICE Experiment at the CERN LHC," *Int. J. Mod. Phys.* **A29** (2014) 1430044, `arXiv:1402.4476 [nucl-ex]`.

[126] R. Brun and F. Rademakers, "ROOT: An object oriented data analysis framework," *Nucl. Instrum. Meth.* **A389** (1997) 81–86.

[127] **ALICE** Collaboration, "Aliroot documentation," 2018. `http://alice-offline.web.cern.ch/AliRoot/Manual.html`.

[128] **ALICE** Collaboration, "Software repository of the alice collaboration on github," 2018. `https://github.com/alisw`.

[129] R. Frühwirth, "Application of Kalman filtering to track and vertex fitting," *Nucl. Instrum. Meth.* **A262** (1987) 444–450.

[130] J. Wagner, *Electrons from decays of open charm and beauty hadrons in p-Pb collisions at $\sqrt{s_{NN}} = 5.02$ TeV*. PhD thesis, Technische Universität Darmstadt, Darmstadt, July, 2016. `http://tuprints.ulb.tu-darmstadt.de/5710/`.

[131] X.-N. Wang and M. Gyulassy, "HIJING: A Monte Carlo model for multiple jet production in pp, pA and AA collisions," *Phys. Rev.* **D44** (1991) 3501–3516.

[132] Brun, Rene and others, "GEANT Detector Description and Simulation Tool." CERN Program Library Long Write-up, W5013, 1994.

[133] **ALICE** Collaboration, J. Adam *et al.*, "Centrality dependence of particle production in p-Pb collisions at $\sqrt{s_{\mathrm{NN}}} = 5.02$ TeV," *Phys. Rev.* **C91** no. 6, (2015) 064905, `arXiv:1412.6828 [nucl-ex]`.

[134] **ALICE** Collaboration, S. Acharya *et al.*, "Azimuthal anisotropy of heavy-flavour decay electrons in p-Pb collisions at $\sqrt{s_{\mathrm{NN}}} = 5.02$ TeV," `arXiv:1805.04367 [nucl-ex]`.

[135] **ATLAS** Collaboration, M. Aaboud *et al.*, "Measurements of long-range azimuthal anisotropies and associated Fourier coefficients for pp collisions at $\sqrt{s} = 5.02$ and 13 TeV and p+Pb collisions at $\sqrt{s_{\mathrm{NN}}} = 5.02$ TeV with the ATLAS detector," *Phys. Rev.* **C96** no. 2, (2017) 024908, `arXiv:1609.06213 [nucl-ex]`.

[136] **ALICE** Collaboration, S. Acharya *et al.*, "Production of muons from heavy-flavour hadron decays in p-Pb collisions at $\sqrt{\mathbf{s_{NN}}} = \mathbf{5.02}$ TeV," *Phys. Lett.* **B770** (2017) 459–472, `arXiv:1702.01479 [nucl-ex]`.

[137] **ALICE** Collaboration, S. Acharya *et al.*, "Search for collectivity with azimuthal J/ψ-hadron correlations in high multiplicity p-Pb collisions at $\sqrt{s_{\mathrm{NN}}} = 5.02$ and 8.16 TeV," *Phys. Lett.* **B780** (2018) 7–20, `arXiv:1709.06807 [nucl-ex]`.

[138] **ALICE** Collaboration, J. Adam *et al.*, "Elliptic flow of electrons from heavy-flavour hadron decays at mid-rapidity in Pb-Pb collisions at $\sqrt{s_{\mathrm{NN}}} = 2.76$ TeV," *JHEP* **09** (2016) 028, `arXiv:1606.00321 [nucl-ex]`.

[139] **ALICE** Collaboration, J. Adam *et al.*, "Forward-central two-particle correlations in p-Pb collisions at $\sqrt{s_{\mathrm{NN}}} = 5.02$ TeV," *Phys. Lett.* **B753** (2016) 126–139, `arXiv:1506.08032 [nucl-ex]`.

[140] **ALICE** Collaboration, B. Abelev *et al.*, "Upgrade of the ALICE Experiment: Letter Of Intent," *J. Phys.* **G41** (2014) 087001.

[141] P. Buncic, M. Krzewicki, and P. Vande Vyvre, "Technical Design Report for the Upgrade of the Online-Offline Computing System," Tech. Rep. CERN-LHCC-2015-006. ALICE-TDR-019, Apr, 2015. `https://cds.cern.ch/record/2011297`.

[142] S. H. I. Barboza *et al.*, "SAMPA chip: a new ASIC for the ALICE TPC and MCH upgrades," *JINST* **11** no. 02, (2016) C02088.

[143] **ALICE** Collaboration, "Upgrade of the ALICE Time Projection Chamber,". `https://cds.cern.ch/record/1622286`.

[144] **ALICE** Collaboration, B. Abelev *et al.*, "Technical Design Report for the Upgrade of the ALICE Inner Tracking System," *J. Phys.* **G41** (2014) 087002.

[145] **ALICE** Collaboration, K. Gajdošová, "ALICE measurements of flow coefficients and their correlations in small (pp and p-Pb) and large (Xe-Xe and Pb-Pb) collision systems," *Submitted to: Nucl. Phys.* (2018) , `arXiv:1807.02998 [nucl-ex]`.

[146] **ATLAS** Collaboration, "Measurement of the long–range pseudorapidity correlations between muons and charged-particles in $\sqrt{s_{\mathrm{NN}}}$=8.16 TeV proton-lead collisions with the ATLAS detector,". `https://cds.cern.ch/record/2244808`.

[147] T. Hachiya, "Azimuthal anisotropy of $b \to e$ and $c \to e$ in 200 gev au+au collisions at rhic-phenix," in *XXVIIth International Conference on Ultra-relativistic Nucleus-Nucleus Collisions*. 2018. `https://indico.cern.ch/event/656452/contributions/2859695/`.

[148] **CMS** Collaboration, A. M. Sirunyan *et al.*, "Elliptic flow of charm and strange hadrons in high-multiplicity pPb collisions at $\sqrt{s_{\mathrm{NN}}} = 8.16$ TeV," *Phys. Rev. Lett.* **121** no. 8, (2018) 082301, `arXiv:1804.09767 [hep-ex]`.

[149] **ATLAS** Collaboration, "*D* meson production and long-range azimuthal correlation in 8.16 TeV p+Pb collisions with ATLAS," Sep, 2017. `https://cds.cern.ch/record/2285811`.

[150] R. J. Fries, B. Muller, C. Nonaka, and S. A. Bass, "Hadronization in heavy ion collisions: Recombination and fragmentation of partons," *Phys. Rev. Lett.* **90** (2003) 202303, `arXiv:nucl-th/0301087 [nucl-th]`.